Measuring Fission Chain Dynamics Through Inter-event Timing of Correlated Particles

by

Mateusz Monterial

A dissertation submitted in partial fulfillment
of the requirements for the degree of
Doctor of Philosophy
(Nuclear Science)
in the University of Michigan
2017

Doctoral Committee:

Professor Sara A. Pozzi, Chair
Professor Christine A. Aidala
Dr. Shaun Clarke
Dr. Peter Marleau, Sandia National Laboratories
Professor David K. Wehe

Mateusz Monterial
mateuszm@umich.edu
ORCID iD: 0000-0002-0739-305X

Ku pamięci mojej zmarłej babci, która zawsze wiedziała, że będę miał tytuł doktora.

ACKNOWLEDGMENTS

First and foremost, I am thankful to my adviser Professor Sara Pozzi for giving me a chance to attend the fine nuclear program at the University of Michigan, and subsequently providing me with the running room to explore my research interests. My Sandia mentor Peter Marleau has been indispensable for the work presented in this thesis, and I thank him for putting up with me over all these years. The discussions I had with my colleagues at Sandia and the University of Michigan have made me a better researcher and contributed to this work in innumerable ways. Special mention goes out to Marc Paff and Tony Shin, who had to review this thesis on short notice because of my procrastination. My mother always believed that I could do this, and she started me on this path long ago. Lastly, my lovely wife Alisha has been a constant pillar of support throughout all my schooling, and I am forever grateful for her patience and generosity.

Below is the mandatory shout-out to the taxpayers.

This material is based upon work supported by the U.S. Department of Homeland Security under Grant Award Number, 2012-DN-130-NF0001. The views and conclusions contained in this document are those of the authors and should not be interpreted as representing the official policies, either expressed or implied, of the U.S. Department of Homeland Security.

Sandia National Laboratories is a multimission laboratory managed and operated by National Technology and Engineering Solutions of Sandia, LLC., a wholly owned subsidiary of Honeywell International, Inc., for the U.S. Department of Energy's National Nuclear Security Administration under contract DE-NA-0003525. SAND Number: SAND2017-10258 T.

This work was funded in-part by the Consortium for Verification Technology under Department of Energy National Nuclear Security Administration award number DE-NA0002534.

TABLE OF CONTENTS

LIST OF FIGURES

LIST OF TABLES

LIST OF APPENDICES

LIST OF ABBREVIATIONS

AR Augmented Reality

BeRP Beryllium Reflected Plutonium

CFD Constant Fraction Discrimination

DAF Device Assembly Facility

DU Depleted Uranium

DZC Derivative Zero Crossing

CIF Cumulative Integral Fraction

FWHM Full Width Half Maximum

FP False Positive

HEU Highly Enriched Uranium

IAEA International Atomic Energy Agency

MCMC Markov chain Monte Carlo

MeVee MeV electron equivalent

MINER Mobile Imager of Neutrons for Emergency Response

MLEM Maximum Log-likelihood Expectation Maximization

NDA Non-Destructive Assay

NPT Non-Proliferation Treaty

NNSS Nevada National Security Site

KDE Kernel Density Estimator

PET Positron Emission Tomography

PGF Probability Generating Function

PMT Photomultiplier Tube

PSD Pulse Shape Discrimination

ROC Receiver Operator Characteristic

TACS Training Assembly for Criticality Safety

TP True Positive

TCPH Time Correlated Pulse Height

TOF Time of Flight

TOFFEE Time of Flight Fixed By Energy Estimation

SOE Stochastic Origin Ensemble

SPECT Single Photon Emission Computed Tomography

SQ Significant Quantities

SNM Special Nuclear Material

WGPu Weapons-Grade Plutonium

ABSTRACT

Neutrons born from fission may go on to induce subsequent fissions in self-propagating series of reactions resulting in a fission chain. Fissile materials comprise all isotopes capable of sustaining nuclear fission chain reactions, and are therefore a necessary prerequisite for the construction of a nuclear weapon. As a result the accountancy and characterization of fissile material is of great importance for national security and the international community. The rate at which neutrons "multiply" in a fissile material is a function of the composition, total mass, density, and shape of the object. These are key characteristics sought out in areas of nuclear non-proliferation, safeguards, treaty verification and emergency response. This thesis demonstrates a novel technique of measuring the underlying fission chain dynamics in fissile material through temporal correlation of neutrons and gamma rays emitted from fission.

Fissile material exhibits key detectable signatures through the emission of correlated neutrons and gamma rays from fission. The Non-Destructive Assay (NDA) community has developed mature techniques of assaying fissile material that detect these signatures, such as neutron counting by thermal capture based detectors, and gamma-ray spectroscopy. An alternative use of fast organic scintillators provides three additional capabilities: (1) discrimination between neutrons and gamma-ray pulses (2) sub-nanosecond scale timing between correlated events (3) measurement of deposited neutron energy in the detector. This thesis leverages these capabilities into to measure a new signature, which is demonstrated to be sensitive to both fissile neutron multiplication and presence of neutronically coupled reflectors. In addition, a new 3D imaging method of sources of correlated gamma rays and neutrons is presented, which can improve estimation of total source volume and localization.

CHAPTER 1

Introduction

1.1 Brief History of the Fission Chain

The 20^{th} century began with a rudimentary understanding of the atom, which was suitable for chemistry and molecular studies. The only known subatomic particle was the electron. From the start of the century, each breakthrough discovery of the subatomic structure of the atom came about every decade. In 1911 Ernest Rutherford discovered the nucleus, and at the end of that decade, in 1919, the proton. In the 1920s Neils Bohr, Erwin Schrödinger, and Werner Heisenberg, among other theorists, developed quantum mechanics, which contradicted the theory of nuclear electrons that would keep protons from being repelled apart. This theoretical work greatly bolstered the case for the existence of a neutron, which was eventually discovered in 1932 by James Chadwick at the Cavendish laboratory headed by Rutherford himself.

The discovery of the neutron proved pivotal in the history of the fission chain, from that point on the world was just thirteen years away from its first nuclear weapons test. Only a year out from the necessary discovery of the neutron, Leo Szilard would conceive of the concept of self-sustaining neutron-induced chain reactions. Even more impressive was his immediate grasp of the explosive implications of such theory, which would profoundly change the world [1]. In that same year, Szilard and Enrico Fermi would patent the idea of a nuclear reactor. Nuclear fission was discovered in 1938 by Otto Hahn, and explained theoretically a year later by Lise Meitner and Otto Frisch through the use of Bohr's liquid drop-model. That same year, Nazi Germany and

Soviet Union would join forces and invade Poland, officially starting World War II in the European theater.

Szilard's dream of a sustained fission chain was realized in 1942 when the Chicago Pile-1 reactor achieved criticality. The work of Szilard and his fellow European refugees under the Manhattan project would eventually give birth to an atomic weapon which was first tested under the code name "Trinity" in a New Mexico desert on July 16^{th} 1945. The scientific lead of weapon design, J. Robert Oppenheimer, described the moment that the bomb went off in an interview for a 1965 television program *The Decision to Drop The Bomb*:

> "We knew the world would not be the same. A few people laughed, a few people cried. Most people were silent. I remembered the line from the Hindu scripture, the Bhagavad Gita. Vishnu is trying to persuade the Prince that he should do his duty, and, to impress him, takes on his multi-armed form and says, 'Now I am become Death, the destroyer of worlds.' I suppose we all thought that, one way or another."

The quote out of the Hindu scripture has now ubiquitous association with that fateful day. One wonders if Oppenheimer thought of it before a fellow physicist Kenneth Bainbridge turned to him immediately after the test and proclaimed:

> "Now we are all sons of bitches."

The end of the war simultaneously begun the next chapter in geopolitical world order. The proverbial Genie was out of the bottle and around the world atomic weaponry would be acquired, by hook or by crook, by an exponentially weaker and poorer list of state actors stretching from Joseph Stalin to Kim Jong-il. In the early 1950s United States and the Soviet Union developed hydrogen bombs, while at same time Eisenhower launched an effort to demilitarize nuclear technology beginning with the "Atoms for Peace" speech at the UN General Assembly. As of today there are eight declared nuclear armed states and 31 countries with operational nuclear reactors.

1.2 Motivation

The global spread in nuclear technology, coupled with a rapid buildup of nuclear weapon stockpile during the Cold War, has left a legacy of abundant global supply of fissile material necessary for making an atomic bomb. Anticipating this problem, the international community has put together a regime of safeguards and non-proliferation, administered through the International Atomic Energy Agency (IAEA), with the specific goal of accounting for and preventing the illicit spread of fissile material and nuclear weapon technology. The centerpiece of global nuclear cooperation is the Non-Proliferation Treaty (NPT), which stipulates a basic bargain: all countries may engage in peaceful use of nuclear technology provided that it's not used for nuclear weapons, and countries with nuclear weapons will work toward complete disarmament. These frameworks function as a deterrent for states that may seek nuclear weaponry, by providing an international inspection regime of nuclear facilities inside member states.

Upholding the disarmament pillar of the NPT bargain has been largely carried out through bilateral treaties between the United States and Russia, which account for over 90% of total nuclear warhead stockpile. These bilateral agreements started in the Cold War with the Strategic Arms Limitation Talks (SALT), which lead to the Strategic Arms Reduction Treaties (START); the latest generation of which is the New START ratified in 2011. These treaties are verified by each others' inspection teams that are invited to visit host nuclear facility of the other country and certify compliance.

The other threat of loose fissile material concerns the use of weapons of mass destruction by non-state actors. Nuclear terrorism includes a range of potential attacks from deploying a dirty bomb to poisoning the water supply, but by far the most consequential is acquisition of a nuclear weapon [2]. Although the probability of terrorist acquiring and detonating a nuclear weapon is low, the threat is quite real. In his 2009 speech in Prague on nuclear weapons, President Obama singled out nuclear terrorism as primary concern:

> "So, finally, we must ensure that terrorists never acquire a nuclear weapon. This is the

> most immediate and extreme threat to global security. One terrorist with one nuclear weapon could unleash massive destruction. Al Qaeda has said it seeks a bomb and that it would have no problem with using it. And we know that there is unsecured nuclear material across the globe."

Preventing fissile material from falling into the wrong hands involves monitoring of illicit trafficking at border crossings and through other ports of entry. The most important task is detection, but once an item of concern is seized, its immediate characterization is a critical task for the emergency response teams. At a later time the item may be sent to a laboratory in order to determine the place of origin through nuclear forensic methods.

The protocols concerning the nuclear threats outlined above fall into four general categories, which have some overlaps:

1. Non-proliferation: preventing the spread of nuclear weapons.
2. Safeguards: securing and account of fissile material.
3. Treaty Verification: confirmation of disarmament.
4. Emergency Response: on-site characterization of seized material.
5. Nuclear forensics: laboratory investigation material age, source origin etc.

All of these require the measurement and characterization of fissile material, which by definition produces nuclear chain reactions. As I will demonstrate, the measurement of fission chain dynamics is relevant because it provides information about the fissile material itself: mass, geometrical configuration, and presence of any neutronically coupled materials, such as high explosives.

1.3 Thesis Contribution and Overview

Fissions produce two primary detectable signatures: gamma rays and neutrons. The prevalence of thermal capture neutron detectors, such as He-3 proportional counters, have limited the develop-

ment of neutron counting based Non-Destructive Assay (NDA). An alternative use of Pulse Shape Discrimination (PSD) capable fast organic scintillators provides three additional key capabilities:

1. Distinguishing between gamma ray and neutron pulses, and incorporating both into the analysis.

2. Sub-nanosecond scale timing between correlated detected events.

3. Measurement of deposited neutron energy through scintillation due to proton recoil.

In addition, the use of fast electronics provides a way to store individual detected pulses and apply advanced digital processing techniques in post-measurement analysis. This thesis leverages these capabilities and provides an alternative technique for characterizing fissile material through fast gamma-neutron correlations. The sensitivity of this new signature to fissile material neutron multiplication and presence of neutron reflectors is explored. Furthermore, a correlated gamma ray coupled with traditional double neutron scatter imaging is shown to produce a new 3D imaging technique, which can further improve estimation of total source volume and localization.

The following is a brief summary of each chapter:

Chapter 2: The definitions of fissile material properties and other neutrons sources are laid out. The basics of the three major NDA techniques, Rossi-alpha, Feynman-Y and Multiplicity Counting, are presented in chronological order, along with the history of the development of each method. Finally, the rationale and advantages of using the new gamma-neutron correlated signature concludes the chapter.

Chapter 3: The best practices and pitfalls of digital processing of organic scintillator pulses from timing to pulse shape discrimination. The details of common processing tasks (e.g. energy calibration) that are applied to data throughout this thesis are collected here for succinctness. A Bayesian approach for classifying the pulses and estimating the gamma-ray or neutron probability is put forward as the PSD method of choice for this work.

Chapter 4: An overview of the prior work with Time Correlated Pulse Height (TCPH) distribution is given, along with a new method of analyzing the distribution and fitting empirical

parameters. Results from fits to measured and simulated TCPH distributions of the BeRP ball with polyethylene and tungsten reflectors are shown.

Chapter 5: A reformulation of TCPH signature into a one-dimensional Time of Flight Fixed By Energy Estimation (TOFFEE) distribution is presented. A template matching approach is used in the context of treaty verification for dismantlement and item confirmation of both plutonium and uranium objects.

Chapter 6: A physical interpretation of the time-dependent neutron population in fissile material surrounded by a reflector is derived from two-region point kinetics. The model is then used to fit physical parameters to bare and reflected configurations of the BeRP ball.

Chapter 7: A new 3D imaging method of sources of coincident gamma rays and neutrons is presented. Preliminary measurements and simulations are shown as a proof-of-concept of the imaging technique.

CHAPTER 2

Fissile Material Properties and Detection Techniques

2.1 Definitions

2.1.1 Source of Neutrons

A broad overview and details about neutron sources and expected yields of most common sources are given in [3]. The focus of the following overview is the correlated emission of neutrons and gamma rays from those sources. The source of fission neutrons comes in two categories: spontaneous and induced. Spontaneous fission is the result of heavy actinides spontaneously decaying into two or more lighter isotopes. In this respect it's simply another mode of decay of an isotope. By contrast, induced fission necessitates neutron absorption by a fissionable isotope from outside the nucleus. The emitted products are neutrons and gamma rays, with slight variations in the energy and number (or multiplicity) of neutrons and gamma rays produced. In addition, there is incident neutron energy dependence on the number and energy of the emitted neutrons. The fission process typically results in the near simultaneous emission of 0 to 6 neutrons and 0 to 20 gamma rays. The distribution of the number of emitted particles is called the "multiplicity" distribution, and examples are shown in Figure 2.1 and 2.2.

The mean neutron multiplicity, $\bar{\nu}$, depends on the isotope, and varies from as little as 2.16 for Pu-240 to as much as 3.757 for Cf-252. Establishing the value of $\bar{\nu}$ has been of utmost importance because of its role in determining the length of a fission chain, and thus when an assembly becomes critical. In a critical assembly the rate of neutron production, which depends among other factors

on $\bar{\nu}$, is equal to the rate of neutron loss. As a result, neutron multiplicity and $\bar{\nu}$ have been studied with numerous experiments to a greater precision than gamma-ray multiplicity [4].

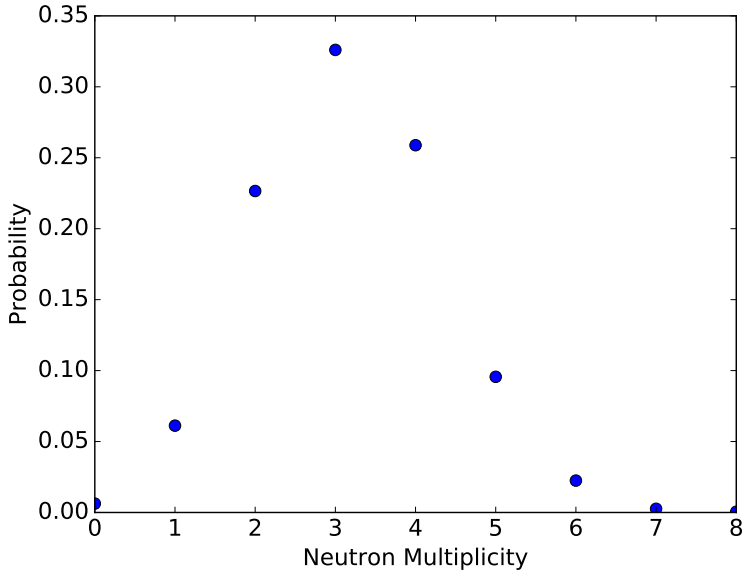

Figure 2.1: Neutron probability distribution for induced fission of Pu-239, with 2 MeV neutron incident neutron energy [4].

The energy of the resulting gamma rays and neutrons also varies between fission events. The mean energy of the fission neutrons is around 2 MeV, and distribution of the neutron energies can be approximated by a Watt spectrum defines as

$$f(E) = C \exp(-E/a) \sinh(\sqrt{bE}) \tag{2.1}$$

where C is a normalization factor and a and b are constants that vary between fissioning isotopes [7].

For isotopes with large cross-sections for fission over the Watt spectrum, the neutrons produced from fission can subsequently induce other fissions, and thus causing a fission chain. Neutrons and gamma rays from the same fission chain are also correlated, though some of them are not born simultaneously. Because these correlated gamma rays and neutrons come from different fissions, there will exist a characteristic time between their emission that set them apart from other sources

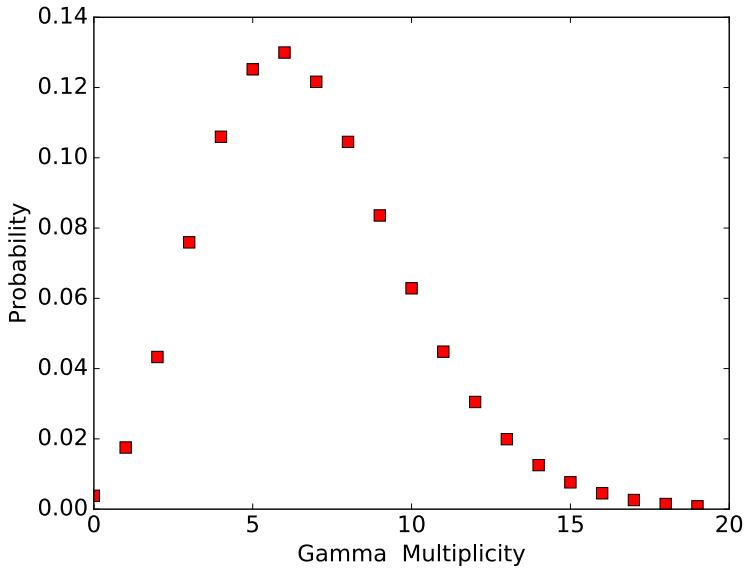

Figure 2.2: Gamma probability distribution for induced fission of Pu-239 [5, 6].

of correlated neutrons and gamma rays. It is this difference that is exploited and explored in this dissertation.

The last category of ubiquitous sources of correlated gamma rays and neutrons are the so-called alpha-neutron, or alpha-n, sources. Their name derives from the (α, n) reactions that occur when a heavy alpha emitter (e.g. Pu-238, Am-241) is brought together with suitable light target isotope (e.g. Be-9, F-19, Li-7, O-17). After capturing the alpha particle and emitting a neutron, the product isotope is left in an excited state which leads to emission of correlated gamma rays. Unlike fission gamma rays, these have specific characteristic energies caused by discrete energy level differences among the excited states and the ground state. The energy spectra of emitted neutrons are also quite different from their fission counterparts, and vary widely between different of alpha-n sources. For example, the mean neutron energy of an AmBe source is 4.5 MeV, but only 300 keV for an AmLi source. This range of energies makes alpha-n sources versatile laboratory tools, but (α, n) reactions also provide a source of neutrons in reactor fuel and stored fissile material.

Uranium and plutonium oxides are the most common form of nuclear fuel used in commercial power plants, and uranium hexafluoride (UF_6) is used for enrichment and storage. Oxygen and fluorine have a relatively large (α, n) cross-sections, therefore these mixtures emit correlated

gamma rays and neutrons of both types: fission and (α, n). The result is a mixed source of neutrons, which have to be accounted for in the coincidence counting techniques described in Section 2.2. The neutrons born out of (α, n) reaction have a multiplicity of one, and by themselves only contribute to the uncorrelated background. However, just like spontaneous fission neutrons, (α, n) neutrons may induce fissions and start fission chains, which contribute to the coincidence response. The relative strength of (α, n) neutrons depends in large part to the source strength of alpha emitters and the amount of low-Z isotopes mixed in the material, and not directly on the amount of spontaneously fissioning isotopes [8]. Since fissile material assay is determined from measuring the amount these spontaneously fissioning isotopes, any unaccounted contributions from (α, n) neutrons may adversely affect the final mass estimations.

2.1.2 Special Nuclear Material

Special Nuclear Material (SNM) is actually defined by law under Title I, Chapter 2, Section 11 of the Atomic Energy Act of 1954 as “plutonium, uranium enriched in isotope 233 or in the isotope 235 [9]." The definition is quite unsatisfactory and leaves open the question of what is so “special" about Special Nuclear Material (SNM). The answer comes later at the end of Section 53 “special nuclear material shall be distributed only on terms... that no user will be permitted to construct an atomic weapon." It’s clear, therefore, that SNM is important because it is the prerequisite for making atomic weapons. For this reason SNM is often used interchangeably with the term “fissile" material, however, the latter has a more precise technical definition.

Fissile material is capable of undergoing induced fission by the neutrons that they emit, and therefore can sustain nuclear chain reactions. The binding energy supplied from capturing a neutron is greater than the critical energy necessary to split the atom. Therefore, no additional energy is required from the neutron to induce a fission which gives birth to subsequent neutrons. In general, heavy actinides with odd number of neutrons meet the physical requirements to be considered fissile. However, the most important fissile isotopes are U-235 and Pu-239, because both can be readily weaponized for a fission-bomb [10]. The other fissile isotopes suffer from either high

spontaneous fission rate or high α-emission rate, which can cause pre-detonation by supplying initiating neutrons. The exception is U-233, which is theoretically weaponizable, but inevitably contaminated by short lived U-232 which makes it practically prohibitive as a nuclear weapon material [10].

Fissile material is a subset of a larger group of fissionable material. As the name suggests, fissionable material is capable of undergoing induced fission by a neutron above a threshold energy. For example, U-235 is both fissionable and fissile. However, other fissionable but not fissile isotopes require extra energy from the neutron to overcome the critical energy necessary to undergo a fission. The distinction stems from the difference in the stability of heavy actinides with odd number of neutrons and/or protons compared with those with an even number of both. The even numbered isotopes are more stable, therefore an odd numbered isotope has greater binding energy after it captures a neutron. Notable examples of fissionable isotopes are Th-232 and U-238, which can be used in nuclear reactor fuel.

The IAEA has determined Significant Quantities (SQ) of different fissile isotopes that are "the approximate amount of nuclear material for which the possibility of manufacturing a nuclear explosive device can not be excluded... and should not be confused with critical masses. [11]" In practice SQs are a useful standard in the safeguards community for discussing the smallest quantity of fissile material worth accounting for, and are summarized in Table 2.1. Purity is also important, uranium enriched in excess of 20% of U-235 is deemed Highly Enriched Uranium (HEU) and plutonium with 93% or more Pu-239 is called Weapons-Grade Plutonium (WGPu).

Table 2.1: Significant Quantities of SNM [11].

Material	SQ
Pu[a]	8 kg Pu
U-233	8 kg U-233
HEU (U-235 $\geq$ 20%)	25 kg U-235

[a] For Pu containing less than 80% Pu-238.

2.1.3 Multiplication Factor

Fissile material is defined by its ability to “multiply" neutrons by generating fission chains. The multiplication factor k is the ratio of the number of neutrons born in one generation to those in the previous generation:

$$k = \frac{\text{number of neutrons in one generation}}{\text{number of neutrons in a previous generation}}. \tag{2.2}$$

This term provides a useful shorthand for the state of neutrons in a multiplying system, such as a reactor. If $k = 1$ then the neutron population is stable and the system is referred to as being “critical". If $k > 1$ then the neutron population will, on average, increase at a geometric rate and the system is said to be “supercritical." Finally, if $k < 1$ then neutron population will, on average, decrease exponentially in subsequent generations and the system is said to be “subcritical."

In reactor theory, four and six-factor formulas are used to relate the factor k to physical properties of a system. The exact definitions of these formulas are not particularly relevant for this thesis work, but the difference between them is useful in highlighting the meaning of k-effective or k_{eff}, which often appears in literature without context. The four factor formula assumes an infinite medium, but the six factor assumes a finite medium by including the probabilities of neutron non-leakage which results in k_{eff} [12]. Neutron leakage is a term that describes the escape of neutrons from the system.

The factor k also makes an appearance as an eigenvalue for so-called criticality “search" problems, where the goal is to determine the size and composition of a reactor which achieves criticality. An example of its use can be seen in the operator notation of one-speed (energy) group neutron diffusion model

$$\mathbf{M}\phi = \frac{1}{k}\mathbf{F}\phi \tag{2.3}$$

where $\mathbf{M}$ is the destruction operator (leakage and absorption), $\mathbf{F}$ the production operator (fission),

and ϕ the neutron flux [13]. In this form the factor k plays a role of a modifier of the production term, $\mathbf{F}\phi$, in order to make it equal to leakage and absorption of neutrons $\mathbf{M}\phi$. The procedure is to pick a reactor size and composition (which modifies $\mathbf{M}$ and $\mathbf{F}$), and solve for the factor k. If $k \neq 1$ then new reactor parameters are chosen and the calculation is repeated. However, if $k = 1$ then the critical reactor configuration was found and the search is over.

Point reactor kinetics, which start from diffusion theory and omit spacial dependence, offer a time based representation of k. The spacial simplification allows for analytical solutions to time-dependent problems in nuclear reactor dynamics. This definition of k takes the form of a quotient of two terms:

$$k = \frac{l}{\Lambda} \tag{2.4}$$

where l is the neutron lifetime which is the mean time for one neutron to be removed by either absorption or leakage, and neutron reproduction or generation time, Λ, is the mean time for one neutron to be replaced by another via fission [14]. The implication here is that a reactor or assembly is critical when $l = \Lambda$.

Neutron generation time is a common term used in reactor point kinetics, but in the nondestructive assay formulations, the mean fission time, l_f, is far more prevalent. The two factors are related by $\bar{\nu}$:

$$\Lambda = \frac{1}{\bar{\nu}\Sigma_f v} \tag{2.5}$$

$$l_f = \frac{1}{\Sigma_f v} \tag{2.6}$$

where Σ_f is the macroscopic fission cross-section and v is neutron velocity, the product of which ($v\Sigma_f$) is the production rate of neutrons. Swapping out Λ with l_f in Eq. 2.4 leads to another

interpretation of the multiplication factor:

$$k = \frac{l\bar{\nu}}{l_f} = p_f\bar{\nu} \tag{2.7}$$

where the ratio of mean neutron lifetime and mean time to fission is shown to be p_f, the probability that a neutron undergoes fission.

2.1.4 Subcritical Neutron Multiplication

The focus of this work is on subcritical systems, and specifically new techniques in measuring their state and configuration. An important parameter derived from the multiplication constant k is the subcritical neutron multiplication. If starting with a single source neutron, plugging in 1 to the denominator of Eq. 2.2, the factor k becomes the average number of neutrons born in the first generation. These first generation neutrons will go on to produce k^2 neutrons in the second generation and so on until the total number of neutrons produced from a single starting neutron is

$$1 + k + k^2 + k^3 + k^4... \tag{2.8}$$

For subcritical systems ($k < 1$) this geometric series converges and the total neutron multiplication is

$$M_T = \frac{1}{1-k} \tag{2.9}$$

Eq. 2.9 is sometimes referred to as the prompt neutron multiplication, because the contribution of delayed neutrons is ignored in this formulation. Prompt neutrons appear almost instantaneously (femtoseconds) with the fission events. Delayed neutrons are the result of the decay of fission products and contribute only a small fraction to the total neutrons resulting from fission. The delay in the time that these neutrons are born is quite significant, as much as several seconds after the

initial fission event. The contribution of delayed neutrons are crucial for reactor dynamics and they make reactor criticality control feasible [15]. However, for the purposes of this dissertation the contribution of delayed neutrons can be ignored because the time-scales that govern their birth (tens μs to tens of seconds) are outside of the coincident time windows that are used in the analysis throughout this work (hundreds of ns).

A more important distinction in the definition of neutron multiplication is between total and leakage multiplication. Leakage multiplication, sometimes referred to as "net" multiplication, describes the number of neutrons that escape from the subcritical assembly [16]. This is an important distinction because the neutrons that escape are the only ones that are available for measurement. If the probability of leakage is p_l then leakage multiplication is just

$$M_L = p_l M_T = \frac{p_l}{1-k}. \tag{2.10}$$

An illustration of the difference between total and leakage multiplication is shown in Figure 2.3. Note that an individual fission chain is used as an example of subcritical multiplication, but in actuality this concepts describes the average behavior of fission chains in a subcritical assembly.

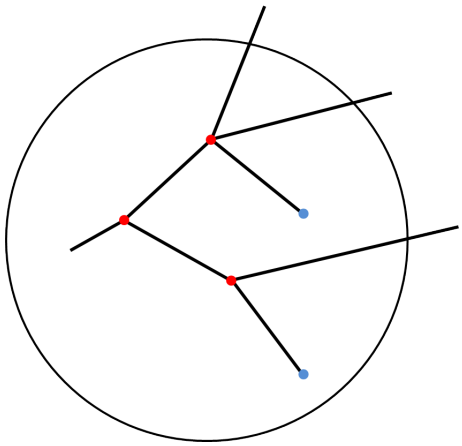

Figure 2.3: Diagram of a fission chain evolution inside hypothetical sphere of special nuclear material. Each of the black lines represent neutrons, the red nodes represent a fission events and the blue termination points represent neutron absorption. The total multiplication is equivalent to the total number of of neutrons or the number of black lines ($M_T = 8$). However, the leakage multiplication is only three ($M_L = 3$), equivalent to the number of neutrons that escaped the sphere.

2.2 Fissile Material Analysis Techniques

The established techniques discussed below — Rossi-alpha, Feynman-Y and Multiplicity Counting — all fall under the theoretical purview of neutron noise analysis [17]. The first two techniques trace their origins to the Manhattan project, and the works of Feynman, de Hoffmann and Serber among many others [18]. Measurement of fundamental system parameters, for example the prompt neutron period, and physical quantities, like $\bar{\nu}$, was of great interest to the brilliant scientists working out these problems atop a New Mexican mesa. Their test subjects were either near-critical or briefly supercritical fast assemblies, or purpose built reactors. A few decades later the NDA community that inherited these techniques had to adapt to the new challenge of fissile material accountancy. The challenge for these applications was to accurately measure the mass of fissile material, and in particular plutonium, in test samples of unknown heterogeneous composition.

The application of the theory has been molded by technology available for neutron coincidence counting at the time, namely thermal capture neutron detectors (He-3) and analog circuitry [8]. More recent work has focused on updating some techniques, such as multiplicity counting, by adopting the analysis to include new factors that come with the use of fast organic scintillators [19]. Some traditional techniques, like Feynman-Y, have been updated to include the contribution for gamma rays measured by PSD capable organic scintillators [20]. This thesis work aims to move beyond traditional analysis and make use of additional signatures available to fast organic scintillators, which will be explored later in this chapter.

2.2.1 Rossi-alpha

Rossi-alpha is one of the most well known and earliest neutron noise analysis methods. The method's namesake, Bruno Rossi, observed larger-than-expected fluctuations in neutron count rates of a boiling water reactor at Los Alamos and reckoned that they were caused by correlated neutrons from fission chains [21]. His key insight was that a single neutron could kick off a long fission chain which would evolve on a characteristically shorter time scale than the random birth of

other source neutrons. The pioneers of neutron noise experiments were interested in measuring the prompt neutron period, α, which is inversely related to the efficiency of explosive reactions [21]. The prompt neutron period can be measured directly by introducing and then removing a strong neutron source (source jerk), or briefly forming a supercritical configuration [22]. Rossi's experiment was an alternative approach to determine α that relied on measuring the fluctuations from many individual fission chains in a near critical assembly which is self-modulated (i.e. the mean time between emission of source neutrons is of the order of or longer than prompt neutron period) [23].

The Rossi-alpha experiment itself is technically simple. First, an initial neutron detection opens up a predetermined time window, or gate, and the times to all subsequent events in that window are binned. The window then shifts to the second event and the binning process proceeds as before. This process is shown in Figure 2.4, and in essence depicts the operations of a shift register. In the days of analog circuitry these time windows would have to be fixed [8], but modern list-mode data acquisitions allows for any time window to be applied in post-measurement analysis [24].

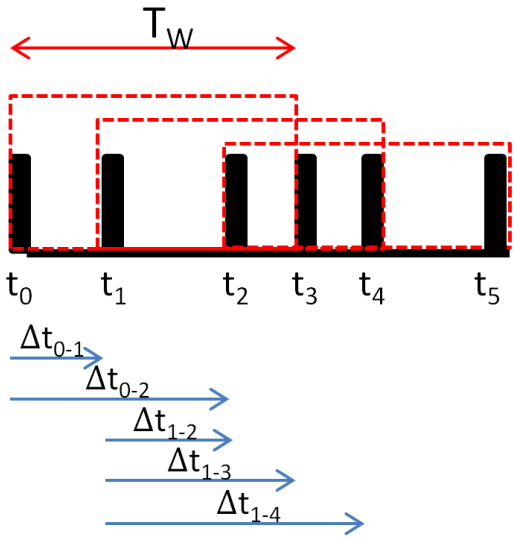

Figure 2.4: Example of time binning in a Rossi-alpha experiment of a neutron event train depicted by black bars. The blue arrows show binned times within each of the fixed time windows of length T_W.

Feynman is credited for developing the theory for interpreting the Rossi experiments [25]. His

formulations had no spacial dimension (single region), and one-speed neutrons (single group), which are prerequisites for modern point reactor kinetics. One-speed assumption meant a single neutron energy, and thus a single average probability for induced fission. Under those assumptions the rate of change of the number neutrons in a multiplying system is the difference between production through fission and loss by absorption or leakage:

$$\frac{dN}{dt} = \frac{\bar{\nu}N}{l_f} - \frac{N}{l} \tag{2.11}$$

The terms in Eq. 2.11 have been previously defined in Section 2.1.3. Given the definition of multiplication constant in Eq. 2.7, the balance Eq. 2.11 can be re-written as

$$\frac{dN}{dt} = \frac{k-1}{l}N. \tag{2.12}$$

Taking $N(0) = N_0$ as the initial condition, the solution to this first order linear differential equation is

$$N(t) = N_0 e^{\frac{k-1}{l}t} = N_0 e^{\alpha t} \tag{2.13}$$

where α is the prompt neutron period and is negative for subcritical assemblies [26]. The constant α is also referred to as the neutron rate of decay when the term in the exponent is negative [18]. It is assumed that delayed neutrons are born on much longer time scales and therefore do not affect the measurement of α.

It follows that if the neutron population decays exponentially then the probability of detecting a correlated neutron is governed by exponential decay. This probability of counting a correlated neutron at time t in interval dt after an initial neutron at $t = 0$ is

$$p(t)dt = F\epsilon\ dt + \epsilon\frac{D_v k^2}{2(1-k)l}e^{\alpha t}dt \tag{2.14}$$

where F is the average fission rate and ϵ is the detection efficiency per fission [24]. Diven's parameter, D_v, is a measure of the relative width of the neutron multiplicity distribution

$$D_v = \frac{\overline{\nu(\nu-1)}}{\bar{\nu}^2}. \tag{2.15}$$

In practice the expression of the shape of the Rossi-alpha distribution is simplified to

$$s(t) = A + Re^{\alpha t} \tag{2.16}$$

where A is the accidental rate of detecting uncorrelated neutrons in the time window and R is the correlated (or "real") coincidence rate [8]. With analog shift registers it is possible to measure both R and A by opening two gates: a coincidence gate following the source trigger, and an accidental gate after a some delay. List-mode digital acquisition allows for construction of Ross-alpha histograms made up of the time differences between detected neutrons. These measured Rossi-alpha distributions are then fit to Eq. 2.16 in order to determine the prompt neutron decay constant α.

2.2.2 Feynman-Y

The Feynman-Y, or the variance-over-mean technique, was developed by Richard Feynman alongside his theoretical work on the Rossi-alpha experiments [18] [27]. The fluctuations in counts per unit time, c, from a purely random source should, by definition, follow a Poisson distribution. However, the presence of correlated counts from fission chains add an excess variance beyond that predicted from Poisson statistics. Feynman quantified this phenomena by taking the ratio of count variance and mean:

$$\frac{\overline{c^2} - (\bar{c})^2}{\bar{c}} = 1 + Y \tag{2.17}$$

where $\bar{c}$ is the average counts per unit time, $\overline{c^2}$ is the average of the square of the counts per unit time, and Y accounts for a deviation from Poisson statistics. For a gate width t, the parameter Y can be approximated by

$$Y = \frac{\epsilon(\overline{\nu^2} - \bar{\nu})}{(-\alpha l_f)^2}\left[1 + \frac{1 - e^{\alpha t}}{\alpha t}\right] \tag{2.18}$$

where l_f is the mean time between fissions, defined previously in Eq. 2.6. Note that this is following Orndoff's [26] rather than Feynman's [18] notation for α in order to stay consistent with the presentation in Section 2.2.1.

The expression in Eq. 2.18 can be further simplified to just the first term if the gate width is long enough to capture the prompt period but small compared to the delay period and the delayed neutrons do not significantly contribute to the overall neutron multiplication [28]. It is possible to determine if the gate width is long enough by taking multiple measurements with increasing gate widths. The Feynman-Y test statistic will asymptotically approach a maximum value, and the minimum required gate width can be determined by plotting the two values against each other. Feynman also made approximations and variations on Y to make it useful for interpreting experimental data. In particular, Feynman used the technique for measuring and validating the second moment of the neutron multiplicity distribution [28].

Operationally the measurement of Feynman-Y differs in two important ways from the Rossi-alpha. First, the number of counts is recorded, as opposed to the time between counts in a gate. Second, the gate is opened through a series of clock triggers, not by events registered in the detector. Feynman-Y histograms, or distributions, can be constructed from the number of counts in each gate, and provide a visual representation of the deviation from an expected Poisson distribution.

The first and second moments of the Feynman-Y distributions were used by Dowdy et al. to develop a formalism that includes the contributions of spontaneous fission, neutron multiplication and (α,n) contaminants [29]. A variation on the Feynman-Y was used by Dowdy et al. to relate

measured fluctuations with these physical parameters:

$$Q_m = \overline{c(c-1)}\bar{c}^2 \tag{2.19}$$

where c is still counts per unit time. However, it was only possible to solve for two of the three parameters under two special cases: negligible (α,n) contribution or a non-multiplying sample ($M = 1$). Using a more advanced technique, Multiplicity Counting, it is possible to solve for all three unknowns. This technique is the subject of the following section.

2.2.3 Multiplicity Counting

Multiplicity counting arose out of the need for accountability of fissile material in the nuclear fuel cycle. The problem is that the fissile material recovered from spent fuel has a complex source term driven by

1. F_s : spontaneous fission rate
2. S_α : (α, n) neutron emission rate
3. M_L : neutron leakage multiplication

The goal is to ultimately measure F_s, which in passive counting can be related back to plutonium effective mass through empirically determined factors [8]. This still requires the knowledge of plutonium isotopics, which can be measured with gamma ray spectroscopy. HEU mass can be measured through active multiplicity counting, with a variation of the equations discussed in this section [30]. S_α and M_L are complicating parameters whose contribution depends on isotopic composition and total fissile mass and geometry.

Before multiplicity counting theory was developed in the early 1980s, it was possible to measure F_s through neutron coincidence counting by assuming that either S_α or M_L was negligible [31] [32]. Multiplicity counting theory set out to relate the probability distribution, $r_m(\tau)$, of counting m number of neutron multiplets in time window τ with the three source properties

enumerated above. The following four general assumptions underline the multiplicity counting theory [33, 34]:

1. The test sample is taken to have no spacial extent (point geometry), and therefore parameters such as the detector efficiency and the probability of fission are assumed to be spatially uniform.

2. Neutron detection efficiency, probability of fission, and neutron multiplicity are assumed to be energy independent. All physically associated quantities are in effect collapsed into a single energy group. The neutron energy spectrum from (α, n) reactions and spontaneous fission are assumed to be the same.

3. The time response of the detector, or the neutron die-away time in the detector moderator, follows a single exponential function with a characteristic decay constant λ.

4. All induced fission neutrons are emitted simultaneously with the initiating (α, n) or spontaneous fission neutrons. This is often referred to as the "superfission" concept, and is valid if the time response of the detector is much slower compared to the lifetime of a fission chain.

5. Neutron capture without fission is negligible, which means the probability of leakage is just the complement of the fission probability ($p_L = 1 - p_f$).

Early efforts led to rather complex expressions for the source parameters and required extensive numerical efforts. In particular, the probability distribution $P_\nu(p_f)$ of emitting ν neutrons from a fission cascade was computed using Monte Carlo [35]. This distribution depends on the multiplicity distribution of neutrons P_ν and the probability of a neutron inducing fission p_f, and is the consequence of the superfission assumption and the need to account for neutron multiplication. By taking the moments of $r_m(\tau)$ it is possible to use analytical approximations for the moments of $P_\nu(p_f)$ which are accurate for a limited number of fissions in a cascade [36]. The approximation is the result of summing the products of probabilities of neutron emission across multiple generations until any additional contributions to $P_\nu(p_f)$ become negligible.

The real breakthrough came by using the mathematical tool of the Probability Generating Function (PGF) and forming the *factorial* moments of $r_m(\tau)$ into which the $P_\nu(p_f)$ distribution also enters in the form of its factorial moments [37, 38]. Factorial moments of $r_m(\tau)$ are far less complicated and require less numerical effort to solve for requisite source term properties compared to the moment formulations [39]. The μ^{th} factorial moment of the $P_\nu(p_f)$ distribution is

$$\overline{\nu_{(\mu)}(p_f)} = \sum_{\nu=\mu}^{\infty} \binom{\nu}{\mu} P_\nu(p_f) \tag{2.20}$$

which can be expressed analytically as a function of the factorial moments of the neutron multiplicity distribution for either induced, $\bar{\nu}_{I(\mu)}$, or spontaneous ,$\bar{\nu}_{s(\mu)}$, fissions [34]. These are defined as

$$\bar{\nu}_{j(\mu)} = \sum_{\mu=\nu} \binom{\nu}{\mu} P_{j\nu} \tag{2.21}$$

where $j = s$ or $j = I$ for either spontaneous or induced fissions. Note that the first moment and factorial moment of neutron multiplicity are equivalent ($\bar{\nu} = \bar{\nu}_{j(1)}$).

The single, R_1, double, R_2, and triple R_3 count rates can be expressed in terms of the aforementioned factorial moments, detector efficiency (ϵ) and desired sample source terms:

$$R_1 = \epsilon M_L (F_s \bar{\nu}_{s(1)} + S_\alpha) \tag{2.22}$$

$$R_2 = \epsilon^2 F_s M_L^2 \bar{\nu}_{s(2)} \left[1 + (M_L - 1) \left(1 + \frac{S_\alpha}{\bar{\nu}_{s(1)} F_s} \right) \frac{\bar{\nu}_{s(1)} \bar{\nu}_{I(2)}}{\bar{\nu}_{s(2)} (\bar{\nu}_{I(1)} - 1)} \right] \tag{2.23}$$

$$\begin{aligned} R_3 = \epsilon^3 F_s M^3 \bar{\nu}_{s(3)} \Bigg\{ & 1 + 2(M_L - 1) \frac{\bar{\nu}_{s(2)} \bar{\nu}_{I(2)}}{\bar{\nu}_{s(3)} (\bar{\nu}_{I(1)} - 1)} \\ & + (M_L - 1) \left(1 + \frac{S_\alpha}{\bar{\nu}_{s(1)} F_s} \right) \left[\frac{\bar{\nu}_{s(1)} \bar{\nu}_{I(2)}}{\bar{\nu}_{s(3)} (\bar{\nu}_{I(1)} - 1)} \left(1 + 2(M_L - 1) \frac{\bar{\nu}_{I(2)}^2}{\bar{\nu}_{I(3)} (\bar{\nu}_{I(1)} - 1)} \right) \right] \Bigg\} \end{aligned} \tag{2.24}$$

These are idealized rates because they do not account for detector response time and method of triggering, either on signal or randomly on gate of length τ. The number of counts in those gates are used to build signal $n_m(\tau)$ and random or background $b_m(\tau)$ distributions whose factorial moments

($m_{n(\mu)}$ and $m_{b(\mu)}$) are then related back to the rates of correlated signal multiplets, R_μ, defined in Eqs. 2.22, 2.23, and 2.24. It's possible to formulate R_μ only in term of $m_{b(\mu)}$, which under certain conditions are equivalent to the factorial moments of the Feynman-Y distribution [40].

Cifarelli and Hage gave a comprehensive overview of possible solutions of source and detector parameters in [34]. For the purposes of this background, it will suffice to give the case for the absolute determination of F_s, S_α and M_L. First, M_L is obtained from the smallest possible solution ($M_L > 1$) of the following third order polynomial:

$$a + bM_L + cM_L^2 + dM_L^3 = 0 \tag{2.25}$$

where

$$a = \frac{R_3}{\epsilon^3} \tag{2.26}$$

$$b = \frac{R_2}{\epsilon^2}\left(\frac{\bar{\nu}_{s(3)}}{\bar{\nu}_{s(2)}} - 2\frac{\bar{\nu}_{I(2)}}{\bar{\nu}_{I(1)} - 1}\right) \tag{2.27}$$

$$c = \frac{R_1}{\epsilon(\bar{\nu}_{I(1)} - 1)}\left(\frac{\bar{\nu}_{I(2)}\bar{\nu}_{s(3)}}{\bar{\nu}_{s(2)}} - \bar{\nu}_{I(3)}\right) + \frac{2R_2\bar{\nu}_{I(2)}}{\epsilon^2(\bar{\nu}_{I(1)} - 1)} \tag{2.28}$$

$$d = \frac{2R_2\bar{\nu}_{I(2)}}{\epsilon^2(\bar{\nu}_{I(1)} - 1)} - c \tag{2.29}$$

The spontaneous fission rate and (α, n) neutron rate can then be solved in terms of M_L:

$$F_s = \frac{R_2}{\epsilon^2 M_L^2 \bar{\nu}_{s(2)}} - \frac{R_1\bar{\nu}_{I(2)}(M_L - 1)}{\epsilon M_L \bar{\nu}_{s(2)}(\bar{\nu}_{I(1)} - 1)} \tag{2.30}$$

$$S_\alpha = \frac{R_1}{\epsilon M_L}\left(1 + \frac{\bar{\nu}_{s(1)}\bar{\nu}_{I(2)}(M_L - 1)}{\bar{\nu}_{s(2)}(\bar{\nu}_{I(1)} - 1)}\right) - \frac{R_2\bar{\nu}_{s(1)}}{\epsilon^2 M_L^2 \bar{\nu}_{s(2)}} \tag{2.31}$$

Multiplicity counting is a mature and robust technique that is useful for assaying a wide array of test samples with unknown contribution of (α, n) neutrons. The typical assay bias is minimal if the test sample is well represented by a point model [33]. However, the biggest drawback is the need for both accurate knowledge of and large absolute detector efficiency. The former is needed to keep uncertainties to a minimum and the latter is required for reasonable measurement times.

Both are a consequence of the ϵ^3 term that is manifest in Eq. 2.24, which can become quite small. As a consequence, multiplicity counters are typically large and are designed to surround the entire test sample. If the value S_α is known or negligible then other correlation counting methods can yield more accurate results in a shorter measurement time [8, 33].

2.2.4 Correlating Particles with Fast Organic Scintillators.

A single fission event releases multiple correlated neutrons and gamma rays, both of which can both be measured with PSD capable organic scintillators. Unlike capture based systems, which require fast neutrons to be slowed or "moderated" to lower energies where capture cross-sections are high, organic scintillators can detect fast neutrons and gamma rays on a sub-nanosecond time scale. This timing allows for resolution of the generation time between fissions in a chain. The PSD capability enables the measurement of cross-correlation distributions of neutron-neutron, gamma-neutron, neutron-gamma, or gamma-gamma pairs from fission events in the same fission chain. In addition, the mode of detection of fast neutrons in organics scintillators makes it possible to preserve some information about the incident neutron energy. This additional information allows for an extension of gamma-neutron and neutron-gamma correlations into TCPH distributions which are useful for characterizing fissile material [41–43]. The TCPH distribution is a bivariate histogram of an estimated incident neutron energy and the time to a correlated gamma ray. TCPH analysis is introduced in Section 2.2.5, but before proceeding it is important to explain the choice of mixed particle correlation and the issues with neutron-neutron and gamma-gamma pairs.

Gamma-gamma and neutron-neutron pairs suffer from significantly more detector cross-talk: when the same particle scatters between separate detector cells. These cross-talk events are characteristic of the detector system geometry, not the measured source itself. Additionally, in different but correlated neutron-neutron pairs, both particles have a time-of-flight that depends on their respective energies, and thus the time between two correlated neutrons is spread, even for pairs originating from the same fission.

By contrast, correlated gamma rays from the same fission should arrive at the detector simul-

taneously. Therefore, any time spread between two detected gamma rays above that of timing resolution can be attributed to fission chain smearing. However, correlated gamma-gamma pairs have many terrestrial (e.g. K-40, Tl-208, Ra-226, Ac-228) and cosmic sources of uncorrelated background that degrade the signal-to-noise of this signature. In addition to correlated fission gamma rays, fissile material typically produces many more uncorrelated decay gamma rays from fission products. Depending on the amount of material present, these uncorrelated gamma rays can create an overwhelming rate of accidental coincidences.

Gamma rays are also highly attenuated by the emitting fissile material itself, because of the high density and mass number. As a result of this self-shielding, detectors will be primarily sensitive to gamma rays emitted from the outer layer of an assembly. It is therefore desirable to include at least one neutron in the correlated pair to gain sensitivity to a larger fraction of the total volume of material.

It can be reasonably concluded that correlated gamma-neutron and neutron-gamma pairs offer the good sensitivity and signal-to-noise ratio. The gamma ray provides a clean indication of the time of a fission, while the neutron is both more penetrating and a clear indication of fission. Cross talk is also reduced by correlating particles of different type, rather than the same type.

2.2.5 Time Correlated Pulse Height

The TCPH distribution is a bivariate histogram of the time difference between correlated neutrons and gamma rays, and deposited neutron energy measured by the light output in the scintillator [44]. In a non-multiplying source, such as Cf-252, most correlated neutrons and gamma rays that are detected within a short time window (10s of nanoseconds) by a fast system are generated from the same fission event. Therefore, the arrival time of a neutron, which depends on neutron incident energy, sets an upper limit on the light output achievable for that event.

The theoretical time between arrival of a gamma ray and a neutron from the same fission can

be determined from its energy:

$$t = \frac{d}{\sqrt{2E_n/M_n}} - \frac{d}{c} \tag{2.32}$$

where d, E_n, and M_n are the source-to-detector distance, energy of the neutron, and its mass, respectively. The d/c term is used to compensate for the arrival time of the gamma ray. However, in organic scintillators the kinematics of neutrons scatter on protons (hydrogen atoms), shown in Figure 2.5, limit the proton recoil energy to at most the incident energy of the neutron ($E_p \leq E_n$). Therefore, for a non-multiplying source, counts on the TCPH distribution will fall below this theoretical time of arrival line described by Eq. 2.32, as shown in Figure 2.6(a).

But multiplying sources make it possible to correlate neutrons to gamma rays from earlier fissions in a fission chain, which would make the time from the correlated gamma greater than the time predicted by Eq. 2.32. Even with the lesser energy deposition from the proton recoil, some counts would inevitably fall above this theoretical line of arrival. An example of the TCPH distribution of a multiplying source, along with the theoretical line of arrival line from Eq. 2.32 is shown in Figure 2.6(b).

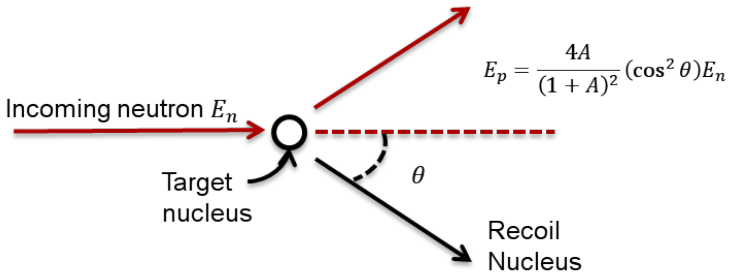

Figure 2.5: Kinematics of neutron scatter on hydrogen nucleus (proton) which is the primary mode of neutron detection in organic scintillators.

The utility of the TCPH distribution has been extensively studied with non-multiplying ^{252}Cf [41], low-multiplying mixed oxide powder and plutonium-gallium disks [42], and highly enriched uranium [45] measurements and simulations [43]. Simulations of the BeRP ball and the resulting TCPH distributions demonstrated a correlation between multiplication and spreading in the

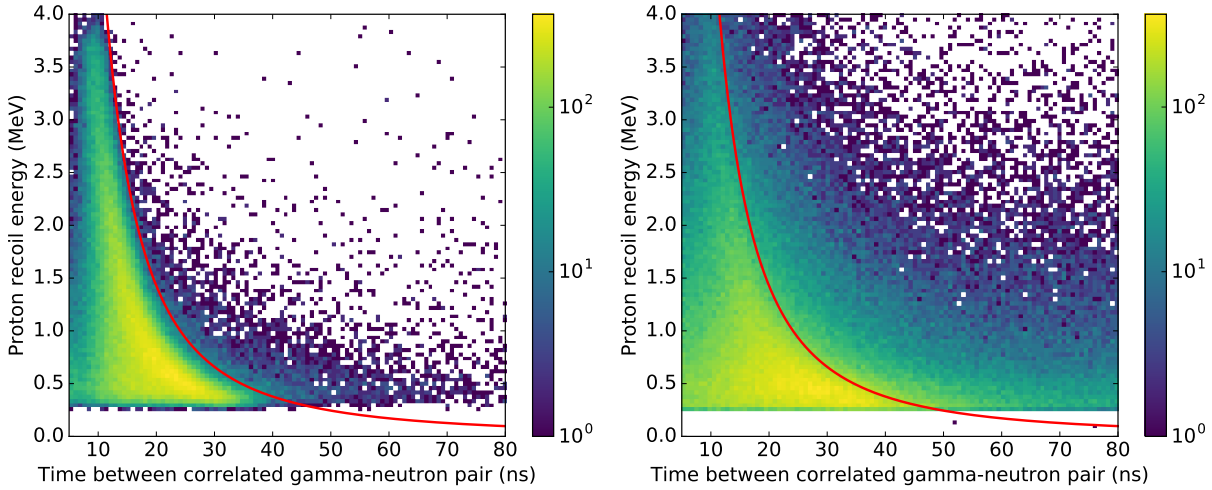

(a) Non-multiplying

(b) Multiplying

Figure 2.6: TCPH distributions for (a) non-multiplying and (b) multiplying sources with the theoretical line of arrival shown in red.

TCPH distribution [46]. In Chapter 4, the measured results are shown, along with a method for quantifying the spread in the TCPH distribution.

Earlier efforts to characterize multiplication relied on counting the correlated events that fell above the theoretical line of arrival, or estimating the gradient of counts above this line. But as will be shown in Chapter 4, the TCPH distribution is actually spread in both time directions due to presence of fissile material. The intermediate goal of this dissertation work was to determine other additional physical quantities of interest that could be extracted by examining the full TCPH distribution. The analysis will progress in Chapter 5 to collapse the TCPH distribution into the TOFFEE distribution, a simpler one-dimensional form which gives greater insight into the underlying fission chain dynamics measured from gamma-neutron correlations.

CHAPTER 3

Digital Pulse Processing

3.1 Motivation

The advent of fast Analog-to-Digital Converters (ADCs) has enabled the capture, storage and offline processing of scintillator waveforms after they are acquired [47]. This has allowed us to move beyond analog pulse-shaping techniques achieved through clever rearrangements of resistors and capacitors. Many digital processing techniques have their analog equivalents (e.g. filtering) [48], but digital processing also allows for any operation that a computer can do to a list of numbers. Therefore, it is important to explain the choice of appropriate digital processing techniques used to get the desired signature for time correlated analysis.

Three pieces of information are required about an interaction that gives rise to a pulse: time of the interaction, energy deposited by interacting particle and the type of particle by pulse shape discrimination (PSD). The challenge is to accurately extract that information when both the gamma ray and neutron interaction are necessary for analysis. The following serves as an overview of some of the available digital processing techniques applicable for pulses recorded from fast organic scintillators coupled to PMTs. The goal is to provide a detection system agnostic reference to processing methods required to replicate the results presented throughout this work.

3.2 Timing

Three candidate methods were investigated for their ability to reliably provide gamma and neutron interaction times: Derivative Zero Crossing (DZC), Constant Fraction Discrimination (CFD) and Cumulative Integral Fraction (CIF). The DZC method is often referred as the constant fraction discrimination method because it is how analog circuitry was used to find a constant fraction of a pulse [49]. The original pulse is operated on by the following:

$$\int \text{DZCPulse}[k] = \sum_{i=1}^{L} F * \text{Pulse}[k-i] - \text{Pulse}[k-i-D] \tag{3.1}$$

where a fraction F of the original pulse is subtracted by a pulse delayed by D. The time is then found by looking for the zero crossing past the maximum as shown in Figure 3.1.

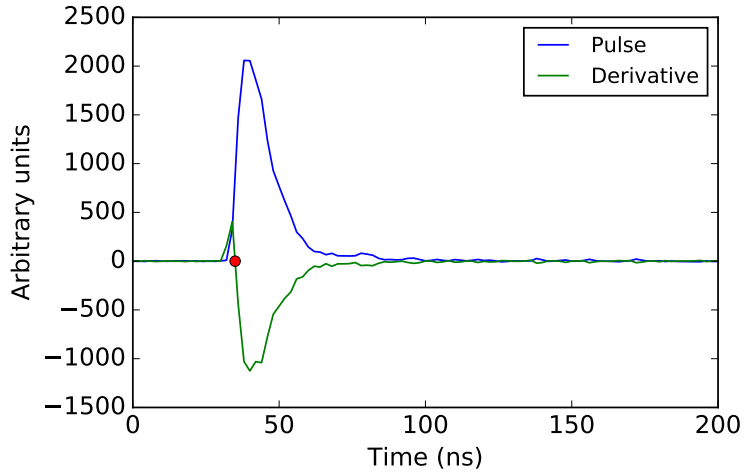

Figure 3.1: Example of a pulse and its derivative as calculated using the DZC method. The zero crossing time, marked by the red dot, is interpolated starting the the maximum of the derivative.

When D and F are both unity, DZC method amounts to taking the derivative of the original pulse, hence the naming convention adopted in this work. On the other hand the second method, CFD, relies on an intuitive implementation of the name “constant fraction". The time is found by interpolating the rising edge of the pulse up to some fraction of the pulse maximum. Finally, the third method, CIF, finds the time at some fraction of the cumulative integral of the pulse, as shown

in Figure 3.2. Trapezoidal integration method was used to better approximate the true pulse's integral.

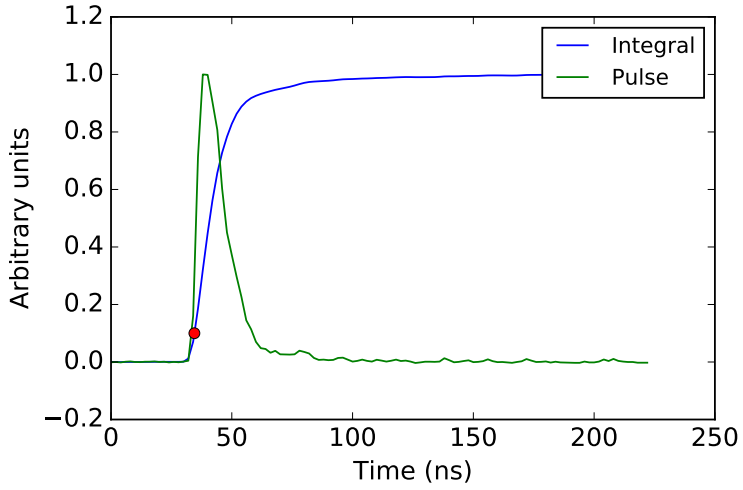

Figure 3.2: Example of a pulse and its cumulative integrals as calculated from the CIF method. The fraction of the cumulative integral (10%) used for time-pick-off is marked by the red dot.

Testing timing performance can be accomplished with pair of equivalent detectors and a source that emits coincident gamma rays. This setup allows for the measurement of the gamma-gamma Time of Flight (TOF) distribution, the width of which is indicative of timing performance. The spacial arrangement of the source and detectors is only important if it's necessary to measure the relative transit time of the PMTs coupled to each detector cell. In that case it's necessary to have the source be equal-distant to each detector. Each timing method has a fraction parameter, which was optimized to give the lowest achievable standard deviation and Full Width Half Maximum (FWHM) of the gamma-gamma TOF distribution. The delay was set to one ($D = 1$) for the DZC method.

The optimized TOF spectra for all three methods are shown in Figure 3.3. The FWHM was calculated via interpolation, and the standard deviation was taken from the entire set of ΔTs between -10 ns and 10 ns. In this case the standard deviation can not be taken as an absolute measure of detector system performance, since its value will change with the length of the time window. Note that the TOF spectra are not Gaussian in shape and the FWHM is not directly proportional

to the standard deviation. Nevertheless, these two metrics were used to optimize the fractions for each of the three methods. The optimized fractions for the DCZ and CFD methods were both at 50% and only 5% for the CIF method.

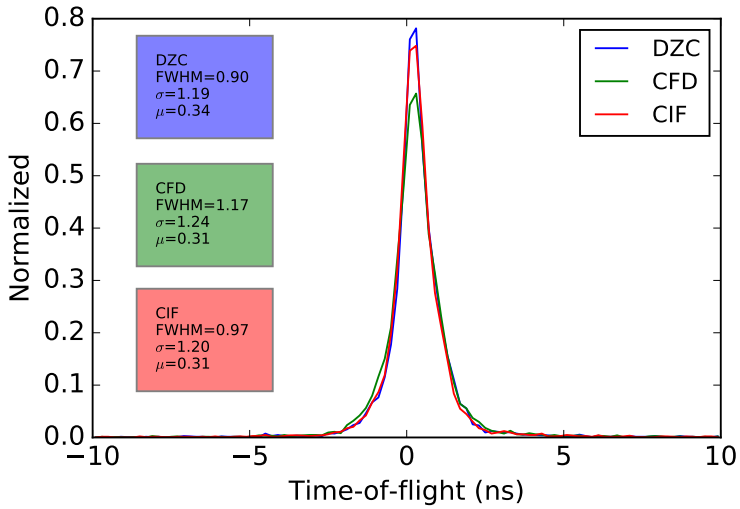

Figure 3.3: Gamma-gamma TOF spectra with optimized parameters for each of the three timing methods. The optimized fractions for the DCZ and CFD methods were both 50% and only 5% for the CIF method. The FWHMs, standard deviations and means are expressed in units of nanoseconds

In general, lowering the fraction decreased both the standard deviation and FWHM. The lower bound on the optimized fractions was dictated by the appearance symmetrical “resonance" peaks at the sampling rate of the digitizer. Since a 500 MS/s CAEN DT5730 digitizer was used for testing, those resonances peaks appeared at +2 ns and -2 ns intervals. Quantitatively the resonances would increase the standard deviation while the FWHM would continue to decrease.

At this point it may seem reasonable to conclude that each method is equally suitable for timing experiments. However, this dissertation primarily concerns mixed gamma-neutron correlations and when each method is compared against measured gamma-neutron TOF spectra, as shown in Figure 3.4, the flaw with the CIF method is revealed. Because the CIF method is pulse shape dependent, it will systematically over-estimate the arrival time of a neutron pulse as compared with a gamma ray pulse.

The gamma-neutron TOF spectra also revealed a problem with the DZC method, which was

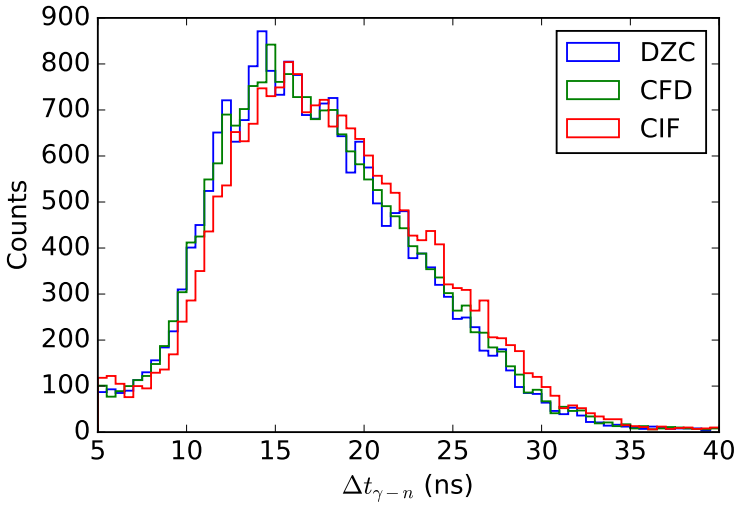

Figure 3.4: Gamma-neutron TOF spectra as calculated using the three timing methods. The data was taken from a measurement of a Cf-252 source at 30 cm distance from the pair of detectors.

not apparent int the gamma-gamma TOF spectra in Figure 3.3. Given a sufficiently high fraction, from Eq. 3.1, the resonances disappeared from the gamma-gamma TOF spectra, but persisted in the gamma-neutron spectra. The remaining resonances were diminished significantly by increasing the delay parameter D from one to two. The results comparing both DZC and CFD against simulation of the same Cf-252 source at 30 cm is shown in Figure 3.5. The chi-squared test statistics between the expected simulation and the observed measured results were 99.42 for DZC and 98.79 for CFD, and therefore neither method had the edge in matching simulation. Judging from this result, and the similarity in features shown in Figure 3.3, these two methods are almost indistinguishable. Furthermore, with an increased delay parameter, the spread of the gamma-gamma TOF standard deviation of the DZC came into agreement with the TOF spectra of the CFD method.

In conclusion, the three timing methods tested have similar performance, but CIF is not suitable for picking off timing from particles that result in different pulse shapes. The remaining two methods, DZC and CFD, are indistinguishable once their respective parameters are optimized. The CFD timing method was used for TCPH work in Chapter 4, and for DZC method was used for all other work presented in this thesis.

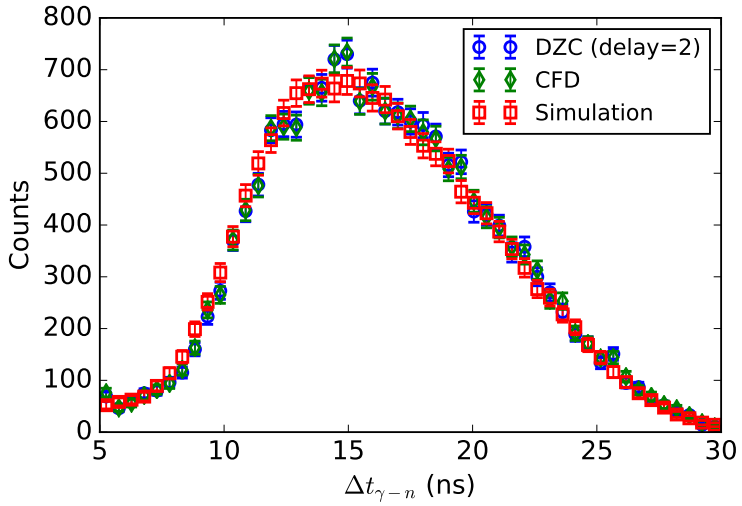

Figure 3.5: Comparison of simulation and measurement data of a gamma-neutron TOF spectra from a Cf-252 source at 30 cm from the detectors. The data was processed using two timing methods, DZC and CFD, with fractions set to 50%.

3.3 Energy Calibration and Resolution

For gamma ray spectroscopy the procedure for determining energy calibration and resolution typically involves fitting known full energy photo-peaks to Gaussian functions. The means and standard deviations of the fits are then used to determine the calibration and resolution of the system, respectively. Unfortunately, physics disallows such full energy photo-peaks in spectra gathered with organic scintillators due to the dominance of Compton scattering in low-Z materials, such as organic scintillator. The only recognizable features are therefore Compton edges corresponding to the maximum possible scattering angle:

$$E_{CE} = E\left(1 - \frac{1}{1 + \frac{2E}{m_e c^2}}\right) \tag{3.2}$$

where E is the incident gamma-ray energy and m_e is the resting mass of the electron. It is difficult to determine this edge accurately, because it's not clearly delineated on a pulse height spectrum due to a finite energy resolution and the effects of multiple scattering interactions.

One approach for estimating the location of the Compton edge is to fix its location at some

fraction of the Compton edge peak. A more robust approach is to fit the measurement results to a Monte Carlo simulation, with energy smearing term to account for energy resolution of the detector [50]. The measured pulse heights (PH) are shifted by linear calibration formula

$$L = a * \text{PH} + b \tag{3.3}$$

where L is the calibrated light output (in MeV) and a and b are calibration parameters. At the same time the simulated results are broadened by the approximate energy resolution of the system parameterized by

$$\frac{\Delta L}{L} = \sqrt{\alpha^2 + \frac{\beta^2}{L} + \frac{\gamma^2}{L^2}} \tag{3.4}$$

where α, β and γ parameters include contributions from light transmission within detector cell, statistical fluctuations of light production, and electronic noise, respectively [51].

The Levenberg-Marquardt algorithm was employed to find the optimum calibration and resolution parameters and an example of the results are shown in Figure 3.6. It is important to give extra weight to the regions of the spectra around the Compton edges, and to ignore the back-scatter peak, which is absent from the simulation due to lack of surrounding materials.

This spectrum matching technique is arguably more robust than using a fraction of the Compton edge peak, because it incorporates the detector resolution parameters, any improvement over this simpler method is probably marginal at best. In any case, the limiting factor is the relatively poor energy resolution of organic scintillators. In addition, the spectrum matching approach is complicated by the covariance between the energy calibration parameters in Eq. 3.3 and resolution parameters in Eq. 3.4. An improvement on this approach would require an independent method for measuring the resolution of the detector, such as the Compton coincidence technique [52].

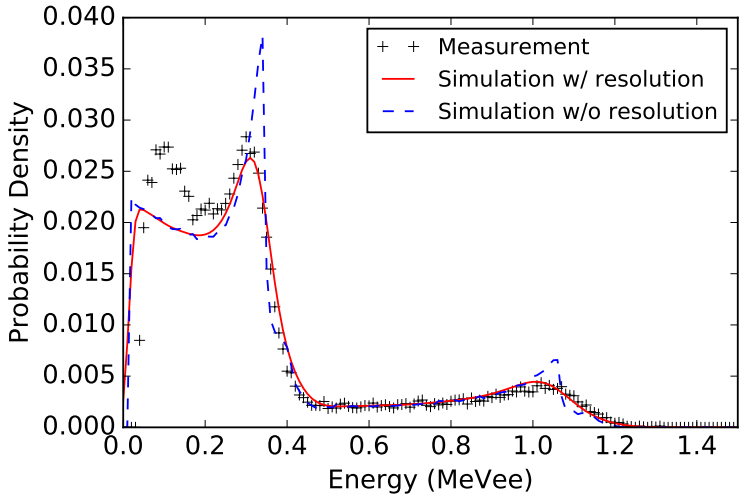

Figure 3.6: Measured and simulated spectra of Na-22 source matched with optimum resolution and calibration parameters.

3.4 Neutron Light Output

The amount of light emitted from an interaction in a scintillator depends on the energy deposited and the type of recoiling charged particle. For gamma rays these charged particles are electrons and for neutrons they are predominantly protons (hydrogen nuclei). In many organic scintillators, electrons provide a near-linear response at energies greater than 125 keV [53], which justifies linear energy calibration used in Eq. 3.3. However, since the light output response from protons is different than electrons, it is useful to refer to this electron light output in terms of MeV electron equivalent (MeVee). This unit, introduced in Figure 3.6, provides an absolute measure of the light output that is useful for characterizing light output caused by proton recoil in terms of its electron equivalent energy.

There are two problems with neutron light output response that make it challenging. First, unlike the electron response the proton response is non-linear, which necessitates multiple calibration points. Second, with exception of deuterium-deuterium (2.5 MeV) and deuterium-tritium (14.1 MeV) fusion neutron generators there is a lack of portable mono-energetic sources of neutrons. A popular approach to characterize the neutron light output response is through time-tagged experiments; where the incident neutron energy can be segregated through time-of-flight [54–56]. For

organic scintillators, it's common to fit the neutron response to an empirical exponential formula first developed by Katz [57]:

$$L(E_p) = aE_p - b[1 - \exp(-cE_p^d)]. \tag{3.5}$$

The coefficients a, b, and c are often reported in terms of units of MeVee/MeV, and d is typically assumed to be unity and is a dimensionless constant [54, 55, 58, 59], and provided that the calibration methodology is the same, can be used universally for detectors of the same geometry and size. The formulation in Eq. 3.5, and its inverse, will be used for analysis in Chapter 4.

A more physical insight into light output yield can be gained by relating the dL/dx, fluorescent energy emitted per unit path length, and dE/dx, energy loss per unit path length for a specific particle [60]. This relationship is commonly referred to as the Birks' formula

$$L(E_p) = S \int_0^{E_p} dE \left[1 + k\frac{dE}{dx}\right]^{-1} \tag{3.6}$$

where S is the normal scintillation efficiency and k reflect the effect of quenching. The requisite dE/dx for electrons and protons in stilbene were calculated using SRIM software [61, 62], and provided by personal correspondence by Mark Norsworthy [63]. Scintillation efficiency refers to the fraction of incident particle energy that is converted to visible light, and is degraded by quenching which is an umbrella term for all the de-excitation pathways that do not lead to emission of light. Birks' formula has been found to work better at lower thresholds ($<$100 keV) than the empirical function in Eq. 3.5 [63, 64], but it requires the knowledge of the stopping power of charged particles for the material of interest. A comparison of the fit to the two formulations for data obtained from solution grown 2"$\times$2" stilbene [65] is shown in Figure 3.7. The neutron light output yield for 2" stilbene crystals was measured by Bourne et al. in a separate set of experiments [65]. Birks' formula fit was used in this thesis for all the data acquired with and simulations of 2"$\times$2" stilbene.

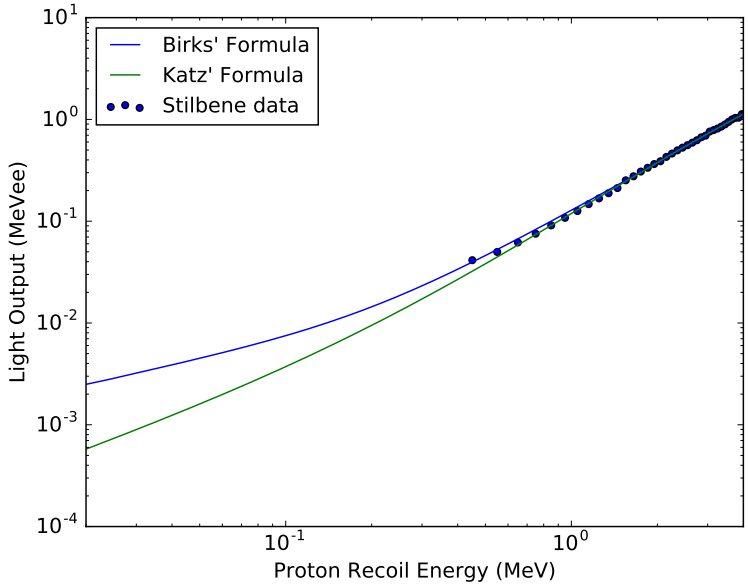

Figure 3.7: A 2"×2" stilbene crystal neutron light output data fit to Birks' and Katz's formulations. The Katz coefficients are $a = 0.505$, $b = 1.072$, $c = 0.446$, and $d = 1$, and the Birks coefficients are $S = 1.63$ and $k = 27.83$.

3.5 Pulse Shape Discrimination

In organic scintillators the fraction of light emitted during delayed fluorescence depends on the exciting particle's dE/dx, therefore it is possible to differentiate between neutron and gamma-ray interactions through PSD. Segregating gamma ray and neutron pulses is a two step process. First, the pulse shape is quantified into some singular quantity called the PSD parameter. Then the PSD parameter is used to quantitatively separate neutron and gamma ray pulses, typically on an energy dependent basis. It is the novel application of Bayes' theorem to this second classification step that was extensively used throughout this dissertation work to maximize the return on gamma rays and neutrons. The details of the comparative performance of this method can be found in [66].

3.5.1 Pulse Shape Quantification

The charge integration PSD method, in both analog and digital applications, relies on the ratio of pulse tail to total integrals [67] as shown in Figure 3.8. This PSD parameter is widely used in comparing PSD performance in organic scintillators [68–70]. An alternative approach used

in this work relies on taking the difference in time between fractions of the pulse integral. This amounts to using the CIF method, shown in Figure 3.2, twice for two different fractions and taking the difference of the results. This approach has the advantage of requiring only two parameters, one less necessary for specifying the tail and total integration windows for the charge integration method.

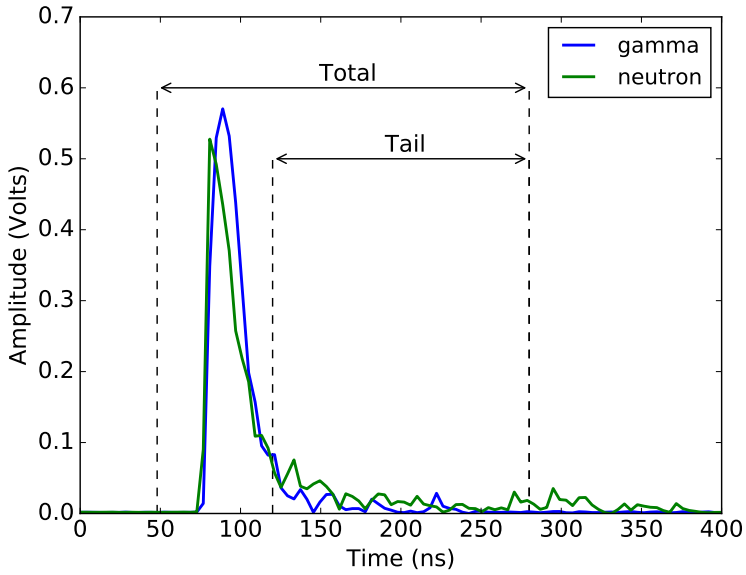

Figure 3.8: Example of tail and total integration windows used in the charge integration method.

There are other methods for quantifying PSD parameters [71], all of which provide a way of clustering neutrons and gamma rays in a particular two dimensional space. Typically, one dimension of this space is the PSD parameter, and the other is some metric of energy deposition such as pulse height or pulse integral. The two clusters of gamma rays and neutrons can be cleaved with a decision boundary, which provides a binary classification of each pulse. The following section demonstrates an alternative Bayesian approach, which gives confidence probabilities on an event-by-event basis. This allows for re-adjustment of the PSD “cut" by adjusting the minimum allowed probabilities in post-processing.

3.5.2 Bayesian Classification Methodology

Applying Bayes' theorem requires a conditional probability, or likelihood, and a prior probability. In this method, the former is defined as the value of an energy dependent Gaussian fit for a given tail-to-total ratio and the latter as the energy dependent gamma-to-neutron ratio. The discussion on estimating both parameters proceeds in the following two sections. Initially, the prior probability is not known and thus it must be inferred from the data by an iterative procedure. Therefore, the Bayesian probability is adaptive to a particular collection of data.

The Bayesian method and an experimental study of its performance relative to a decision boundary technique have been previously published in [66]. The following overview demonstrates the method only, which was used throughout the work in this thesis to classify neutron and gamma-ray pulses. Appendix A.2 includes the source code that employs the Bayesian method for PSD.

3.5.2.1 Fitting detector specific parameters

The first step is to determine the detector specific parameters, the means and standard deviations, from a double Gaussian fit to the PSD parameters. This step should preferably be accomplished on a data-set with nearly equal gamma ray and neutron populations. These parameters are energy dependent, therefore the data has to be binned into specific light output groups. The groups have to be narrow enough to capture the changing means and standard deviations, but wide enough to include statistically significant number of counts to perform an accurate fit. The number of counts decreases with increasing light output, but fortunately the variations in the means and standard deviations also decrease with increasing light output, as is shown in Figure 3.9, and therefore can accommodate larger light output bin widths. These parameters are only system dependent, and like gain calibration procedures, only need to be performed once for a particular experiment.

Each binned group of PSD parameters was fit in descending order of light output, with the previously calculated coefficients used as the next initial guess. This ensured continuity of the coefficients across all groups, and facilitated the precarious fitting at lower light outputs where distributions overlap the most. The Gaussian distributions were normalized and took on the familiar

form:

$$f(s) = \frac{1}{\sigma\sqrt{2\pi}} \exp\left(-\frac{(s-\mu)^2}{2\sigma^2}\right) \tag{3.7}$$

where s is the PSD parameter.

In order to calculate the Bayesian probability for each pulse individually, the Gaussian coefficients were fit across the light output range of interest. Smoothing splines were used to approximate the mean and standard deviation coefficients as a function of light output. The resulting R-squared values were greater than 0.99 for all fitted parameters. The result of the fitting procedure is shown in Figure 3.9, as applied to a subset of data collected with an Am-Be source. The details of the experimental setup are given in [66]. Conditional probabilities for the Bayesian formula were taken from these fits.

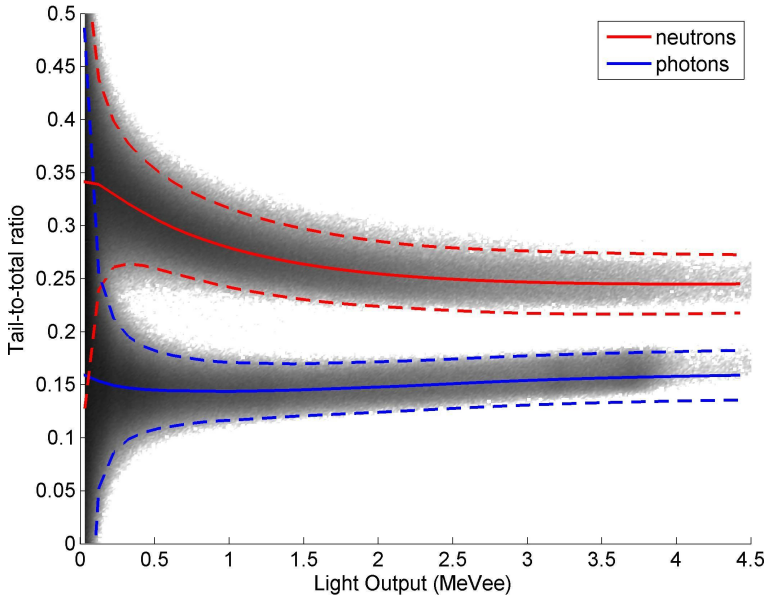

Figure 3.9: The mean (solid lines) and three standard deviation (dashed lines) fits as applied to the Am-Be data set.

By fixing the mean and standard deviation parameters from a calibration data set, the assumption is that they only depend on the detector system, and therefore do not need to be refitted for other measurements.

3.5.2.2 Inferring the gamma-to-neutron ratio

The Gaussian fits provide the conditional probabilities, but a prior is required in order to calculate a gamma-ray or neutron posterior probability. In this case the prior is the energy dependent ratio of gammas-to-neutrons, which will change depending on the incident radiation (i.e. the type of radiation source measured). Therefore, an iterative procedure is introduced that updates the gamma-to-neutron ratio by recalculating posterior probabilities until a convergence criteria in the gamma-ray and neutron populations is met.

The following formulation of the Bayes' theorem was used for calculating posterior probabilities for either gamma rays

$$P(\gamma|s) = \frac{f_\gamma(s)R_{\gamma/n}}{f_\gamma(s)R_{\gamma/n} + f_n(s)} \tag{3.8}$$

or neutrons

$$P(n|s) = \frac{f_n(s)}{f_\gamma(s)R_{\gamma/n} + f_n(s)} \tag{3.9}$$

where $f(s)$ are the Gaussian fits from Eq. 3.7, the γ or n index indicates the gamma-ray and neutron distribution and s is the PSD parameter. $R_{\gamma/n}$ is the ratio of the estimated number of counts in the gamma-ray and neutron distributions within a light output group. The number of instances of gamma rays and neutrons is estimated by summing the posterior probabilities of each class

$$N_\gamma = \sum_{s \in E_i} P(\gamma|s) \tag{3.10}$$

$$N_n = \sum_{s \in E_i} P(n|s) \tag{3.11}$$

for a particular light output group E_i.

For the first iteration $R_{\gamma/n}$ is assumed to be unity, then the results from Eqs. 3.8 and 3.9 are used to estimate its value for the subsequent iteration:

$$R_{\gamma/n} = \frac{N_\gamma}{N_n}. \tag{3.12}$$

The iterative approach used is an example of an expectation-maximization algorithm for Gaussian mixtures [72] with fixed means and standard deviations. Iterations terminate when the convergence criteria is satisfied. Convergence criteria was defined as 1% difference in total $R_{\gamma/n}$ between two consecutive iterations. This iterative scheme is robust, and converges to the same solution given a wide range of initial $R_{\gamma/n}$. The final result are posterior probabilities, as shown in Figure 3.10, which can be used to adaptively classify pulses.

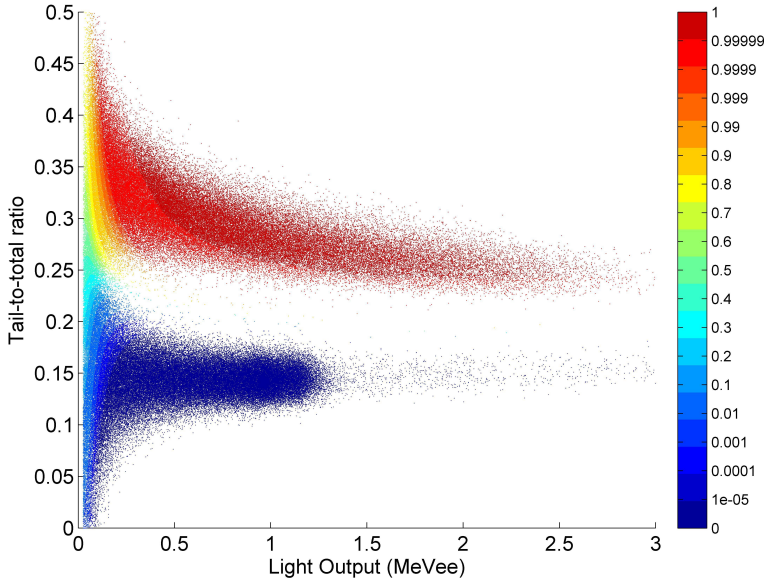

Figure 3.10: The distribution of neutron posterior probabilities for 1:1 mixture of ^{60}Co and time tagged neutron data.

3.5.2.3 Variance estimation

Since the sum of probabilities, not counts, is used to estimate the size of gamma-ray and neutron populations, a different formulation from counting statistics is required to account for the uncertainty of the posterior probability itself. In this work the variance on the total number of estimated

instances N was calculated by

$$Var(N) = \sum P_i + \sum P_i(1 - P_i) \tag{3.13}$$

where P_i are either gamma ray or neutron posterior probabilities for each pulse. N represents the number of gamma ray or neutron instances as calculated by Eqs. 3.10 and 3.11. The first term in Eq. 3.13 sums to N and represents the variance on the total number of counts. The second term is the variance on each individual probability, which follows a binomial distribution because there are only two classes, gamma rays and neutrons. In the limit that all the P_i are large, the variance estimation reduces to N. On the other hand, if P_i are small, then the variance estimation is effectively doubled to $2N$.

CHAPTER 4

Time Correlated Pulse Height Distributions

4.1 Motivation

The details of the TCPH distribution and its relation to characterizing fissile material were introduced in Section 2.2.5. The analysis pioneered by Miller et al. focused on the counts that lay above the theoretical line of arrival. This stemmed from the observation that in the presence of fission chain neutrons from later generation events could be correlated with earlier gamma rays, hence increasing the time between the two correlated events [42]. This misses the corollary observation, which is that neutrons from earlier fission events can be correlated with later generated gamma rays. Therefore, the time of arrival is either shorter or longer depending on the order of the generation along the fission chain of the correlated gamma-neutron pair. In a multiplying assembly of fissile material this effect manifests itself as a spreading or smearing of the TCPH distribution, not just increased counts above the theoretical line of arrival.

To characterize this behavior, a new method had to be developed to quantify the smearing of the whole TCPH distribution. The method and experimental results were first published in [73], and this Chapter summarizes that approach and results. The underlying assumption of the method is that the smearing is caused by the time distribution of fission events within a chain. The approach in this Chapter uses the Gamma function as an empirical approximation for this smearing distribution. The goal is to fit empirical parameters of the Gamma function that correlate with the underlying fission chain timing distribution. These empirically fit parameters were found to correlate with

multiplication, shielding material types and source-to-detector distance. They provided another handle on the characterization of fissile material that would be useful in warhead dismantlement confirmation, where knowledge of the presence of the coupled material might be useful to confirm that surrounding moderating material has been removed. The application of a variation of the TCPH distribution for treaty verification is explored in Chapter 5.

4.2 Analytical Model

In order to access the fission chain timing distribution, a model was constructed of TCPH distributions for multiplying sources. The model consists of a linear combination of the expected distribution for gamma-neutron pairs that are correlated by the same-fission and those correlated by different fissions within the same chain.

The “same-fission" distribution is determined by a combination of the detector response to fission spectrum neutrons (Watt) and the time delay expected for the source-to-detector distance. The detector response matrix was simulated using MCNPX-Polimi [74]. Pu-239 fission Watt spectrum was assumed for energies of incident neutrons and Katz's formula, from 3.5, was used for the light output function [55]. The simulated neutron response matrix and the resulting same-fission TCPH distribution are shown in Figure 4.1

The different-fission distribution includes additional time smearing due to the time difference between any two fissions within a chain. A physical model of the fission chain process is outside the scope of this Chapter, it will be introduced in Chapter 6. Therefore, the Gamma function was used as an empirical substitute for the physical model of the time distribution of fission events in a chain.

The probability density function of a Gamma distributed random variable is

$$f(x) = \frac{1}{\Gamma(\alpha)\theta^{\alpha}} x^{\alpha-1} e^{-x/\theta} \tag{4.1}$$

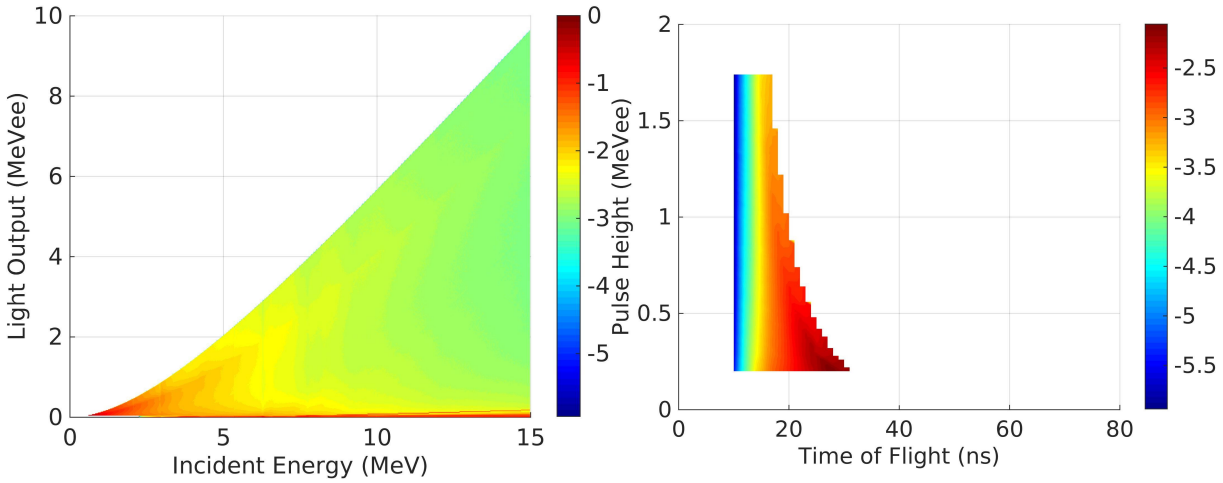

(a) Response Matrix

(b) TCPH Distribution

Figure 4.1: Simulated EJ-309 neutron response matrix and the resulting TCPH distribution with assumed ^{239}Pu Watt neutron energy spectrum and source-to-detector distance of 50 cm. Each distribution is normalized to unity and displayed on a logarithmic scale.

where α is the shape parameter and θ is the rate parameter. Two properties of the Gamma function make it a plausible representation for the distribution of times between fission events. First, the Gamma function describes the waiting times until the α^{th} Poisson distributed event. Second, the sum of independent Gamma distributed events follow a Gamma function. The independence condition is not true for events in a fission chain; however, it can be empirically demonstrated that the time distribution between fission events roughly follows a Gamma function by comparing MCNPX-PoliMi simulations. The simulated distribution of time differences between fission events in a bare BeRP sphere and corresponding Gamma function fits are shown in Figure 4.2. Although the time distribution between a set number of fission events follow a Gamma function, with coefficient of determination (R^2) between 0.930 and 0.949, the fit for all possible fission combinations has R^2 of 0.997. The Gamma function fits systematically undershoot the peaks of the time difference distributions from simulation, because those distributions are generally narrower. The smaller variance in those time differences from simulation is due in part to the fact that fission events in a chain are correlated. The other phenomena not captured by the Gamma function is branching of a fission chain, which makes it possible for fission events in different generations to

be closer in time than expected from a straight linear succession of fissions in a chain.

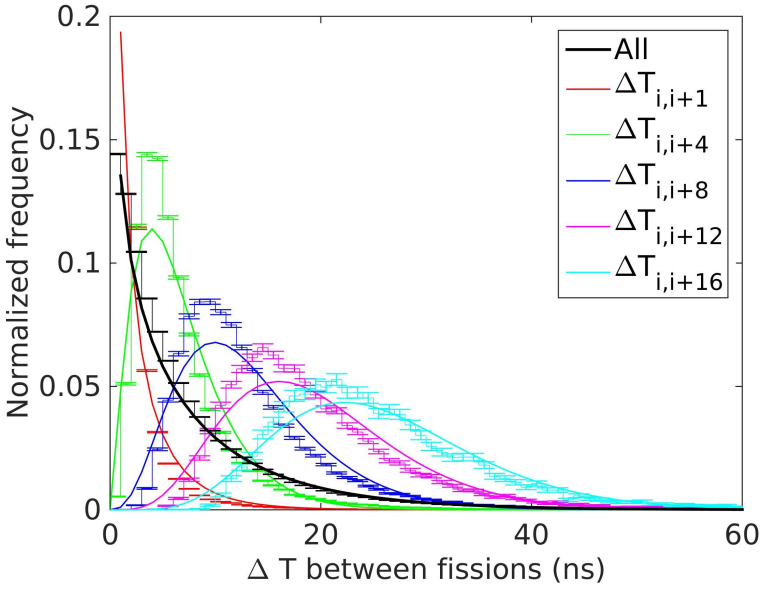

Figure 4.2: Distribution of time differences for various nth-nearest-neighbor fission events is represented by each colored line, with the black line showing the distribution between all fission events in a chain. The distributions were obtained from an MCNPX-PoliMi simulation of bare BeRP ball (stairs) and then normalized to unity and fit by Gamma functions (solid lines).

Finally, the TCPH distribution for a multiplying source is constructed using a linear combination of the non-multiplying TCPH distribution, as shown in Figure 4.1(b), and a TCPH distribution smeared by the Gamma function. The smearing is accomplished by setting each bin on the TCPH distribution equal to the sum of neighboring bins along the time axis, with a weight given by the Gamma function for the time delay between bins. Included in the sum is the contribution of the original same fission bin weighted by factor n.

The factor n represents the fraction of correlated pairs from like fissions over all fission and in theory should be proportional to the length of fission chain L:

$$n \propto \frac{L}{\binom{L}{2}}. \tag{4.2}$$

By definition the average length of the fission chain is related to the sub-critical multiplication from Eq. 2.9 such that $M = (\bar{L} - 1)$.

A conditional statement is added to the Gamma function to account for n:

$$F(x|\alpha,\theta,n) = \begin{cases} f(x|\alpha,\theta) & \text{if x} > 0 \\ n & \text{otherwise.} \end{cases} \tag{4.3}$$

where $f(x)$ is defined in Eq. 4.1. The smeared TCPH distribution is calculated by

$$\boldsymbol{M} = \boldsymbol{N} \times F(\boldsymbol{A}) \tag{4.4}$$

where $\boldsymbol{N}$ is a pulse height by time matrix of the same-fission TCPH distribution. The matrix $\boldsymbol{A}$ is a symmetric Toeplitz matrix with the first row defined as the cumulative difference between the times in the TCPH distribution $\boldsymbol{N}$. In this case, the function F performs a point-wise operation on values in matrix $\boldsymbol{A}$.

The resulting TCPH distribution $\boldsymbol{M}$ depends on α, θ and n which define how the distribution is smeared, and the distance from the detector which shifts the non-multiplying TCPH distribution $\boldsymbol{N}$. If the distance is known it can be fixed, otherwise it can be included as a free parameter with the other three parameters. To solve for the parameters, the loss function is defined as the root-mean-square error (RMSE) between the modeled TCPH distribution $\boldsymbol{M}$ and a measured distribution. This function is then minimized by employing an unconstrained non-linear optimization method based upon the Nelder-Mead simplex algorithm [75, 76].

The parameters of interest are solved in three steps. In the first and the final third step all four parameters are optimized, and in the intermediate second step the source-to-detector distance is fixed. In between the steps the initial guesses are changed to the previous solutions. The Nelder-Mead simplex algorithm works best with fewer parameters, therefore by reducing their number in the middle step the Gamma function parameters could be further optimized. The distance parameter was fixed because it proved to be the most well constrained with the smallest relative covariance with respect to the other parameters.

4.3 Experimental Setup

A series of measurements of the BeRP [77] ball were conducted at the Nevada National Security Site (NNSS) to acquire data to assess TCPH distribution analysis for highly multiplying assemblies of fissile material. The BeRP ball is a 4.5 kg sphere of α-phase WGPu metal, original manufactured in October 1980 by Los Alamos National Laboratory [77]. To explore a range of multiplications with different levels of moderation and reflection, five configurations were measured: bare, 1.27 cm and 2.54 cm thick close fitting shells of tungsten, and 2.54 cm and 7.62 cm thick close fitting shells of high density polyethylene (HDPE). The measurement times for each configuration were 5515, 3600, 8999, 3600, and 2509 seconds, respectively.

Data were collected using four 7.62$\times$7.62 cm cylindrical EJ-309 liquid scintillation detectors. The source-to-detector distances were measured from the center of the BeRP ball. Most configurations were measured at 50 cm distances with the exception of 2.54 cm tungsten and polyethylene measured at 48 and 60 cm, respectively. A diagram of the experimental setup, taken from an MCNPX-PoliMi model, is shown in Figure 4.3. Anode outputs from 7.62 cm Electron Tubes photomultiplier tubes (PMTs) coupled to each cell were digitized using CAEN DT5720 digitizer, capable of 12-bit (nominal) resolution and 250 MHz sampling rate. All data processing was performed off-line after the measurements, and a 0.2 MeVee (MeV electron-equivalent), equivalent to neutron energy of 1.2 MeV, threshold was applied in post-processing.

4.4 Measurement Results

A subset of the measured TCPH distributions and corresponding optimized models built from best-fit parameters are shown in Figure 4.4. The same-fission TCPH distribution, shown in Figure 4.1(b), is smeared to produce TCPH distributions shown in subfigures (b), (d) and (f) of Figure 4.4. The smearing parameters are optimized in order to match the measured TCPH distribution shown in subfigures (a), (c) and (e) of Figure 4.4.

The optimized Gamma function parameters and factors of n are shown in Table 4.1. It is

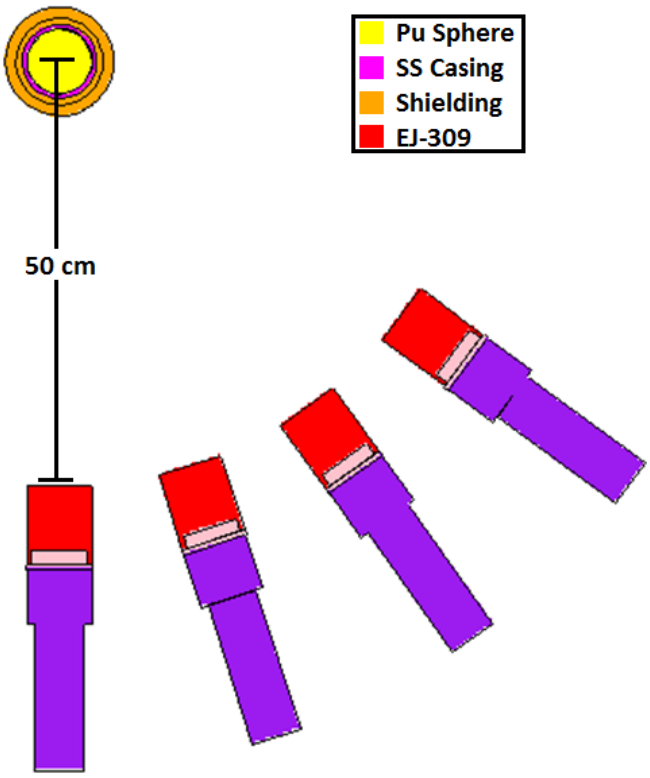

Figure 4.3: Diagram of the experimental setup of the BeRP ball surrounded by four EJ-309 detectors. The detectors were spaced approximately 8.5° apart.

expected that the parameter n would decrease with increasing sub-critical multiplication given its relationship to fission chain length in Eq. 4.2. This trend is apparent within each shielding material configuration, but is not present between them. Furthermore, the relative uncertainty in this parameter is over five times greater than the others, which limits its predictive capability.

The shape parameter, α, clearly demarcates the differences between the polyethylene moderator and tungsten reflector. Although α has no obvious physical interpretation when its a non-integer less than 1, it is valuable that it can distinguish between intervening material type independently of multiplication.

It is also expected that the rate parameter, θ, would increase with multiplication because it is proportional to the degree of smearing of the TCPH distribution. The corollary to this is the measure of the gradient of the TCPH distribution found in [42]. This positive correlation is only apparent for the tungsten case, and is actually negative for the polyethylene. The negative correla-

tion in polyethylene was unexpected, but the difference in source-to-detector distances between the two polyethylene measurements could be a factor. The greater distance increases the time between correlated gamma rays and neutrons, and therefore somewhat smears out the TCPH distribution. However, this effect is incorporated into the analytical TCPH model that is used for fitting. The other factor to consider is that the two polyethylene measurements were performed on different experimental campaigns. The source-to-detector distance is the only noted difference between the two measurements, but that does not exclude any other systematic differences that could arise from setting up measurements on different days. In Section 4.5 it is shown that for simulated polyethylene cases the rate parameter is positively correlated with multiplication, as expected.

Table 4.1: Optimized Gamma function parameters for the five measured configurations of the BeRP sphere with standard errors of 1 standard deviation shown [73].

case	α	θ	n	Multiplication
bare	0.57 ± 0.04	12.41 ± 0.62	0.08 ± 0.03	4.429 ± 0.002
1.27 cm W	0.87 ± 0.04	14.91 ± 0.63	0.11 ± 0.03	6.447 ± 0.004
2.54 cm W	0.90 ± 0.02	19.67 ± 0.53	0.06 ± 0.01	8.752 ± 0.006
2.54 cm HDPE	0.48 ± 0.03	26.74 ± 1.38	0.08 ± 0.03	7.743 ± 0.005
7.62 cm HDPE	0.53 ± 0.03	22.54 ± 0.91	0.07 ± 0.02	20.3 ± 0.2

The optimized source-to detector distances are shown in Table 4.2. Multiplication values were calculated from MCNP5 simulations of each configuration [7]. In all cases the optimized distance was smaller than the measured distance, with the greatest discrepancy present in the thicker tungsten case. This suggests that this effect may be due to self-shielding; correlated particles from fission events closer to the surface of the BeRP ball on the side of the detectors are more likely to be detected. Therefore, any additional high-Z material would preferentially favor gamma rays born at the surface of the BeRP ball, which would decrease the optimized source-to-detector distance. This effect is seen in simulation, where the source-to-detector distance decreases significantly for increasing tungsten reflector thickness but remains only slightly altered for low-Z polyethylene moderator.

Table 4.2: Optimized distances for the five measured configurations of the BeRP sphere with standard errors of 1 standard deviation. The measured distance was measured from the center of the BeRP ball to the face of the detectors.

case	optimized distance (cm)	measured distance (cm)
bare	49.02 ± 0.06	50 ± 0.5
1.27 cm W	49.04 ± 0.12	50 ± 0.5
2.54 cm W	44.75 ± 0.11	48 ± 0.5
2.54 cm HDPE	59.72 ± 0.09	60 ± 0.5
7.62 cm HDPE	49.25 ± 0.09	50 ± 0.5

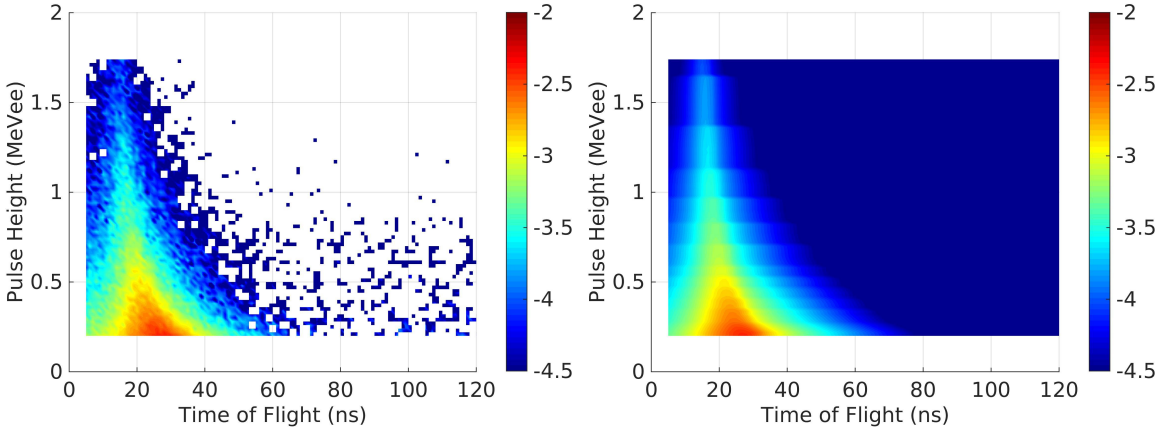

(a) Bare measured

(b) Bare model

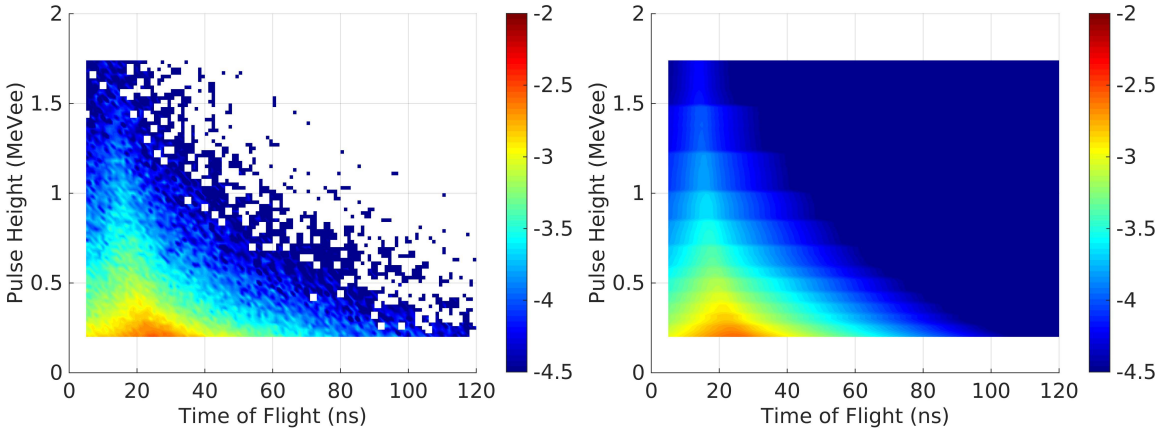

(c) 2.54 cm W measured

(d) 2.54 cm W model

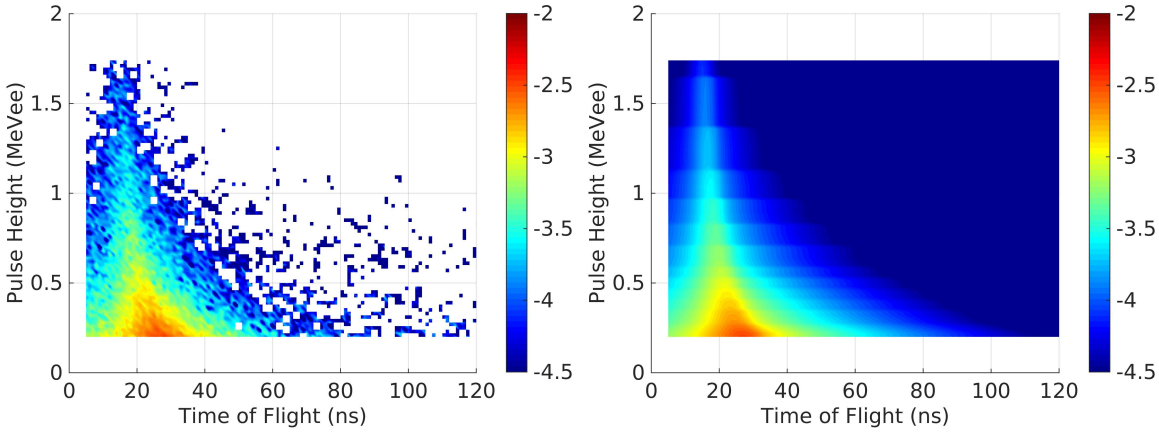

(e) 7.62 cm HDPE measured

(f) 7.62 cm HDPE model

Figure 4.4: Measured TCPH distributions (left) and corresponding models with parameters from the minimization algorithm (right) for various BeRP ball configurations.

4.5 Simulation Results

MCNPX-PoliMi simulations with shielding configurations of 1.27-7.62 cm for polyethylene and 1.27-7.62 cm for tungsten in 1.27 cm intervals were simulated to better illustrate the trends in the TCPH distribution. The optimization results of the shape and rate parameter for both simulations and measurement are shown in Figure 4.5, with multiplication proportional to the area of each marker.

The standard errors were taken from a covariance matrix of the best-fit parameters derived from a numerical estimation of the Jacobian. There are considerable absolute differences between measurement and simulation, but the general trends remain the same with the notable exception of the aforementioned measured polyethylene cases. The simulations reveal that it would be possible to measure the relative change in multiplication, independently of the change of surrounding moderator for a reflector or vice versa. The main driver in the size of the relative standard errors was the number of total correlated gamma-neutron pairs. This is most apparent for the thick tungsten cases which effectively shield the vast majority of fission gamma rays.

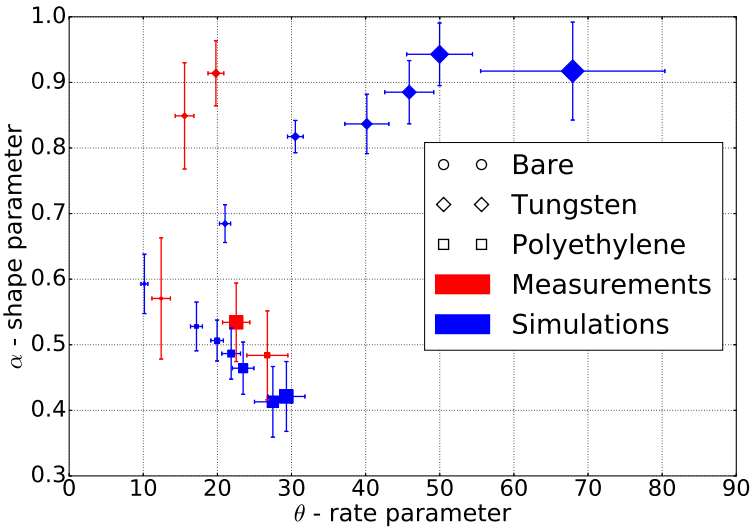

Figure 4.5: Optimized shape and rate parameters for both simulation (blue) and measurement (red) cases. The shielding configurations varied in thickness from 1.27-7.62 cm with 1.27 cm intervals. The increase in symbol size corresponded to an increase in multiplication, which is proportional to the area of each marker. Note that the bare configurations are furthest to the left for both measurements and simulations.

4.6 Conclusions

This Chapter introduced a new approach for the characterization of SNM based on a signature of temporally correlated gamma rays and neutrons. The approach was to fit the empirical approximation of the timing distribution between fissions in a fission chain to the measured TCPH distribution. It was shown that for the BeRP ball these empirical parameters correlate with both multiplication and the type of material (e.g. low-Z moderator or high-Z reflector) coupled to the fissile assembly. This property makes this method a candidate for treaty verification applications, where confidence in warhead dismantlement is the objective. In this case warhead dismantlement would involve the removal of high explosives, which is a form of moderating material, from the fissile material of a warhead. The reliance on a signature that is unique to SNM makes it more difficult to spoof dismantlement of fissile material. Furthermore, the signature used can be captured with a portable set of fast organic scintillators which could be carried by an inspector.

Though the Gamma function was shown to reproduce the measured TCPH distributions in bare fissile assemblies, as increasing amounts of reflector were added, it became a less relevant proxy for the complete effect of the fission chain dynamics. Despite this, the rate parameter of the optimized Gamma function correlated positively with multiplication. Simulation results revealed this trend, but it was not shown to be the case for the measured polyethylene cases. This multiplication-rate parameter relationship followed a different trend-line for moderated and reflected systems; which were easily identified by the shape parameter.

For this work, an empirical model was utilized to identify general trends in the fissile assemblies. However, if this were replaced by a physical model of the timing distribution of fissions within fission chains, then it may be possible to further improve the available information present in this signature. Furthermore, the TCPH distribution is a representation of the raw signatures: time between correlated neutrons and gamma rays, and the energy deposited by the incident neutron. The underlying signature that captures the fission chain dynamics is missed in this form. In the subsequent Chapters these raw signatures will be transformed into more physically meaningful and easier to work with 1D TOFFEE distribution.

CHAPTER 5

Time of Flight Fixed by Energy Estimation

5.1 Motivation

In Chapter 4 it was shown that the TCPH distribution is sensitive to the change in multiplication that arises from the presence of reflector/moderator around fissile material. This signature is unique to fissile material as it relies on underlying fission chain dynamics. Furthermore, it can be measured with a relatively small detection system that can be made to be portable. These attributes make this signature and analysis a useful choice for applications such as treaty verification, where the claim of warhead dismantlement and initial warhead count has to be certified.

However, the TCPH distribution is essentially the raw representation of gathered recorded times between correlated gammas and neutrons, and the corresponding light output from the neutron interaction. Comparing changes in this 2D distribution is made difficult by the lower statistics per bin, as compared to a 1D distribution with the same number of total counts. Therefore, it would be advantageous for both comparative and quantitative analysis to reduce the dimensionality of the measured distribution while still using the information gained from the light output of the neutron interaction. This goal was accomplished by using a new Time-Of-Flight Fixed by Energy Estimation (TOFFEE) distribution. The derivation of this new TOFFEE distribution, and its application as a template analysis for potential application to treaty verification is discussed in this Chapter. The application of TOFFEE for treaty verification was first presented at the 57^{th} annual Institute of Nuclear Materials Management conference [78].

5.2 TOFFEE Definition

TOFFEE is the measured time between correlated gamma rays and neutrons adjusted by the expected TOF of the neutron and gamma ray from the point of emission to the detector. The incident neutron energy, E_n, is estimated by the energy deposited in the detector as determined by the elastic scatter on a proton, E_p. Because the neutron typically deposits only a fraction of its energy in this interaction, this estimated energy will be systematically low and thus the estimated neutron TOF will be systematically too large. With a known source-to-detector distance d, it is possible to estimate the travel time difference between a neutron and gamma ray emitted simultaneously:

$$t_p = d\left(\sqrt{\frac{m_n}{2E_p}} - \frac{1}{c}\right) \tag{5.1}$$

where c is the speed of light and m_n is neutron's mass. The calculated quantity t_p is therefore the estimated difference in neutron and gamma-ray time of flight difference from the proton recoil energy. Since E_p is systematically smaller than the true incident neutron energy, t_p will overestimate the true time of flight difference between the neutron and gamma ray. Finally, the "fixed" in TOFFEE refers to subtracting this quantity from the measured time between a gamma ray and neutron pair, $t_{n,\gamma}$.

For non-multiplying sources (e.g. spontaneous fission or (α, n)), the actual travel time difference between a gamma ray and a neutron, $T_{n,\gamma}$, will equal the measured $t_{n,\gamma}$, as shown in Figure 5.1(a). Therefore, TOFFEE for non-multiplying sources will be less than or equal to zero

$$t_{n,\gamma} - t_p \leq 0. \tag{5.2}$$

In contrast, for multiplying sources the measured time difference between correlated gamma rays and neutrons will include the difference in generation time, ΔT_g, as shown in Figures 5.1 (b) and (c). As a result, TOFFEE for sources with fission chains will be less than or equal to the times

between fission events that emitted each particle

$$t_{n,\gamma} - t_p \leq \Delta T_g. \tag{5.3}$$

There are three important implications from Eqs. 5.2 and 5.3 on the relationship between TOFFEE and the type of source measured. First, there is a sharp distinction between non-multiplying and multiplying sources because the former should have a steep drop in counts on the positive side of the TOFFEE distribution. The TOFFEE distribution of a multiplying source will, in contrast, be "smeared" in both negative and positive time directions by ΔT_g. The bi-directional smearing is exemplified in Figures 5.1 (b) and (c), and is the consequence of correlating gamma-neutron pairs where either the gamma ray or the neutron were born first.

Second, the TOFFEE distribution is sensitive to the level of neutron multiplication, M, in fissile material, given in Eq. 2.9. Neutron multiplication is defined as the average number of neutrons produced per starting neutron or the average length of a fission chain [16]. The probability of detecting particles from the same fission grows linearly with M, which will be distributed according to Eq. 5.2. Whereas, the probability of detecting particles from different fissions in a chain increases factorially with M and will be distributed according to Eq. 5.3. The contributions of the particles correlated in the same generation and different generation from a simulation of the bare BeRP ball is shown in Figure 5.2. In this example, generations are used to distinguish correlated events, because MCNPX-PoliMi output provides the generation number of a fission that originated a detected particle, but not a unique identifier of the fission event itself. Multiple fissions can belong to the same generation, because of branching in a fission chain, therefore this example is an approximation to TOFFEE distributions from same and different fissions. As a consequence, the same generation TOFFEE distribution, shown in Figure 5.2, will sometimes include the time between fissions of the same generation and will therefore also include a ΔT_g smearing term. The different generation TOFFEE distribution is not only smeared out due to the addition ΔT_g, but also has noticeably more counts due to the greater probability of detecting particles that are correlated

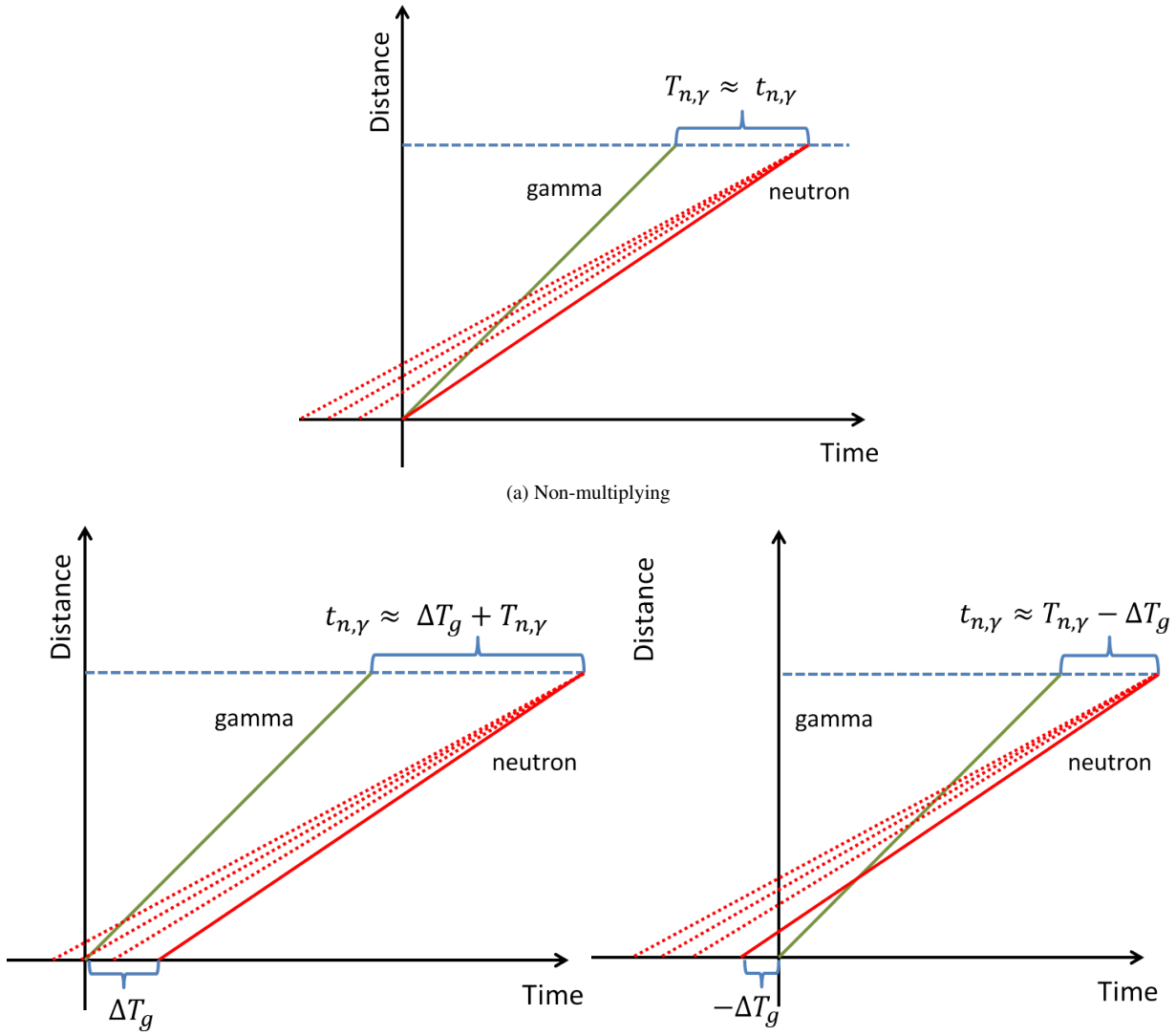

(a) Non-multiplying

(b) Multiplying, gamma ray born first

(c) Multiplying, neutron born first

Figure 5.1: Space-time diagrams of gamma ray (green) and neutron (red) particle paths from birth to detection (dashed blue line). The (a) non-multiplying diagram depicts the simultaneous birth of particles, and the (b) and (c) multiplying diagrams depict a fission chain where each fission is separated by generation time ΔT_g. The measured time-of-flight difference, $t_{n,\gamma}$, is equivalent to the true time-of-flight difference $T_{n,\gamma}$ in the non-multiplying case, but it includes the generation time in the multiplying case. The dashed red lines depict possible estimates of the neutron's velocity from proton recoil. The end-points of those dashed lines on the time-axis at the assumed source distance make up the TOFFEE distribution.

from separate fission events.

Finally, the influence of ΔT_g, as shown in Eq. 5.3, means that the TOFFEE distribution is simultaneously a measure of the length of a fission chain and the timing distribution of fissions

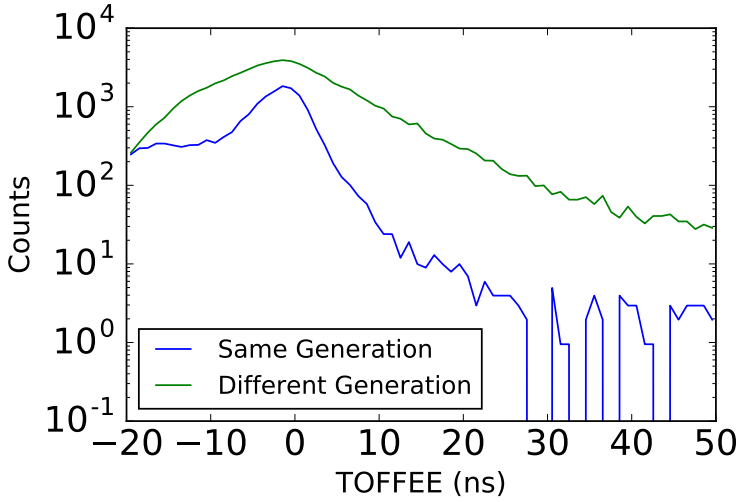

Figure 5.2: TOFFEE distributions of simulation of the BeRP ball constructed from gammas and neutrons originating from the same generation and different generations of fissions. There are more correlations from different generations due to neutron multiplication of the BeRP ball ($M = 4.389 \pm 0.005$).

within that chain. The characteristic time between fission events in a chain is indicative of the probability of fission, and the average neutron energy between fissions. In addition, for assemblies that are coupled to a reflector, the time between fission events also depends on the probability and delay time for a neutron to return to the fissile material.

5.3 Template Approach for Treaty Verification

Treaty verification is a process under which States party to a particular treaty validate each other's compliance through mutual monitoring. The objective of treaty verification is to establish trust and confidence that treaty obligations are not being violated. Any effective monitoring system should be sensitive enough to reliably verify compliance. However, for nuclear dismantlement and arms control treaties there is also the desire that sensitive information is not divulged through collected data [79]. Therefore, proper information barriers (IB) should be incorporated into measurement systems while maintaining the system's reliability. Templating is often presented as a methodology that offers a natural sequestration of sensitive information; all sensitive information used to confirm

an object is contained in a template which is protected by an information barrier [80].

Generally, a template based approach involves measuring a unique signature of a trusted object to build an identifying template. This measurement is then repeated on a tested object and the measured signature is compared against the previously acquired template in order to verify the object's identity [81]. A diagram of the procedure is shown in Figure 5.3. Because this technique relies on any deviation in measured signature, and not the absolute value of thereof, determination on object's authenticity can be made relatively quickly and with high confidence. Additionally, any potential sensitive information is carried with the template itself which naturally lends itself to application of information barriers; examples include zero-knowledge protocols [82, 83] and public-key cryptography [84].

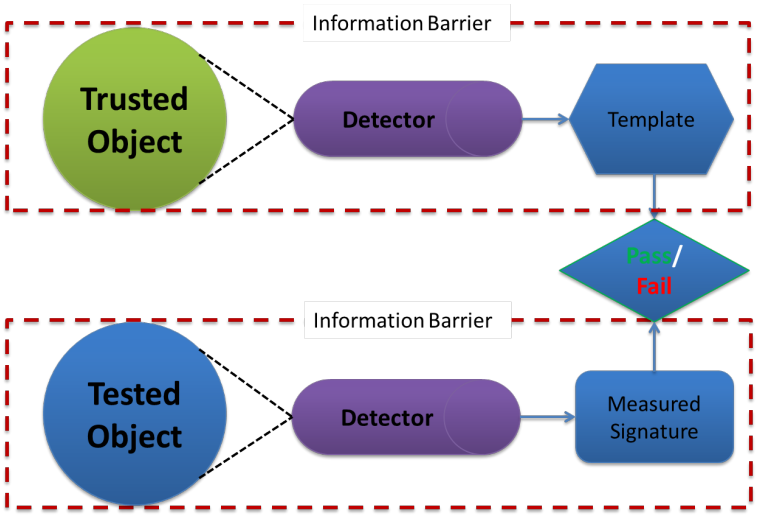

Figure 5.3: A diagram of the principle operations of template-based verification measurements.

The ability of the template based approach to impart confidence in the declaration rests in the uniqueness of the measured signature and trust in the authenticity of the measurement. This work does not deal with that latter requirement. The TOFFEE distribution measures the direct effects of the underlying fission chain timing distribution of a multiplying object, which is sensitive to any changes in fissile material mass, geometry and presence of surrounding neutronically coupled material. The sensitivity of the presence of a fission chain, and any perturbations in its timing distribution due to changes in its configuration makes TOFFEE distributions a useful signature for

item (warhead) confirmation and dismantlement confirmation. In general, these activities aim to answer the following questions:

- Dismantlement confirmation: Has the high explosive been separated from the fissile material?
- Item (warhead) confirmation: Is the fissile assembly including reflecting material in the tested object consistent with a nuclear warhead?

In the following sections the two propositions will be tested on surrogate fissile materials.

5.4 Experimental Setup

Dismantlement confirmation was tested by comparing bare and moderated configurations of WGPu BeRP ball [77] and of HEU Training Assembly for Criticality Safety (TACS) shells [85]. The moderated configurations used a surrogate material to simulate the presence of high explosive. The moderated BeRP ball configuration was surrounded with 2.54 cm thick shells of HDPE. In contrast, the TACS shells configuration is more complex with nested layers of Lucite, HEU and depleted uranium (DU) moving from the inside to outside. The inner radius of the Lucite was 4.6 cm, and the outside radius 7.92 cm at the edge of the DU. The inner most Lucite was left there from previous experiments in which the Am-Li source was placed at the center of the assembly. The moderated TACS configuration included an additional outer shell of 1.12 cm thick Lucite. Collectively the HEU shells weighed 16.53 kg compared to just 6.4 kg for the Depleted Uranium (DU). The presence of DU made confirmation measurement more difficult by attenuating all potential gammas emanating from U-235 fissions. In addition, HEU's lack of a strong source of spontaneous fissions necessitated actively interrogating the configuration with an Am-Li source. The interrogating source was placed on the opposite side of the TACS HEU shells with respect to the detectors.

Item confirmation was tested with a series of sources with increasing level of neutron multiplication: non-multiplying Cf-252, relatively low-multiplication 190 grams of WGPu Oxide

hemispheres (Hemis), and the relatively highly-multiplying BeRP ball. These were compared with the moderated BeRP ball and TACS shells. Except for the Hemis, which were measured at B262 at Lawrence Livermore National Laboratory (LLNL), all the other measurements were performed at the NNSS Device Assembly Facility (DAF). A summary of all the measured objects is provided in Table 5.1.

Table 5.1: Total data collection times for objects at the DAF and LLNL measurement campaigns.

configuration	distance (cm)	measurement time (min)	rate of gamma ray neutron pairs (Bq)	campaign
BeRP	34	59	55.6	DAF
BeRP + 1 in HDPE	34	589	77.8	DAF
TACS (HEU)	34	55	0.068	DAF
TACS (HEU) + 0.6 in Lucite	34	80	0.077	DAF
Cf-252	36	31	10	DAF
Hemi	46	499	0.096	LLNL

The measurement system consists of eight, 2âĂİ in diameter and 2âĂİ thick (2âĂİ×2") stilbene crystals arranged in a cylindrical pattern, as shown in Figure 5.4. Each stilbene crystal was coupled to H1949-50 Hamamatsu Photomultiplier Tube (PMT) with a custom low voltage to high voltage bias converter. Quarter inch thick pucks of lead were attached to the front of the detectors in order to minimize count rate from uncorrelated and low energy decay gamma rays emitted by the plutonium and americium in the BeRP ball. The PMT outputs were digitized by an 8 channel, 14-bit, 500 MS/s CAEN DT5730 desktop digitizer operated in asynchronous acquisition mode. Asynchronous acquisition allows each channel to record pulses above threshold independently, allowing for correlation analysis to be performed off-line with different coincidence windows. In synchronous or coincident acquisition, multiple channels have to trigger inside a certain time window for the events to be recorded. This second mode conveniently saves on the amount of acquired data, but the coincident window remains fixed to the acquisition settings used to collect the data. In this experiment, all pulses above the minimum threshold were recorded in list-mode and the gamma/neutron PSD and timing analysis was performed off-line. The PSD was performed using Bayesian procedure outlined in Section 3.5.

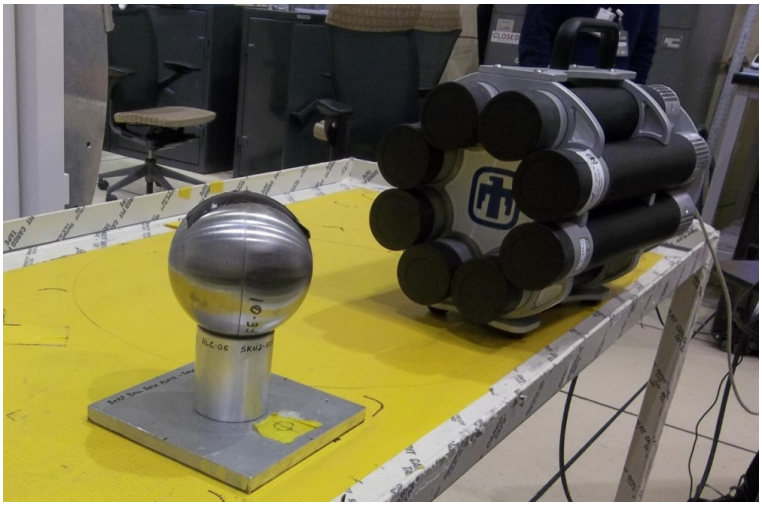

Figure 5.4: Photograph of the measurement of one of the BeRP ball configurations with the Stilbene Array.

5.5 Methodology

A log-likelihood was used as a metric to compare the template to other test object measurements. The counts in each bin of the TOFFEE distribution are assumed to follow Poisson statistics, and the template is used to get the expected mean for each bin. The metric value is then the sum of log-likelihoods for every bin:

$$L = \sum_{i=0}^{n} -\log(P(x_i|\mu_i)) \tag{5.4}$$

where n is the total number of bins and $P(x_i|\mu_i)$ is the Poisson probability of measuring bin value x given the scaled template bin value μ in the i$^{\text{th}}$ bin. The bin range of -5 to 60 nanoseconds was used to compare different measured distributions.

All correlated measurements will exhibit a âĂIJflatâĂİ background of uncorrelated random accidentals, the level of which is linearly dependent on the overall interaction rate. This rate will vary between different sources and configurations, ranging from 0.07 s^{-1} from TACS to 78 s^{-1} for the BeRP ball. The background rate was estimated by taking the average of the neutron pulse-height dependent rate of correlated counts in the -1500 ns to -500 ns window ahead of each gamma

ray. This average rate was then subtracted from the rest of the distribution for each measurement.

The rate of correlated neutrons and gamma rays varies between different sources and configurations. For example, the addition of a moderator provides some shielding while simultaneously increasing multiplication with the net effect of greater rate of measured correlated neutrons and gammas. The rate of correlated neutrons is sufficient to distinguish between almost all of our source configurations, as shown in Table 5.1, but this alone is not sensitive to the length of fission chain nor their temporal development. In contrast, the TOFFEE distribution, is uniquely sensitive to multiplication of the object itself. In order to separate the effects of correlated count rate and TOFFEE distribution shape, each test was conducted with both count normalized and time normalized TOFFEE distributions. In the time normalized analysis, the primary discriminator is the difference in rate. In count normalized analysis we remove these differences by using the same number of events from each distribution. This ensures that only differences in the shape of the timing distribution will enter the comparison metric. An example of both count normalized and time normalized TOFFEE distributions of the bare and moderated BeRP ball are shown in Figure 5.5.

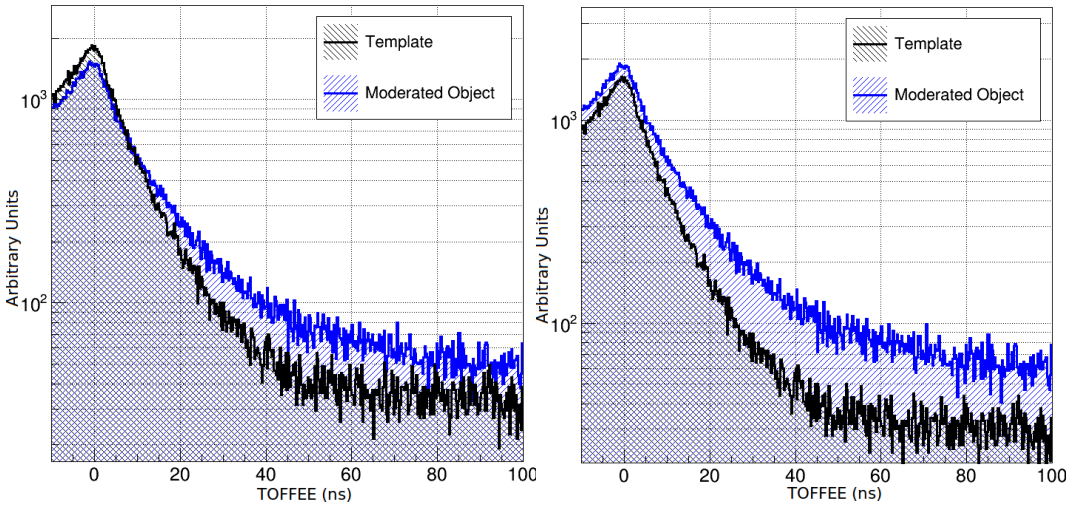

(a) Count Normalized

(b) Time Normalized

Figure 5.5: Count normalized (left) and time normalized (right) TOF corrected neutron-gamma time distributions for the bare BeRP ball (black) and the BeRP ball in a 2.54 cm HDPE shell (blue).

Verification performance was judged on the basis of minimum dwell times required to confirm dismantlement or a warhead. TOFFEE distributions of the tested object were constructed for specific dwell times by using a randomly sampled subset of measured data. A total of 10,000 trails of such randomly sampled subsets of data were used to estimate log-likelihood distributions for each dwell time, as is shown in Figure 5.6. An arbitrary operation point of 99% True Positive (TP) rate was chosen, and dwell times were incrementally increased until the False Positive (FP) fell just below 1%. The dwell times that met both these operational thresholds were recorded for comparison among different sets of trusted and tested objects.

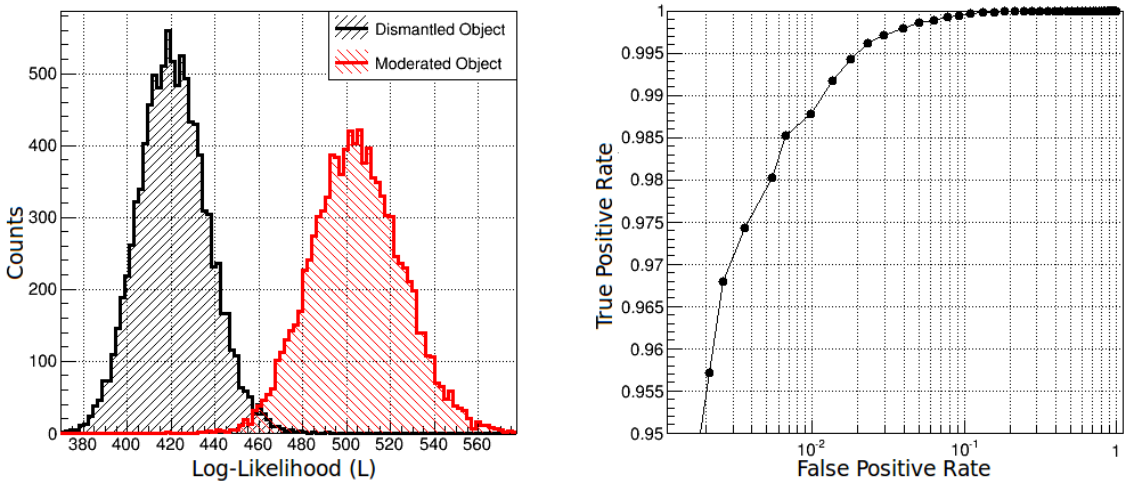

Figure 5.6: The log-likelihood distribution (left) and corresponding Receiver Operator Characteristic (ROC) curve (right) for 10,000 — 8 second trails of the comparison of the bare (dismantled) and moderated BeRP ball.

5.6 Dismantlement Confirmation

Dismantlement confirmation performance was tested by comparing bare and moderated configurations of the BeRP ball and TACS HEU shells. The bare configurations were used as templates and the moderated configurations were the test objects. A depiction of each trusted and test object pairs are shown in Figure 5.7.

The BeRP ball took only a few seconds to confirm, which was over an order of magnitude

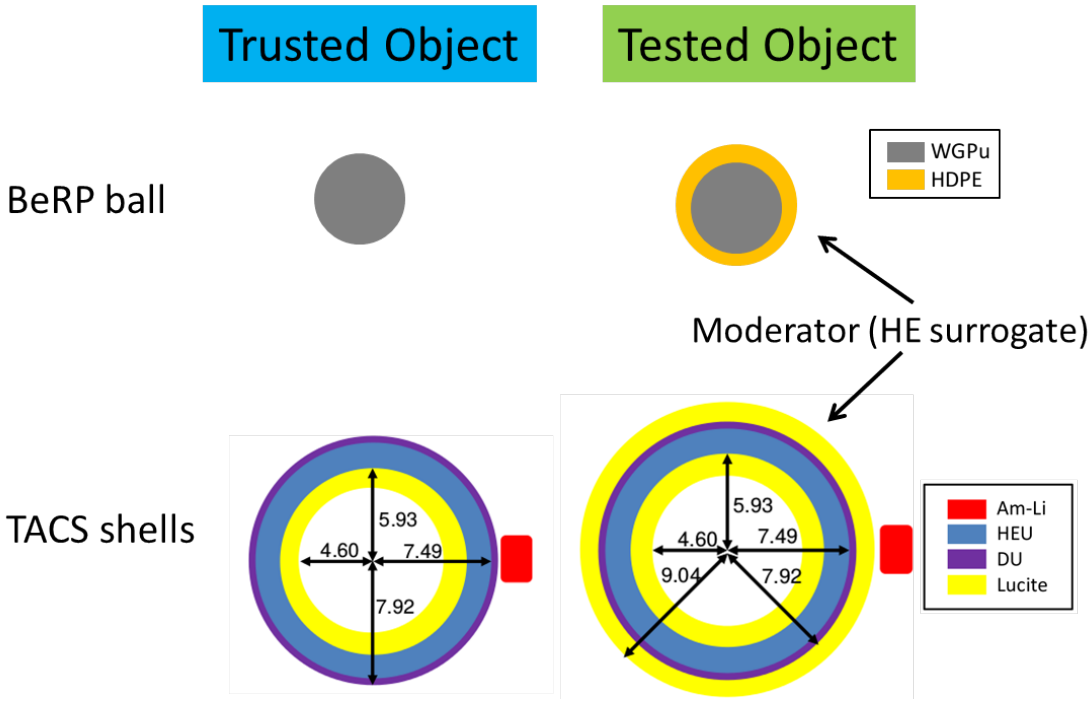

Figure 5.7: The pairs of trusted and tested objects used for dismantlement verification. The moderators, HDPE and Lucite, were used as high explosive (HE) surrogates. The inner and outer dimensions of the TACS shells are given in centimeters.

less time than the TACS shells. This difference is predictable due to the much higher spontaneous fission rate of Pu-240 in the BeRP ball which allows for much higher rate of fission chain initiation. Figure 5.8 illustrates the dependence of the False Positive rate for the two objects, assuming 99% True Positive rate operational threshold, on dwell time. In theory, it would be possible to reduce the dwell time required to confirm HEU by using a stronger interrogating source. The presence of DU shielding also effectively cuts down on the rate of measured correlated neutron and gamma-ray pairs.

Table 5.2: Summary of the time to confirm dismantlement with 99% TP and 1% FP rate.

trusted object	tested object	count normalized (s)	time normalized (s)
BeRP ball	BeRP ball + HDPE	12	3.7
TACS shells	TACS shells + Lucite	380	590

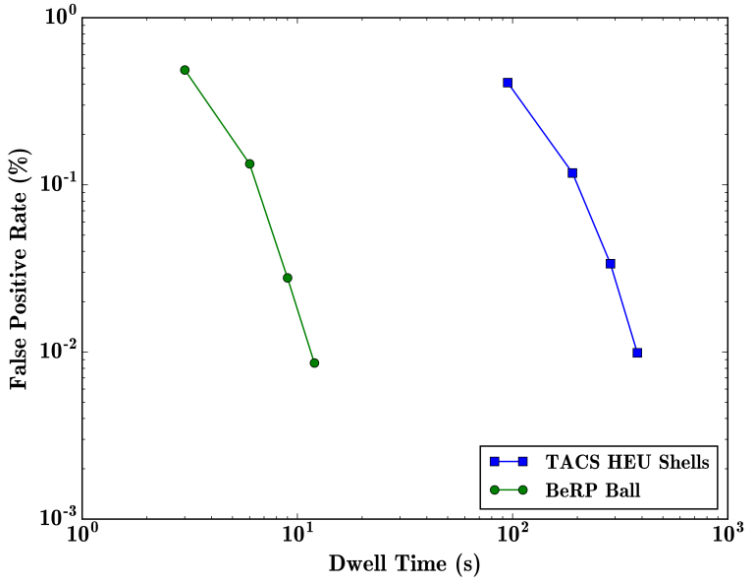

Figure 5.8: False Positive rate as a function of dwell time assuming 99% True Positive operational threshold with count normalized analysis of dismantled objects.

5.7 Item Confirmation

Item confirmation was performed by using the moderated configurations of the BeRP ball and TACS shells as trusted objects. A depiction of each trusted and test object pairs are shown in Figure 5.9. The choice of a test objects for item confirmation is much more difficult than in the case of dismantlement confirmation because of the open ended options for potential spoofs that an adversary could use. Two test objects were used: Cf-252 and plutonium oxide hemispheres (Hemis). The former is a readily available laboratory source of Watt spectrum fission neutrons, and the latter is fissile material with far smaller mass and Oxide chemical form.

As with the dismantlement confirmation, the requisite dwell times for confirmation against the BeRP ball are significantly shorter. The limited number of counts in the HEU measurement requires coarser binning in time and ultimately results in a much noisier template. The results are summarized in Table 5.3. The assumptions about Poisson statistics for calculating the log-likelihood also break down for any comparison that is statistically starved. Comparisons of False Positive rates as a function of dwell time for all cases are shown in Figure 5.10.

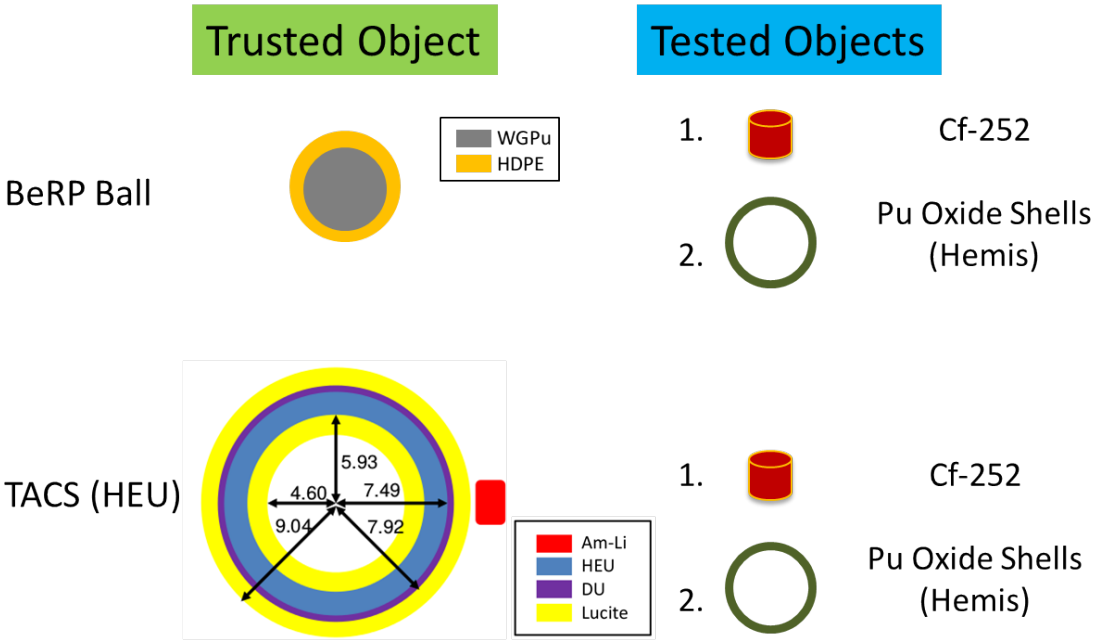

Figure 5.9: The pairs of trusted and tested objects used for dismantlement verification. The moderators, HDPE and Lucite, were used as high explosive (HE) surrogates. The inner and outer dimensions of the TACS shells are given in centimeters.

Table 5.3: Summary of the time to item confirmation with 99% TP and 1% FP rate.

trusted object	tested object	count normalized (s)	time normalized (s)
BeRP ball + HDPE	Cf-252	12	6
BeRP ball + HDPE	Hemi shells	2	6
TACS shells	Cf-252	1100	80
TACS shells	Hemi shells	540	960

5.8 Conclusions

The previously studied TCPH distribution, a bi-variate histogram of neutron deposition energy and time to correlated gamma ray, was collapsed into one dimensional TOFFEE distribution. As a result, the direct effect of the inter-generational time within a fission chain, ΔT_g, on the measured signature became apparent. Furthermore, TOFFEE was more desirable for direct comparison of measurements, because of the greater counts per bin, which improve statistical performance over the TCPH analysis. This capability was tested in the context of two treaty verification problems: dismantlement and item confirmation. The goal was to determine the minimum dwell time required

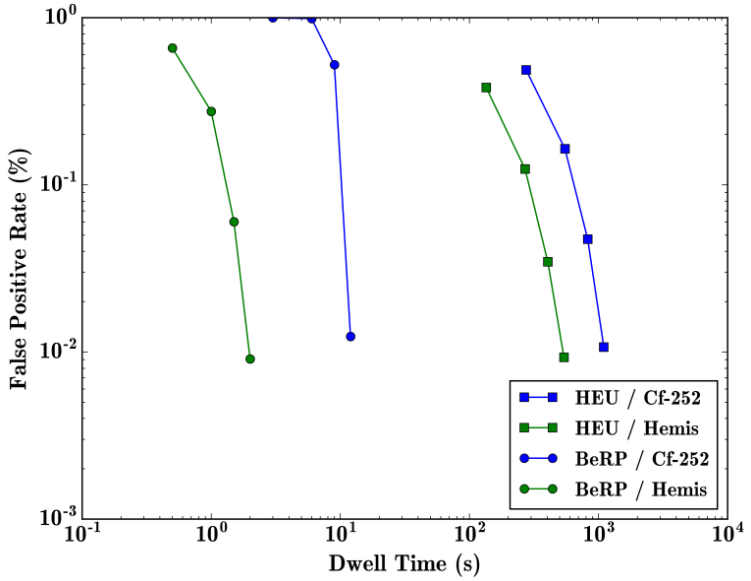

Figure 5.10: False Positive rate as a function of dwell time assuming 99% True Positive operational threshold with count normalized analysis for item confirmation comparing TACS shells (HEU) and the BeRP ball against the non-multiplying Cf-252 and low-multiplying Hemi shells.

to confirm that the test object did not match the trusted object, and to demonstrate that TOFFEE is a useful signature for these applications.

A TOFFEE distribution template of a trusted object was compared against test object's TOFFEE distribution with the log-likelihood as a metric of comparison. Distributions of the log-likelihoods were built by sampling 10,000 times from the measurements of the trusted and test objects for specific dwell times. These were then used to build Receiver Operator Characteristic (ROC) curves from which operational performance was determined. The desired performance threshold was set at 99% TP rate with a corresponding 1% or less FP rate, and the minimum dwell times required to achieve those performance thresholds were reported.

For both dismantlement and item confirmation, the BeRP ball required only several seconds (2-12 s) to determine that the test object was inauthentic. By contrast, TACS shells required hundreds of seconds of dwell time for confirmation at the same operational thresholds. The difference was mainly due to the relatively strong source of spontaneous fission neutrons from Pu-240 inside the BeRP ball, which drove the initiation of fission chains and corresponding correlated particles. The TACS shells, whose fissile component was HEU, had to be stimulated by an external Am-Li

interrogation source. In addition, the outer DU shell around the HEU further suppressed the signal from correlated neutrons and especially gammas.

Finally, the analysis was performed over both count normalized and time normalized TOFFEE distributions. It was expected that the additional difference in gamma-neutron correlation pair detection rates between trusted and tested objects would allow for faster confirmation and thus lower dwell times. However, the time normalized results were not consistently lower than the count normalized counterparts. In particular, the dismantlement confirmation with TACS shells and the item confirmation with the Hemi's produced the opposite of expected results. The measurement of those objects suffered from relatively lower gross counts due to equally low rates of detected gamma-neutron pairs. As a result, the reported dwell time may carry significant uncertainty, which was not reported in this work. However, this uncertainty is reflected by the difference in the count and time normalized dwell times which run counter to the expected results.

CHAPTER 6

Solving For Subcritical Assembly Physical Parameters

6.1 Motivation

In Chapter 5, the measured TOFFEE distribution was used to distinguish between different sources of correlated gamma rays and neutrons in the context of treaty verification. The reduction in the number of dimensions from the TCPH distribution made it more suitable for direct comparison of two measurements. In addition, the role of inter-fission timing in the shape of the TOFFEE distribution became clear. Inter-fission timing is influenced by both the amount of fissile material and presence of any reflectors. The sensitivity of the TOFFEE distribution to those factors was tested in Chapter 5. The work presented in this chapter will explore the extraction of physical parameters driving fission chain dynamics from the measurement of a TOFFEE distribution.

In a way this is a return to the analysis shown in Chapter 4, where empirical parameters of a Gamma function were shown to correlate with neutron multiplication and type of reflector material. However, the construction of an analytical TCPH distribution was rather convoluted and the empirical parameters of the Gamma function lacked immediate physical interpretation. This is avoided here by fitting the positive side of the simpler one dimensional TOFFEE distribution to a physically meaningful model that describes time dependent neutron population behavior in a critical assembly coupled to a neutron reflector. The physical model is developed from two-region point kinetics theory, which is an extension of the one-region point kinetics used in Rossi-alpha

method described in Section 2.2.1.

The goal is to determine three inter-dependent parameters:

1. Neutron multiplication
2. Amount of coupled neutron reflector material
3. The type of neutron reflector material

These are intrinsically difficult to decouple because greater amounts of neutron reflector increase neutron multiplication. The determination of the amount and composition of reflector material could be useful in the area of emergency response, or safeguards. Therefore, the analysis developed here could complement other traditional methods (e.g. multiplicity counting, Rossi-alpha analysis and gamma spectroscopy) that are complicated by the presence of neutronically coupled reflector material.

6.2 Two-Region Point Kinetics

As described in Section 5.2, the spread in the TOFFEE distribution of a multiplying source is driven by the generation time, ΔT_g, between the detected gamma-rays and neutrons. The probability of detecting these particles is governed by the time dependent population of fissions, or the corresponding neutrons that propagate fission chains. Point kinetics equations are a well established method for studying the time-dependent neutron populations in a nuclear reactor. However, modeling neutron behavior inside reflected assemblies required a two-region kinetic model [86, 87].

First, traditional reactor point kinetics is simplified by ignoring delayed neutron precursors that result from the cascade of decays of fission product isotopes. These fission product isotopes are typically organized into six groups with half-lives ranging from hundreds of milliseconds to tens of seconds [88]. These delayed neutrons can be ignored because the TOFFEE correlation window of interest is only on the order of a hundred nanoseconds. Ignoring delayed precursors, the time-dependent neutron population of prompt neutrons in a reflected assembly can be approximated

by:

$$\frac{dN_c}{dt} = \frac{k_c - 1}{l_c} N_c + f_{rc} \frac{N_r}{l_r} \tag{6.1}$$

$$\frac{dN_r}{dt} = f_{cr} \frac{N_c}{l_c} - \frac{N_r}{l_r} \tag{6.2}$$

where:

N_c is the number of neutrons in the fissile core region

N_r is the number of neutrons in the reflector

k_c is the multiplication factor in the fissile core region

l_c is the neutron lifetime in the fissile core region

l_r is the neutron lifetime in the reflector region

f_{cr} is the fraction of neutrons that leak from the fissile core region into the reflector

f_{rc} is the fraction of neutrons that leak from the reflector back into the core

Note that the k_c is different from the multiplication factor k, but the two are related as shown in Eq. 6.17. The former is the property of only the core, while the latter is the property of the whole *system* (i.e. the core and reflector assembly).

The system of equations in Eqs. 6.1 and 6.2 can be solved by converting them to a second order differential equation:

$$l_r l_c \frac{d^2 N_c}{dt^2} + (l_c - l_r(k_c - 1)) \frac{dN_c}{dt} - (f + k_c - 1) N_c = 0 \tag{6.3}$$

The new variable f is the fraction of neutrons that leak out of the core and are reflected back, which is just the product of two previously defined terms

$$f = f_{rc} f_{cr} \tag{6.4}$$

The complete solution requires two initial conditions:

$$N_c(0) = N_o \tag{6.5}$$

$$N_r(0) = 0 \tag{6.6}$$

at $t = 0$ the neutron population in the core is N_o and no neutrons are present in the reflector. The solution to Eq. 6.3, given these initial conditions is a familiar double exponential:

$$N_c(t) = N_o \left[(1 - R)e^{tr_1} + Re^{tr_2}\right] \tag{6.7}$$

where the roots to the characteristic polynomial are

$$r_1 = \frac{-\sqrt{4l_c l_r(f + k_c - 1) + (l_c - l_r(k_c - 1))^2} - l_c + l_r(k_c - 1)}{2l_c l_r} \tag{6.8}$$

$$r_2 = \frac{\sqrt{4l_c l_r(f + k_c - 1) + (l_c - l_r(k_c - 1))^2} - l_c + l_r(k_c - 1)}{2l_c l_r} \tag{6.9}$$

and scaling ratio R is

$$R = \frac{r_1 - \alpha}{r_1 - r_2} \tag{6.10}$$

where

$$\alpha = \frac{k_c - 1}{l_c} \tag{6.11}$$

f and k_c are constrained to be less than 1. The factor R falls within the range 0 to 1 for all plausible combinations of these variables.

The solution to Eq. 6.7 collapses to a single exponential shown in Eq. 2.13, which is a starting point for Rossi-alpha analysis, in three special cases:

1. The reflector does not return any neutrons, in effect the fissile material is bare.

2. Neutron lifetime in the reflector is large, and as a result neutrons crossing into the reflector just stay there.

3. Neutron lifetime in the reflector is exceedingly small, and as a result reflected neutrons are immediately returned to the fissile core.

In the first case none of the leaked neutrons are reflected back, that is $f_{rc} = 0$ and therefore $f = 0$. As a result, Eq. 6.1 simplifies to Eq. 2.12 and the solution is a single exponential.

The second and third case involve the extremes of the l_r parameter. If l_r is large, then the neutrons spend a long time in the reflector and do not return to the fissile core. Under that condition, and assuming a subcritical fissile core ($k_c < 1$), the roots of the characteristic polynomial are

$$\lim_{l_r \to \infty} r_1 = \alpha \tag{6.12}$$

$$\lim_{l_r \to \infty} r_2 = 0 \tag{6.13}$$

which implies that $R = 0$ and the solution in Eq. 6.7 again collapses to a single exponential characteristic of a bare assembly with the rate parameter α.

On the other hand if l_r is really small ($l_r < 0.01ns$) then the roots are

$$\lim_{l_r \to 0} r_1 = -\infty \tag{6.14}$$

$$\lim_{l_r \to 0} r_2 = \frac{f + k_c - 1}{l_c} \tag{6.15}$$

which in implies that $R = 1$ and again the solution collapses into a single exponential. The neutrons that enter the reflector either immediately disappear or are instantaneously return the fissile core. In this case the fraction f effectively adds to the probability that a neutron fissions in the core.

6.3 Experiments

The measurements were conducted at the NNSS, with five distinct reflector configurations shown in Table 6.1, at a source-to-detector distance of 30 cm. The reflectors were made from close fitting sets hemispherical shells made of iron and nickel, with a single 4.509 cm diameter hole used to support the fissile material at the center of the shells.

Table 6.1: Measurement details of the various configurations of the BeRP ball with iron and nickel reflectors. The neutron multiplication was calculated from MCNP5 k-code simulation.

case	measurement time (sec)	rate of gamma-ray neutron pairs (Bq)	multiplication
bare	1968	136	4.433 ± 0.001
0.5 in Fe	897	211	5.584 ± 0.008
1 in Fe	2095	280	6.648 ± 0.012
1.5 in Fe	1497	239	7.182 ± 0.015
1.0 in Ni	1497	243	7.472 ± 0.016

In addition to a multiplying source, a 21 μCi Cf-252 source was measured at a source to detector distance of 35 cm. This measurement was performed independently at Sandia National Laboratories. This measurement served as a starting point for validation of the MCNPX-PoliMi simulations that were used to extend the available measured configurations of the BeRP ball.

All measurements were performed with the same purpose-built portable array of eight 2" by 2" cylindrical stilbene crystals and acquisition system described in Section 5.4 and shown in Figure 6.1. The acquisition threshold was approximately 20 keVee (keV electron-equivalent), and the post-processing threshold was set to be 100 keVee.

The Birks' formula, from Eq. 3.6, was used for the neutron light output calculations with fitted parameters of $S = 1.63$ (MeVee/MeV) and $k = 27.83$ (mg/(cm^2 MeV)). The integrand in Eq. 3.6 was evaluated for deposited energies ranging from 1 keV to 250 MeV, and the results were saved in a lookup table. Linear interpolation of the values in the table was used to calculate light output from simulations and approximate proton recoil energy from light output in measurement.

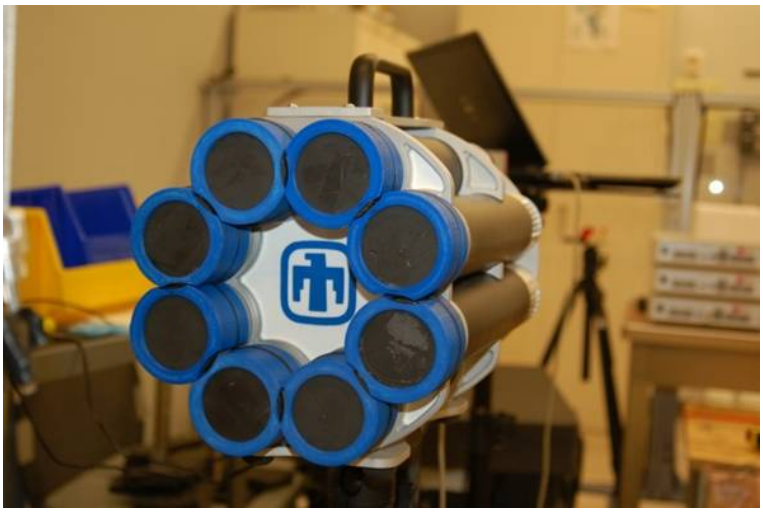

Figure 6.1: The front of purpose-built stilbene array used for all measurements.

6.4 Simulation Validations

The measured configurations of the BeRP ball, shown in Table 6.1, include three sets of shell thickness and two types of reflector material. Simulations were used to expand the range shell thicknesses, explore other reflector materials, and vary the mass of the BeRP ball by changing the diameter of the sphere. In order to have confidence in these results, it was necessary to validate the simulations by comparing them with measurements as will be done in the following sections.

6.4.1 Cf-252

The goal of starting with a Cf-252 source was to isolate contributions to the TOFFEE distribution caused by factors other than the development of a fission chain. One factor is the detector response, which depends on the energy calibration and validity of the light output function shown in Eq. 3.6. Another factor is particles scattering from other objects in the experimental setup, contributing to the so-called room return.

The ubiquitous Cf-252 isotope is a very well characterized source of correlated gamma rays and neutrons, and is readily available as built-in source option for MCNPX-Polimi [74]. In addition, the commercially available Cf-252 source capsule used for the measurement is small enough to

be approximated as point source in the simulation. The effects of room return were simulated by the addition of a 30 cm thick concrete floor 1 meter below the source. The floor is expected to dominate the scattering effects because of its proximity to the source, therefore the walls (2+ m away) and other smaller scattering materials were not included in the simulations.

The neutron Pulse Height Distributions (PHDs) were compared to test the energy calibration and neutron light output function. The neutrons were limited to those that were correlated with gamma rays inside a 2 μs window. The measured and simulated PHDs shown in Figure 6.2 overlap with the entire range of measured energies, without any noticeable systematic bias and within the statistical error. The statistical fluctuations are reflected in the relative error, which oscillates around zero.

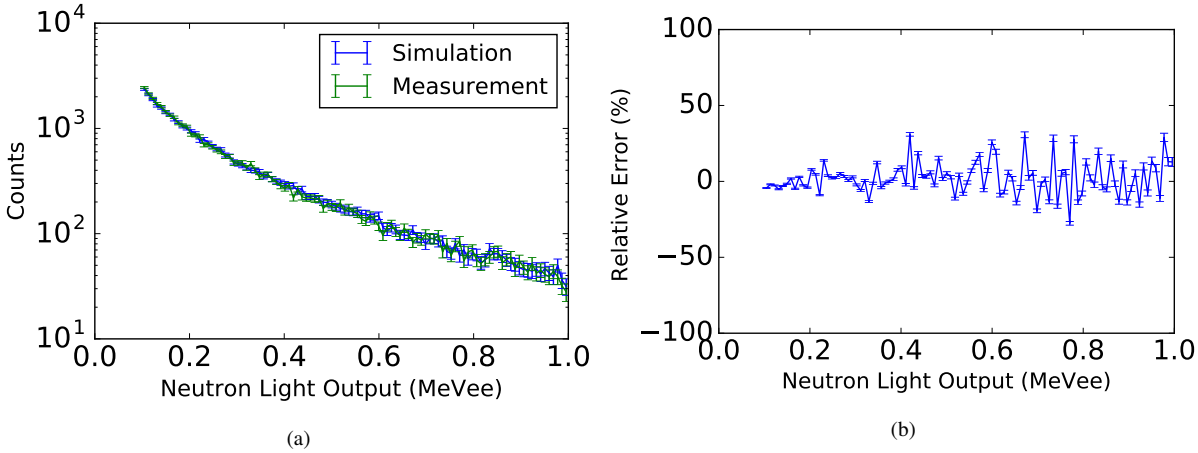

(a) (b)

Figure 6.2: Measurement and simulation comparison of the Cf-252 source (a) pulse height distribution of gamma-ray correlated neutrons and (b) corresponding relative error of the simulation.

In contrast to the PHDs, which is relatively featureless, the TOFFEE distributions shown in Figure 6.3 have several features whose shape depend on the detector response. The most significant feature is the bell-like curve between -10 and 5 ns which includes the vast majority of correlated counts. The width of these curves line up with each other, indicating that the energy calibration and corresponding thresholds are well matched, and that time resolution is properly applied. In addition, the width is affected by the source-to-detector distance, which in both the simulation and measurement was 35 cm.

The higher counts in the measurement in the region between -20 and -10 ns is partly due to PSD misclassification, where gamma-gamma correlations are mistakenly classified as gamma-neutron. There is also good agreement in the region beyond 60 ns, where the effects of scattering from the floor is evident. There are not many counts in that region, which contributes to the erratic relative error, but the simulation and measurement match within the statistical error. The region of the largest notable error lies roughly between 5 and 25 ns, right around the steep drop in counts expected from a non-multiplying source.

Finally, there is the rate of “accidental" correlations that depend on the source strength and appear as a flat background in the TOFFEE distribution. The contribution from accidentals is estimated by averaging counts in each bin of a region offset by 1000 to 1500 ns from each coincidence trigger. This is then subtracted from the TOFFEE distribution.

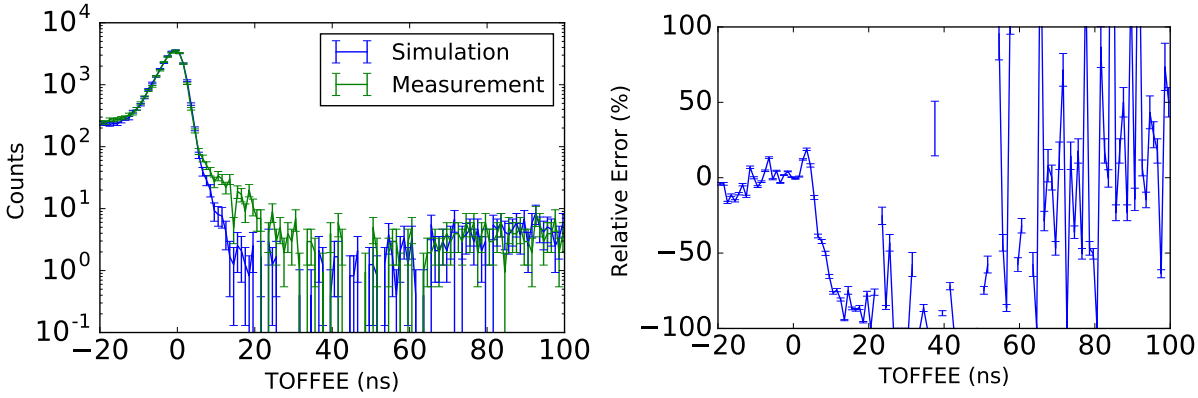

(a) (b)

Figure 6.3: Measurement and simulation comparison of the Cf-252 source (a) TOFFEE distribution and (b) corresponding relative error of the simulation.

6.4.2 BeRP Ball

The BeRP ball is a much more complicated source compared to Cf-252. It’s a distributed spherical source having a diameter of 7.59 cm and a multiplication of 4.4, and therefore cannot be treated as a non-multiplying point source. In the simulation, the source term was evenly distributed spontaneous fissions of Pu-240. In reality the BeRP ball includes a more complicated mix of isotopes

that become ingrown over time, but these were omitted from the simulation because they primarily contribute to the flat uncorrelated accidental background which was subtracted out.

The bare configuration comparison, shown in Figure 6.4, shows that the measured TOFFEE distribution is just slightly wider. The larger source of discrepancy is in the region between 40 and 100 ns, which is dominated by reflection from the floor. There are many time bins that are within statistical agreement in that region, but also a handful that have no counts at all. The problem is that the accidental background rate is much lower in the simulation (1 per ns) compared to the measurement (62 per ns) because of the lack of ingrown isotope sources in the former. In the measurement the higher accidental background competes with the effect of room return and is statistically significant when the two are subtracted, which is apparent from the large uncertainties.

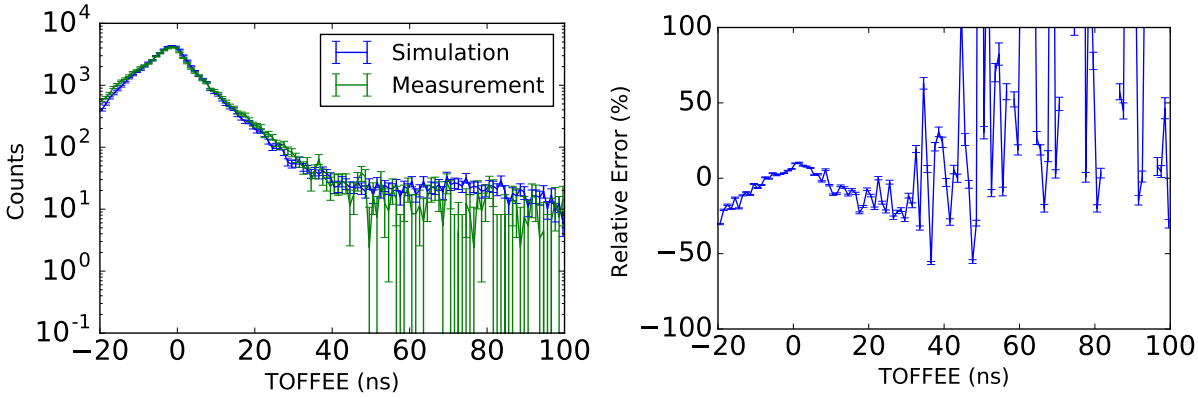

(a) (b)

Figure 6.4: Measurement and simulation comparison of the bare BeRP ball (a) TOFFEE distribution and (b) corresponding relative error of the simulation.

The overall agreement between simulated and measured TOFFEE distributions improves as reflector material is added. The BeRP ball with 1 inch iron is shown in Figure 6.5 as a representative example of the improvement. It appears that the time smearing associated with longer fission chains dominates over the discrepancies caused by room return, and accidental background.

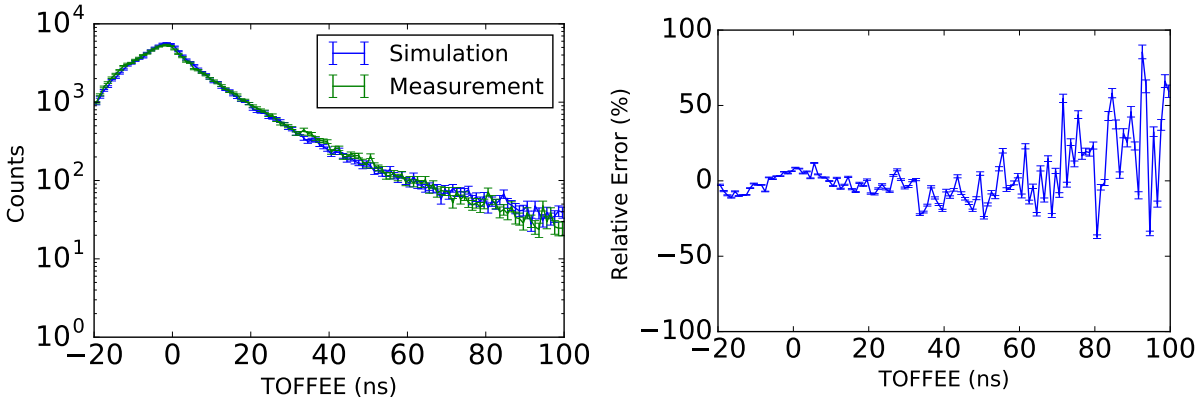

(a) (b)

Figure 6.5: Measurement and simulation comparison of the BeRP ball with 1 inch iron shielding (a) TOFFEE distribution and (b) corresponding relative error of the simulation.

6.5 Bare Configurations

Neutron multiplication and reflector thickness are correlated, since neutron reflection increases the neutron population and average length of fission chains. In order to study the effect of multiplication independently from the effects of reflector bare BeRP balls with various masses were simulated, ranging from 1 to 8 kg. The change in mass was accomplished by changing the diameter of the BeRP ball. A section of TOFFEE distribution, from 0 to 100 ns, were fitted to Eq. 2.13, which is a single exponential that doesn't account for a reflector.

A comparison of the measured and simulated BeRP ball is shown in Figure 6.6. As explained in Section 6.4.2, there is some disagreement at later times due to competing effects of floor reflection and accidental correlations. However, the fits and resulting α parameters for measurement (0.144 ± 0.003) and simulation (0.153 ± 0.004) are within two standard deviations of each other.

The multiplication factors and neutron lifetimes for the bare cases were tallied in MCNP6 simulations, and Eq. 6.11 was used to calculate corresponding α parameters. Figure 6.7 shows the comparison of these MCNP derived alpha values with the alpha values estimated from the exponential fits. The relationship between estimated and MCNP alphas is linear, and a regression analysis revealed a correlation coefficient greater than 0.98, and a slope of 1.0974.

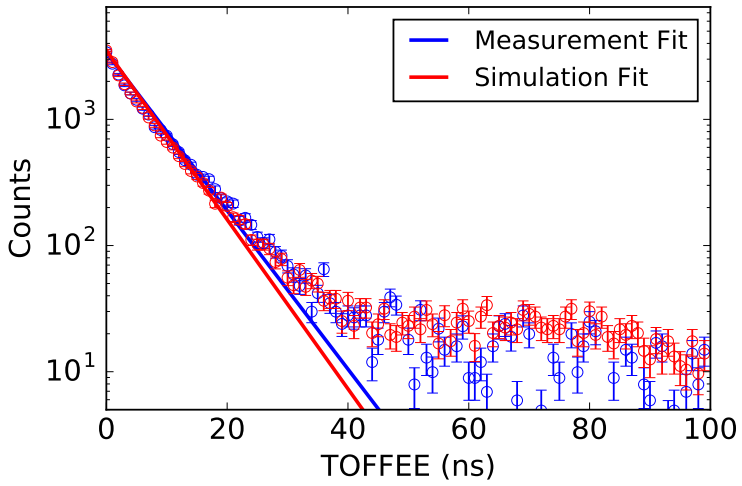

Figure 6.6: Comparison of the measured and simulated bare BeRP ball TOFFEE distributions and exponential fits from Eq. 2.13.

As shown in Figure 6.7, there is a slight deviation from the linear trend for the actual BeRP ball simulation and measurement. For all other masses the thin stainless steal shell surrounding the BeRP ball was removed and truly bare Pu spheres were simulated.

Neutron multiplication can be derived from the neutron decay constant and core lifetime by rearranging Eq. 6.11:

$$M = -\frac{1}{\alpha l_c}. \tag{6.16}$$

Neutron multiplications were derived from fitted alpha parameters by using previously tallied core neutron lifetimes from MCNP6. As expected, there is a positive linear correlation between the derived and actual neutron multiplication, as shown in Figure 6.8(a). However, the derived values underestimate the actual values, and the deviation grows with increasing BeRP ball mass. This increasing underestimation could be due in part to self-shielding, which would mean that detected particles are preferentially drawn from near the surface of the sphere. This is consequential because on average fission chains near the surface are shorter than the ones near the center.

Leakage multiplication, defined in Section 2.1.4, should compensate for the effect of self-shielding by taking into the account the probability of neutron leakage. The relationship between

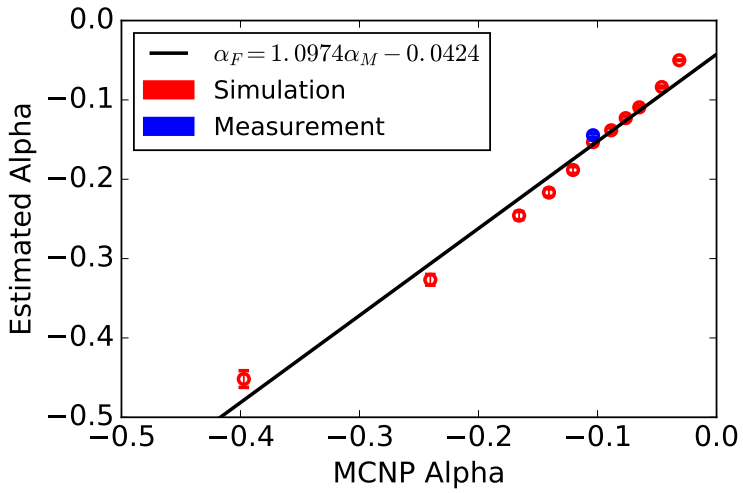

Figure 6.7: The estimated (α_F) and calculated, from MCNP6, (α_M) alpha parameters for BeRP balls with mass ranging from 1 to 8 kg. A linear regression was performed with the resulting relationship shown in the legend and a correlation coefficient of 0.9890.

derived multiplication and leakage multiplication is shown in Figure 6.8(b). There is still underestimation of the leakage multiplication with increasing BeRP ball mass, although it's less pronounced with average deviation of -10.69%.

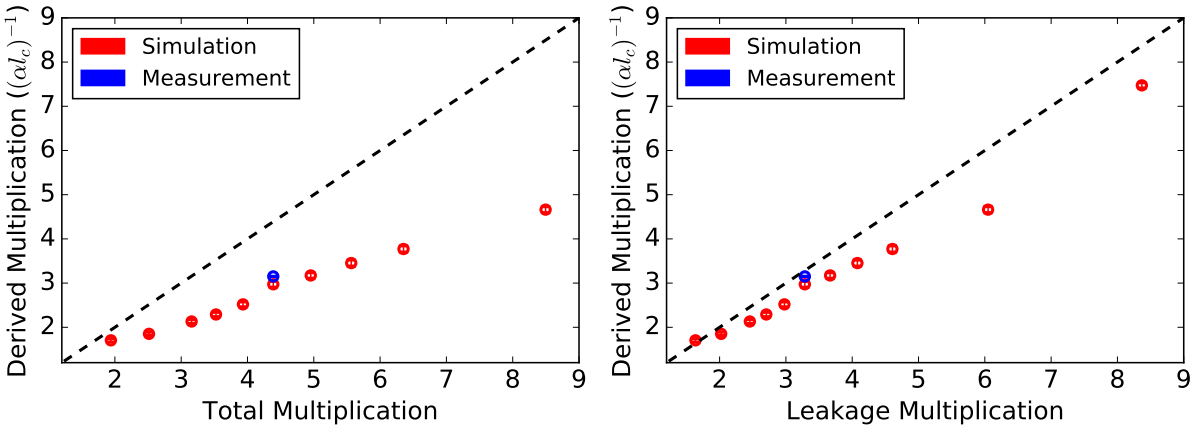

(a) (b)

Figure 6.8: Derived neutron multiplications from TOFFEE fits of the bare BeRP balls with different masses with the corresponding (a) total and (b) leakage multiplications obtained through MCNP6 simulations. The dashed line corresponds to perfect agreement between derived and actual multiplication, with the points above and below corresponding to overestimation and underestimation, respectively.

6.6 Reflected Configurations

Next we fit Eq. 6.7, derived from two-region point kinetics model in Section 6.2, to the reflected BeRP ball configurations. In Eq. 6.7 there is total of four physical parameters, but two of the parameters were constrained to make a meaningful fit.

At first three parameters were considered in the fitting routine: l_c, l_r and f. Either k_c or l_c have to be constrained because the correlation coefficient between the two is 1. However, the remaining two parameters, l_r and f, had no discernible trend between reflector material and across different shell thicknesses. Furthermore, the coefficient of correlation between the parameters was large, and corresponding uncertainties on the fitted parameters were large. A strategy had to be developed to systematically fit only two parameters.

Most meaningful results were obtained by fixing both k_c and l_c and letting l_r and f float. The core multiplication constant was taken from MCNP6 kcode calculation. The neutron lifetime in the core was then solved for separately for both simulations and measurements using Eq. 6.11 with the fitted α from the bare BeRP ball. The Eq. 6.7 fits of the measured iron cases are shown in Figure 6.9. In the first 60 ns time window the fit tracks quite well with the data, but undershoots the data at later times in the 80-100 ns window. Some of this behavior is due to the lower statistics in that region which make it less important for the fit. There is also some effect of floor reflection that is not accounted for in the two-region point kinetics model and therefore missing from Eq. 6.7.

6.6.1 Multiplication

The parameter f is related to the total system k by

$$k = \frac{k_c}{(1-f)}. \tag{6.17}$$

Neutron multiplication is then be calculated from Eq. 2.9. The comparison of this “Estimated Multiplication" with the MCNP6 equivalent for the measured and simulated cases is shown in Figure

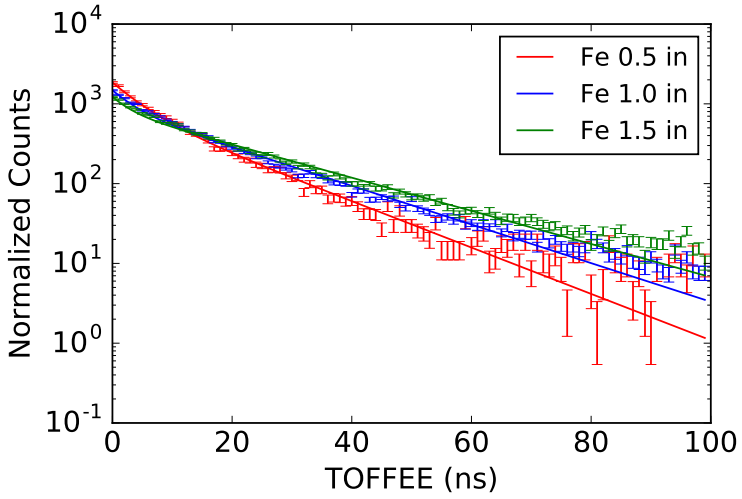

Figure 6.9: TOFFEE distributions of the measured iron configurations with corresponding double exponential fits from Eq. 6.7.

6.10. As expected, there is convergence between the simulated and measured cases with increasing shell thickness. The average relative difference between estimated and expected multiplication was 10%.

The simulation results that include aluminum and tungsten shells of up to 6 in thick are shown in Figure 6.11. The estimated multiplications for all shielding materials have positive correlations with the MCNP multiplication, although the relationship is different between materials. The trend is superlinear for aluminum and sublinear for tungsten. Iron and nickel have a more linear trend. The average relative difference also varied from one material type to the next, with as little at 14% for aluminum and as much at 22% for iron. Unlike with the bare case correlation with leakage multiplication produced even worse agreement and the trends among the different materials remained the same.

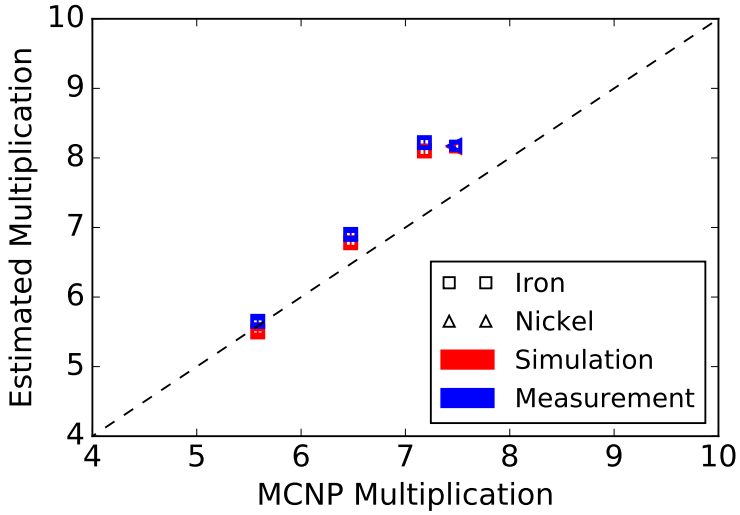

Figure 6.10: Comparison of the estimated multiplication of the measured and simulated TOFFEE distribution for the shielded configuration of the BeRP ball. The dashed line represent perfect agreement between the fit and the expectation from MCNP simulation.

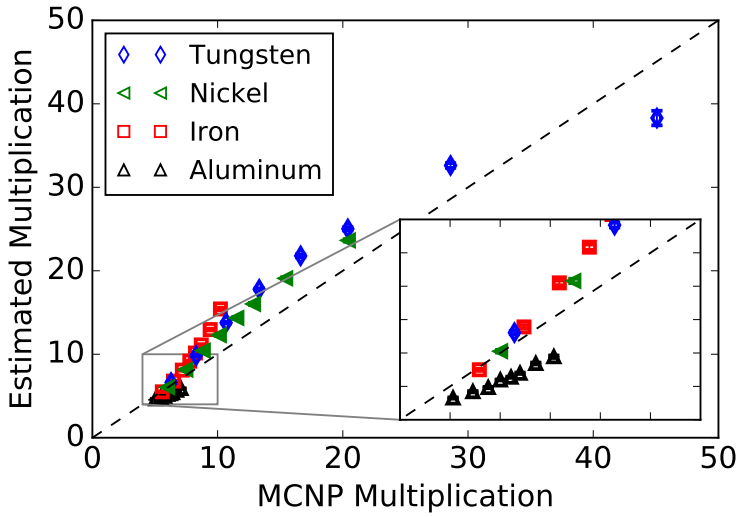

Figure 6.11: Estimated multiplication for simulated TOFFEE distributions of several configurations of shielded BeRP ball with different material types.

6.6.2 Shell Thickness and Material Type

Apart from the fitted parameters, f and l_r, there were a couple of derived quantities that proved to be correlated with physical quantities. The integral of Eq. 6.7 used in fitting the reflected configurations is

$$\int_0^\infty N_c(t)dt = \frac{R-1}{r_1} - \frac{R}{r_2} \tag{6.18}$$

Plotting this integral against shell thickness, as shown in Figure 6.12, reveals unique linear correlations for each material type. As mentioned before, shell thickness and multiplication are in themselves correlated, but the integral has much more linear and consistent correlations with shell thickness. Furthermore, the slope of each line increases with atomic number and density. This demonstrates that it may be possible to determine material type if shell thickness is known, or vice versa.

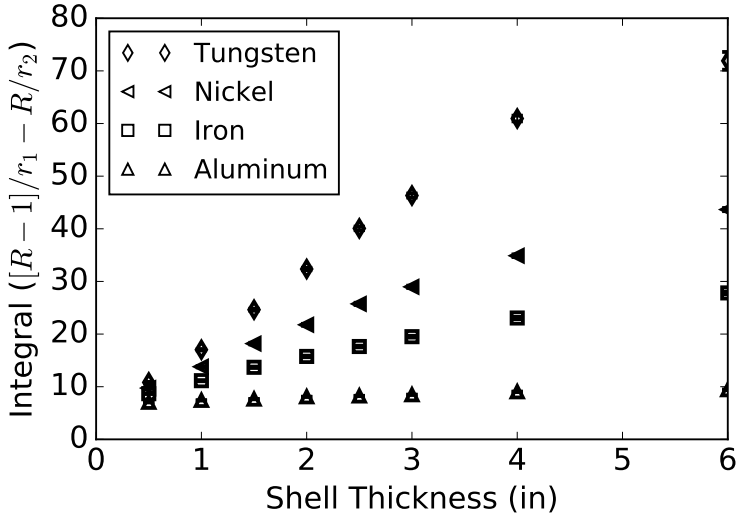

Figure 6.12: Integral of a double exponential fit as a function of shell thickness.

Given the relationships demonstrated in Figure 6.12, it was worth investigating the correlation with the integral of the fit could be decoupled from any particular element and related back to the total amount of reflector. The total amount of reflector surrounding the core was quantified by the effective areal density, which takes into account shell thickness and density. The integral

correlation with effective areal density for all four reflector materials is shown in Figure 6.13. The results of linear least-squares regression for each material and all of them combined is shown in Table 6.2. Each material has a unique linear correlation, but the combined regression shows a strong correlation coefficient of 0.9717. The deviation between materials is likely due to inelastic and other capture neutron interactions within each reflector, which is not correcting for.

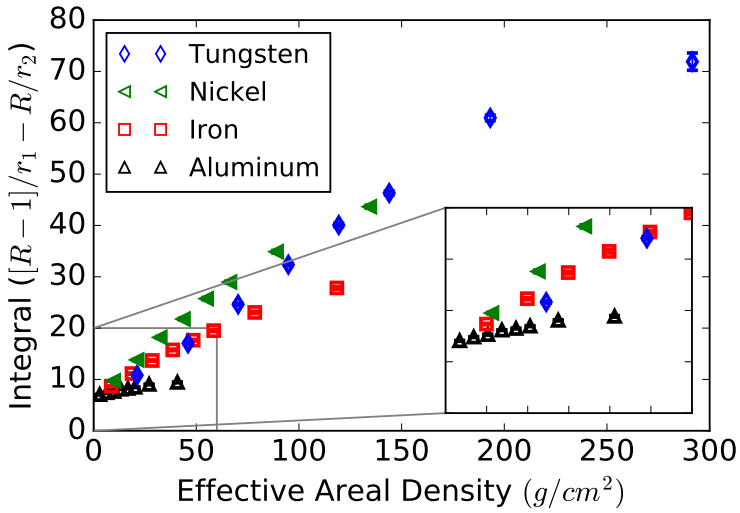

Figure 6.13: The integral of the fit of Eq. 6.7 to TOFFEE distributions of the reflected configurations of the BeRP ball and the effective areal density of each of the shells.

Table 6.2: Linear leas-squared regression for the correlation between integral of the fit to TOFFEE distribution and effective areal density of the reflector material.

reflector	slope	intercept	correlation coefficient
Aluminum	0.064	7.06	0.9748
Iron	0.175	8.46	0.9889
Nickel	0.274	9.10	0.9895
Tungsten	0.237	8.91	0.9815
All	0.251	6.55	0.9717

The second derived quantity of interest is the scaling ratio, R, which asymptotically approaches unity with increasing shell thickness, as shown in Figure 6.14(a). As the amount of reflector material goes up, so does its effect on the TOFFEE distribution. Eventually this dominant reflector term collapses the double exponential fit into a single exponential. This suggests that it may be

difficult to separate the effects fissile material mass and presence coupled reflector at sufficiently high areal densities of said reflector.

The asymptotic behavior of the scaling ratio approaching unity is driven by the fitted l_r that for the heavier materials approached zero, as shown in Figure 6.14(b). The results from fitted l_r mirror those of the scaling ratio shown in Figure 6.14(a), but unfortunately lack meaningful physical interpretation. Neutron lifetime in the reflector is expected to be largest for the denser materials, and increase with shell thickness. Instead, the exact opposite is shown to be the case. This may be a consequence of the negative covariance between f and l_r. As was shown in the multiplication analysis in Section 6.6.1, the parameter f appropriately increased with greater neutron multiplication. But this may have inadvertently driven the fitted value of l_r down because of its negative correlation.

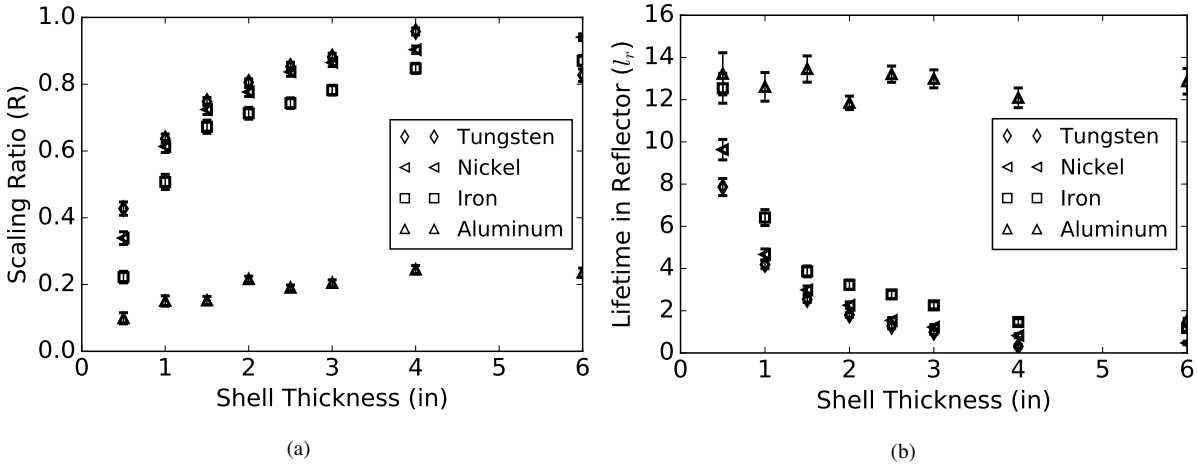

(a) (b)

Figure 6.14: The (a) scaling ratio and (b) neutron lifetime in the reflector from the fit of Eq. 6.7 to TOFFEE distributions of the BeRP ball with various reflector shell thicknesses.

6.7 Conclusions

The positive side of the TOFFEE distribution was fitted, from 0 to 100 ns, to time dependent neutron population derived from point kinetics theory. A bare subcritical assembly is sufficiently described by a single exponential in Eq. 2.13 and introduction of a reflector yields a double expo-

nential shown in Eq. 6.7.

For the bare cases the estimated alpha parameters and the expected alpha values are linearly correlated. A derived multiplication was calculated from the estimated alpha parameters by assuming a known l_c from MCNP6 simulations. This derived multiplication positively correlated with the leakage multiplication with an average relative error of 10.6%.

The TOFFEE distributions from the reflected BeRP ball assemblies were fitted to the double exponential model from Eq. 6.7. The derived multiplication from f had a positive correlation with the expected multiplication for MCNP6, although the relationship varied between material types. Furthermore, we determined that the effective areal density of the reflectors was positively and linearly correlated with the integral of those same double exponential fits. It is conceivable that with knowledge of either shell thickness or material composition it would be possible to determine the other property.

CHAPTER 7

3D Imaging

7.1 Motivation

Nominally this thesis is about measuring fission chain dynamics through gamma-neutron correlations. TOFFEE distributions provide an indirect means of measuring of the temporal evolution of a fission chain. The central approximation at the core of TOFFEE stems from the overestimation of the neutron travel time from proton recoil shown in Eq. 5.1. This is due to the fact that the proton recoil energy (E_p) underestimates the incident neutron energy (E_n):

$$E_p \leq E_n \tag{7.1}$$

which results in the inequalities in Eqs. 5.2 and 5.3.

If the incident neutron energy was known, then the measurement of the TOFFEE distribution would directly measure the generation time difference between correlated particles:

$$t_{n,\gamma} - t_p = \Delta T_g \tag{7.2}$$

As a consequence, the TOFFEE distributions from non-multiplying sources would resemble a delta function centered around zero, having a width due to timing and energy resolution of the detector system. This would potentially improve discrimination sensitivity between non-multiplying and multiplying sources, and improve characterization of the latter since ΔT_g would be measured

directly.

Neutron incident energy can be estimated with a double scatter neutron spectrometer, which, through detection of correlated gamma-neutron-neutron ($\gamma - n - n$) events, could yield this better resolved TOFFEE distribution. Fortunately, double scatter neutron imagers also function as neutron spectrometers, and those that can detect gamma rays have been in development for over a decade at both Sandia National Laboratories and University of Michigan [89]. A preliminary measurement of Cf-252 source with Mobile Imager of Neutrons for Emergency Response (MINER) [90], shown in Figure 7.1, revealed that estimated incident neutron energy rather than the proton recoil energy shifted the TOFFEE distribution around the origin, but did not appreciably narrow it. This is caused by the relatively poor energy and timing resolution of MINER, and therefore dominating the width of the TOFFEE distribution.

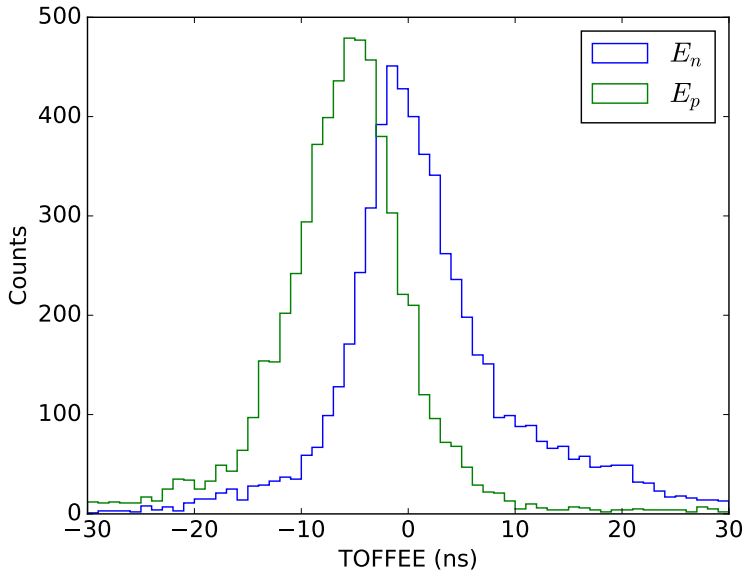

Figure 7.1: TOFFEE distributions of a measured Cf-252 source at a distance of 50 cm with neutron energy estimations using the proton recoil energy (E_p) and the incident neutron energy (E_n) from double scatter.

With this preliminary result, it is unclear if incident neutron energy information is worth the substantial diminished efficiency in detecting a triple coincidence of $\gamma - n - n$. Intuitively, the timing between gamma-neutron correlations carry with them information regarding the source-to-detector distance, a fact that was known from previous studies of the TCPH distributions discussed

in Chapter 4. In this Chapter, I rigorously prove the $\gamma - n - n$ coincidence provides the information required to reconstruct a correlated source in three dimensions. Some preliminary measurements and the proof of the method were first published in [91]. With this technique it is possible to perform 3D reconstructions of correlated gamma-neutron sources from a view from a single side, which is unique because traditional 3D imaging techniques require some movement of the detector around the source of interest or multiple detectors positioned around the object to be imaged.

This new imaging technique utilizes an inherent property of the majority of neutron sources important in nuclear threat-search, safeguards and non-proliferation: the coincident emission of neutrons and gamma rays. These sources include those undergoing spontaneous and induced fission [92], a property of SNM, and common (α,n) sources that leave the remaining nucleus in an excited state leading to prompt gamma ray emission [93].

7.2 Background of 2D and 3D Radiation Imaging

Radiation imaging is well established in fields as diverse as medicine [94, 95], astronomy [96, 97], and nuclear safeguards and non-proliferation [98, 99]. Because fission energy gamma rays and neutrons cannot be lensed as in optical imaging, they function by either:

1. modulating (blocking) the incident radiation

2. tracking multiple scatters of the incident particle in the detector medium, and estimating their incident direction by kinematic reconstruction of their paths.

The first gamma-ray camera was developed by Hal Anger who used multichannel collimators to modulate incident radiation [100]. The same principle can be applied with more complex coded aperture masks, which are analogous to superimposed pinhole cameras, to image both thermal and fast neutrons [101, 102].

The technique introduced in this chapter is an extension of the second category of radiation cameras which track multiple scatters to reconstruct source direction. In gamma-ray imaging,

these are called Compton cameras [98], and are a mature technology with commercially available portable cameras [103]. The functioning of a neutron scatter camera is analogous to the Compton camera, but with the use of the time-of-flight (TOF) between the first two scatters to determine the incident neutron energy rather than relying on full energy deposition in the second interaction [104].

The discussion so far has been limited to 2D imaging systems, but in principle any radiation camera can produce a 3D reconstruction of a source. The most common approach is to take multiple 2D images from different views, and combine them to form 3D rendering of the source. This technique is used in Single Photon Emission Computed Tomography (SPECT) and Positron Emission Tomography (PET) to image radioisotopes inside a patient [94]. Recently, researchers at Lawrence Berkeley National Laboratory have used a variation of this technique, combined with a 3D rendering of physical space, to reconstruct source locations in real time [105]. All of these techniques require multiple views of the source and some freedom of movement with respect to the object being imaged.

Single-sided 3D imaging has been demonstrated in Compton cameras by taking advantage of the parallax effect [106]. However, parallax techniques require a large solid angle coverage to function as a modality at all, whereas the $\gamma - n - n$ correlation method that I will describe only necessitates solid angle coverage to increase efficiency. Furthermore, the $\gamma - n - n$ technique could function at any distance with a portable system, even if it requires long measurement times.

7.3 Neutron Double Scatter 2D Imaging

Measurement of a double-scatter neutron provides a conical surface of possible source locations with the vertex at the first neutron scatter (n_0) and axis defined by the location of two scatters. In a traditional segmented scatter camera, each scatter is measured as a separate interaction within any two detector cells of the measurement system. Crucially, the incident neutron energy and by extension velocity of the incident neutron (v_n) is also calculated from this measurement [104].

The outgoing energy following the first neutron scatter is calculated by the time-of-flight ($\Delta t_{n_0,n_1}$) to the second scatter:

$$E_{n1} = \frac{m_n}{2}\left(\frac{d_n}{\Delta t_{n_0,n_1}}\right)^2 \tag{7.3}$$

where d_n is the distance between the two scatters. The outgoing energy is then summed with the energy lost due to proton recoil (E_p) in the first scatter which gives the initial incident energy of the neutron:

$$E_{n0} = E_p + E_{n1}. \tag{7.4}$$

The opening angle of the cone of possible source locations is

$$\cos^2(\theta_{n1}) = \frac{E_{n1}}{E_{n0}}. \tag{7.5}$$

The resulting cone of possible source locations is illustrated in Figure 7.2. Typically, a projection distance has to be chosen in order to display the image formed from the overlapping regions of the projected cones. The following section will show that by measuring a coincident gamma ray with a double scattered neutron it is possible to calculate the distance from the first neutron scatter to the possible source locations along the surface of the cone.

7.4 Gamma-Neutron-Neutron 3D Imaging

An illustration of the first neutron scatter (n_0) and the correlated gamma ray is shown in Figure 7.3. R_n and R_γ are the distances from a possible source location to the neutron and gamma ray interactions, respectively. Note that the second neutron scatter is omitted from this illustration, but it's shown in Figure 7.2. The goal is to solve for R_n in order to constrain the possible source location to the third dimension along the surface of the cone.

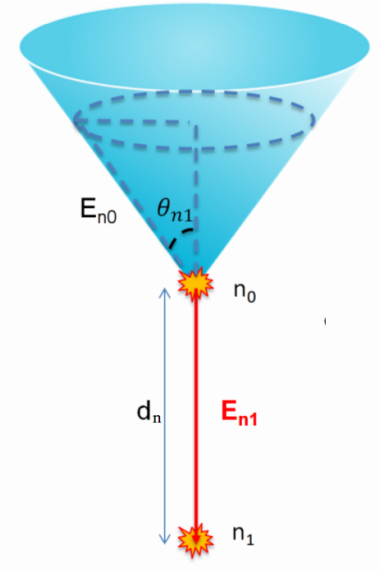

Figure 7.2: Illustration of the kinematics of a double neutron scatter in a scatter camera, resulting in a cone of possible source locations.

The two unknown distances R_n and R_γ, and the known distance d triangulate the location of the source along the azimuthal angle, ϕ, around the cone. These variables are related by the law of cosines in a parametric equation

$$R_\gamma^2 = R_n^2 + d^2 - 2R_n\mu d \tag{7.6}$$

where μ is the cosine of the angle between the cone surface and the vector $\overrightarrow{n\gamma}$

$$\mu = \frac{\overrightarrow{n\gamma}}{d} \cdot \hat{R}_n(\phi). \tag{7.7}$$

$\hat{R}_n$ is a unit vector pointing from the vertex of the cone to any possible source location along cone surface. The locations of γ and n_0 interactions, and therefore the distance (d) between them, are known implicitly from the detectors that participated in each interaction.

The measured time difference between γ and n_0 ($t_{\gamma,n}$) relates R_n and R_γ through

$$t_{\gamma,n} = \frac{R_n}{v_n} - \frac{R_\gamma}{c}. \tag{7.8}$$

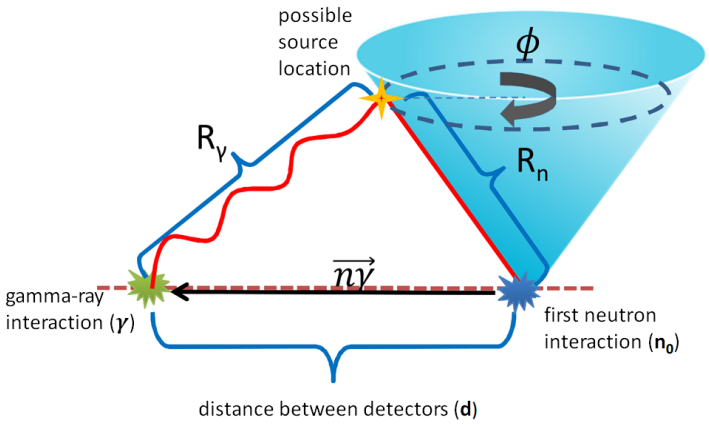

Figure 7.3: The cone of possible source locations from neutron double scatter and a corresponding correlated gamma ray. The second neutron scatter is not shown. The distances between the source (yellow 4-pointed star) and first neutron scatter (R_n) and gamma ray (R_γ) are shown for one of the possible locations along the surface of the cone. All other possible source locations lay somewhere along the azimuthal (ϕ) angle of the cone.

By substituting R_γ from Eq. 7.8 into Eq. 7.6, the resulting quadratic equation can be solved in terms of the distance from the first neutron interaction:

$$R_n(\phi) = \frac{c^2 t_{\gamma,n} v_n - d v_n^2 \mu \pm \sqrt{v_n^2 \left(c^2(t_{\gamma,n}^2 v_n^2 - 2 d v_n \mu t_{\gamma,n} + d^2) + v_n^2 d^2(\mu^2 - 1)\right)}}{c^2 - v_n^2} \tag{7.9}$$

Using these two solutions for image reconstruction is problematic, especially if the value of the discriminant is significant and dominates the resolution of the detection system. Fortunately, only one solution is physically possible, because the neutron cannot have a velocity exceeding c. The full proof of this is included in Appendix B. The valid solution is the one with the positive discriminant:

$$R_n(\phi) = \frac{c^2 t_{\gamma,n} v_n - d v_n^2 \mu + \sqrt{v_n^2 \left(c^2(t_{\gamma,n}^2 v_n^2 - 2 d v_n \mu t_{\gamma,n} + d^2) + v_n^2 d^2(\mu^2 - 1)\right)}}{c^2 - v_n^2} \tag{7.10}$$

The parametric solution to Eq. 7.10 effectively cuts a slice of possible source locations from the double neutron scatter cone from Figure 7.3. As a consequence, the distribution of possible source locations resembles “donut" in 3D space, as shown in Figure 7.4. This torus-like shape is

analogous to PET's line-of-response for a measured pair coincident gamma rays. Multiple such events further constrain the distribution of possible source locations by superposition of the torus-like shapes in 3D space. The region of overlap among those shapes reveals the true source location.

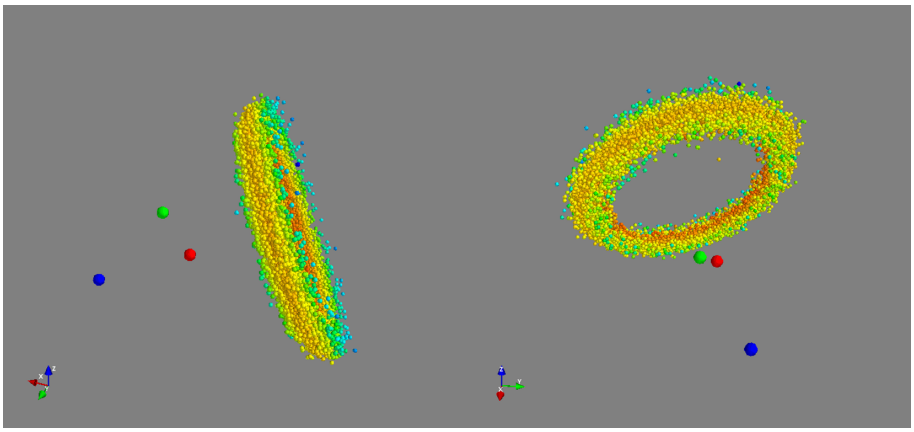

Figure 7.4: Possible source locations for a single measured correlated events shown as colored spheres. The first (red) and second (blue) neutron scatter define the central axis of the cone and the opening angle, and the correlated gamma ray (green) constrains the radial distance to form the resulting "donut" shape. The superposition of many donuts will reveal the source location in the overlapping region. For illustrative purposes we show the same object from two different angles.

7.5 Image Reconstruction

The solutions in Eqs. 7.5 and 7.10 provide the opening angle (θ) of the cone and distance from its vertex to possible source location (R_n), but additional steps are necessary to provide possible source locations. There are two ways to proceed with image reconstruction: the so-called list-mode or bin-mode [107]. In list-mode each possible source location is stored in an array, for example Cartesian (x, y, z) coordinates. In bin-mode the space of possible source locations is divided up into predefined bins of certain size and calculated source locations fill those bins. This distinction is only significant for the purpose of choosing an advanced reconstruction method like Maximum Log-likelihood Expectation Maximization (MLEM) or Stochastic Origin Ensemble (SOE). For this work, SOE was used to improve image quality, and it was intuitive to store all possible source locations in list-mode. The implementation of SOE is discussed in greater detail in Section 7.6.

In addition to calculating R_n and θ, it's also necessary to compute the unit vector between the first and second neutron scatter:

$$\hat{n} = \frac{\overrightarrow{n_1 n_0}}{d_n} \tag{7.11}$$

where d_n is the distance between two interactions. This vector will have to be declined by the opening angle of the cone, in any arbitrary direction. First, an axis has to be defined which points 90° away from $\hat{n}$ by taking the cross product between $\hat{n}$ and any arbitrary vector $\hat{u}$ and normalizing the result

$$\hat{n'} = \frac{\hat{u} \times \hat{n}}{|\hat{n'}|} \tag{7.12}$$

With this result, the original vector from the two neutron scatter points can be declined by the opening angle of the cone:

$$\hat{s} = \hat{n}\cos(\theta) + \sin(\theta)(\hat{n'} \times \hat{n}) \tag{7.13}$$

This source vector, $\hat{s}$, points to *one* of the possible source locations, but it's necessary to rotate it around the azimuthal angle of the cone, ϕ from Figure 7.3, in order to represent all possible source locations. The vector $\hat{s}$ can be rotated around axis $\hat{n}$ by angle ϕ through Rodrigues' rotation formula:

$$\hat{s}_{rot} = \hat{s}\cos(\phi) + (\hat{n} \times \hat{s})\sin(\phi) + \hat{n}(\hat{n} \cdot \hat{s})(1 - \cos(\phi)) \tag{7.14}$$

Once this vector is calculated, the source location can be determined by multiplying by the distance R_n.

The range of the azimuthal angle of the cone is constrained by

$$0^\circ < \phi < 360^\circ \tag{7.15}$$

but in reality there has to be a finite number of possible source points stored per set of correlated detected events. For this application, 100 points was sufficient for reconstructing a desired image. Any greater number of source points increased computational time without any tangible improvements in image quality. Each correlated set of events produced 100 points Cartesian coordinates of possible source locations, and the full list provided flexibility in how the final images were displayed. I went a step further, and applied SOE to improve image quality, as explained in the next section.

7.6 Stochastic Origin Ensemble

SOE is an application of the Metropolis-Hastings algorithm that is used to improve the reconstruction quality over standard back-projection. The new 3D imaging technique works just fine with back-projection, but advanced reconstruction techniques aid with the lack of adequate correlated counts. This is a particular problem for a technique that requires $\gamma - n - n$ particle coincidence. SOE was chosen because it is relatively straight forward to implement and it has been shown to improve the signal-to-noise and image quality in neutron imaging systems [108].

The basic idea behind SOE is to sample the measured quantities (time, interaction location, energy resolution) with appropriate uncertainties and estimate the source distribution as a probability density function (PDF). This is repeated for many iterations, as shown in Figure 7.5. The reconstructed source locations are displaced between iterations if certain criteria regarding new source location density is met. This displacement rate decreases rapidly over during the first set of iterations, referred to as the “burn-in" period. Once the rate of displaced locations has stabilized and adequate number of iterations is completed, the desired PDF is estimated as the density of source locations averaged over all iterations with uncertainties given by the variance of all interactions,

excluding the initial burn-in period. Details of the SOE algorithm as applied to Compton imagers is given in [109], and the principles are the same for neutron scatter cameras.

SOE can be computationally intensive, especially if the required number of iterations is large. Individual iterations may also require substantial computational time if there are many source locations, and if non-standard source density estimation is employed. Fortunately, SOE is in a class of Markov chain Monte Carlo (MCMC) methods which means that multiple iterations can be launched in parallel, and the final PDF can be determined from the average over all iterations. The source displacement over parallel iteration sessions is shown in Figure 7.5.

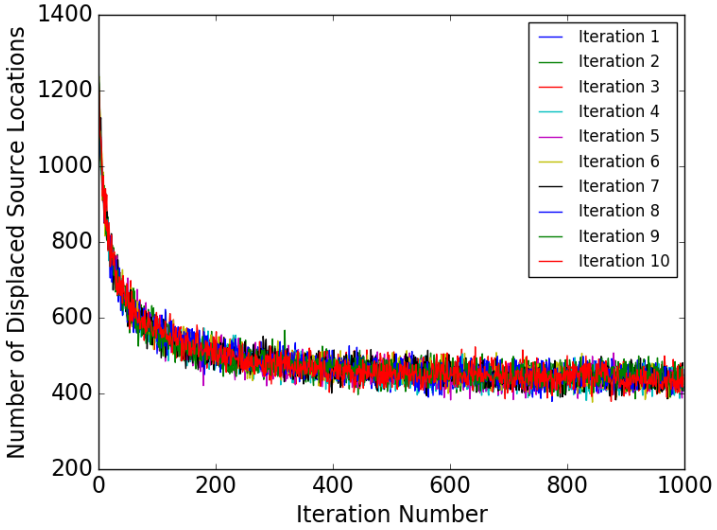

Figure 7.5: The number of displaced source locations per iteration during a SOE reconstruction of an image. This particular reconstruction was ran 10 times in parallel, as indicated by the legend.

The SOE method requires an accurate assessment of the source density between iterations. This task is made difficult with small number of correlated counts (a few thousand) in three-dimensional space. The simplest method of estimating density is by computing a multidimensional histogram. However, subdividing just 1 m^3 of space into 1 cc parts requires a million voxels, and given only a few thousand reconstructed source locations leaves the vast majority of the voxels empty or with only one count. Obviously, this makes for a dismal estimation of the source density at each location.

As a solution, a Kernel Density Estimator (KDE) was used to calculate the density at each source location. This method provides for an estimate of source density at every single point, regardless of how sparse the points are in space. A multidimensional KDE is defined as

$$\hat{f}(\boldsymbol{s}) = \frac{1}{n}\sum_{i=1}^{n} K(\boldsymbol{s} - \boldsymbol{s_i}) \tag{7.16}$$

where source locations are $s_i = (x_i, y_i, z_i)^T$ for a total of n. K is the kernel function, for this application the Epanechinkov kernel provided optimal results at reasonable CPU times. Besides the choice of an appropriate kernel, it's also necessary to select a bandwidth parameter, which acts as a sort of smoothing factor. The bandwidth parameter is analogous to the size of voxels or bins in the histogramming approach. If the bandwidth parameter is too large then the final image will appear blurry and smeared out. Otherwise, if its too small then the source density may be overestimated in certain areas leading to a distorted image. For this application, the bandwidth parameter closest to the resolution of the system (2-6 cm) appeared to work the best. The Scikit-learn machine learning package for Python was used to compute the requisite density estimations and multidimensional KDE computation [110].

7.7 Measurements and Simulations

As a proof of concept, a neutron scatter camera called MINER was used to conduct preliminary measurements [90]. MINER was adequate at proving the technique works, but it was primarily designed as a compact emergency response tool, rather than a high resolution system which would show the technique's full potential. Simulations of the MINER system with better, but currently achievable, timing and interaction location resolutions were conducted and the comparison between image resolutions are discussed in the following in this section.

7.7.1 Detection System and Setup

MINER is an array of sixteen 7.62×7.62 cm EJ-309 cylindrical detectors packaged in a larger cylindrical form-factor for portability and symmetry which allows for omnidirectional (4π) imaging. A photo of the opened system is shown in Figure 7.6. The portability comes at the expense of imaging resolution because adjacent cells centers are only 11.9 cm apart.

Figure 7.6: A photo of MINER in open configuration.

Two equal strength, 26.7 μCi, Cf-252 sources were measured 50 and 60 cm away from the center of MINER. The two sources were placed 45° apart as shown in Figure 7.7. The centers of each detector cell were taken as the position of the incident particle interaction. MINER has a timing resolution of approximately 2 ns and interaction location resolution of 2.2 cm.

The corresponding simulations assumed timing resolution of 200 ps and interaction location resolution of 5 mm. The former is possible with fast photomultiplier tubes (PMTs) or silicon photomultipliers (SiPMs) [111]. The latter can be achieved by using smaller detector cells, or using multiple readouts to better localize the interaction withing the detector. MCNPX-PoliMi was used to perform the requisite simulations [112].

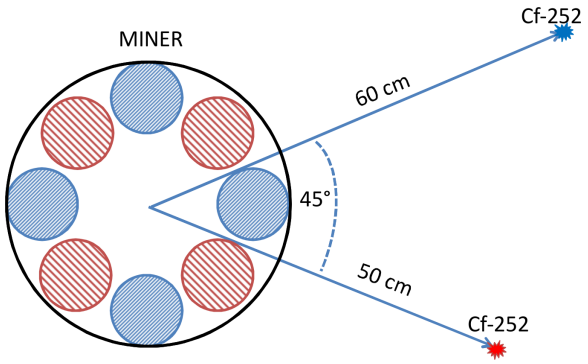

Figure 7.7: Measurement configuration showing the position of the two Cf-252 sources with respect to MINER. The dimensions of the detector and source-to-detector distances are drawn in correct proportions.

7.7.2 Point-source Image Results

Traditional 2D images of the measured and simulated Cf-252 sources are shown in Figure 7.8. Each source is marked by red (50 cm source) and blue (60 cm source) squares. The source points from those marked regions were used to estimate the radial distance and azimuthal angle resolutions. These resolution results are discussed in Section 7.7.3.

Figure 7.9 essentially displays a top-down view of the sources by looking at source particle densities projected on a polar plane. In all images and distributions shown each source point was weighted by r^4 in order to account for the efficiency of detecting two correlated particles.

In both measurement and simulation the two sources are clearly resolved in both radial distance and angular space. The 2D image from the measurement shows some reconstruction artifacts, likely caused by the application of SOE. These are largely due to the choice of a narrow bandwidth parameter, which improves resolution at the cost of having these artifacts in the final reconstruction. Nevertheless, the final image reconstruction of these point sources was not very sensitive to the selection of a bandwidth parameter from 2 to 10 cm.

7.7.3 Radial Distance and Angular Resolutions

It's clear from Figures 7.8 and 7.9 that the images improve with better detector system resolution parameters, but the images alone are not enough to quantify the improvement. For that purpose,

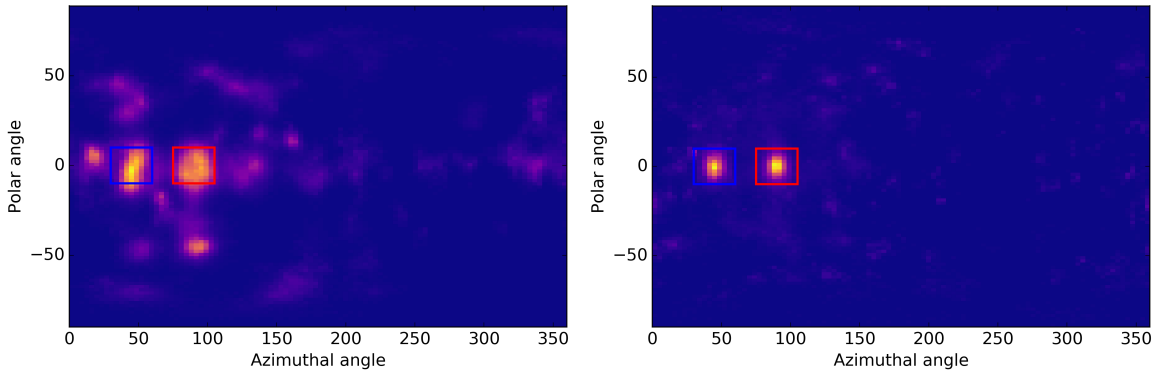

Figure 7.8: The measurement (*left*) and simulated (*right*) images with each reconstructed source point weighted by r^4. Each source is marked by a blue (60 cm source) and red (50 cm source) square.

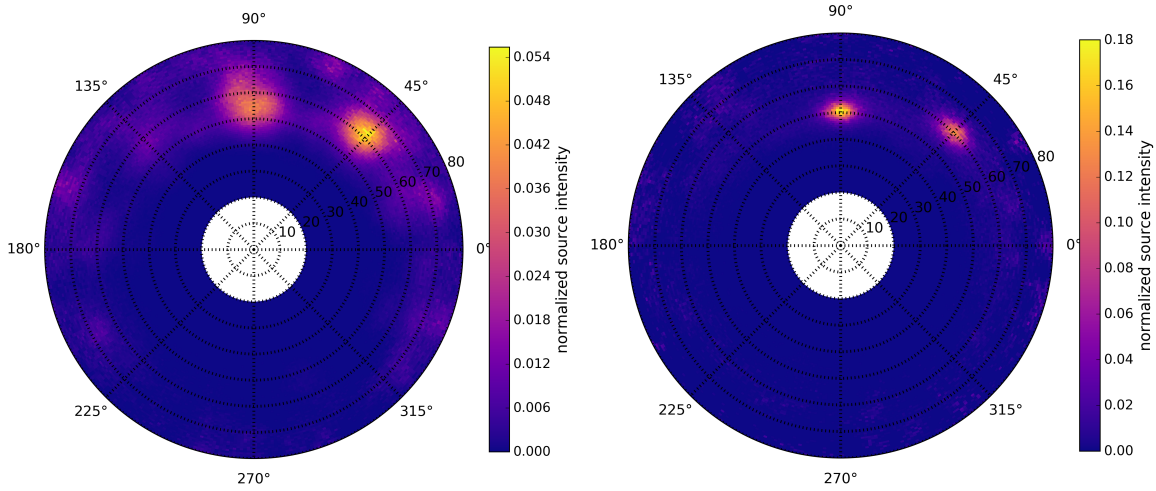

Figure 7.9: The polar projection (top-down view) of the image reconstruction for both the (*top*) measurement and (*bottom*) simulation.

the reconstructed source locations were projected along radial distance and azimuthal angle, and the results are shown in Figure 7.10. Peak locations and FWHM of the resulting 1D distributions were used to estimate accuracy and resolution, respectively. Both parameters were estimated by interpolating through the points in the distributions. The radial distribution and angular distribution parameters are shown in Tables 7.1 and 7.2.

The relative resolution of the radial distance is the ratio of FWHM and peak location, and it averaged at 26% for the measurement and 11% for the simulation. The angular resolution for the measurement improved from FWHM of 23° to 15° with source-to-detector distance. The simu-

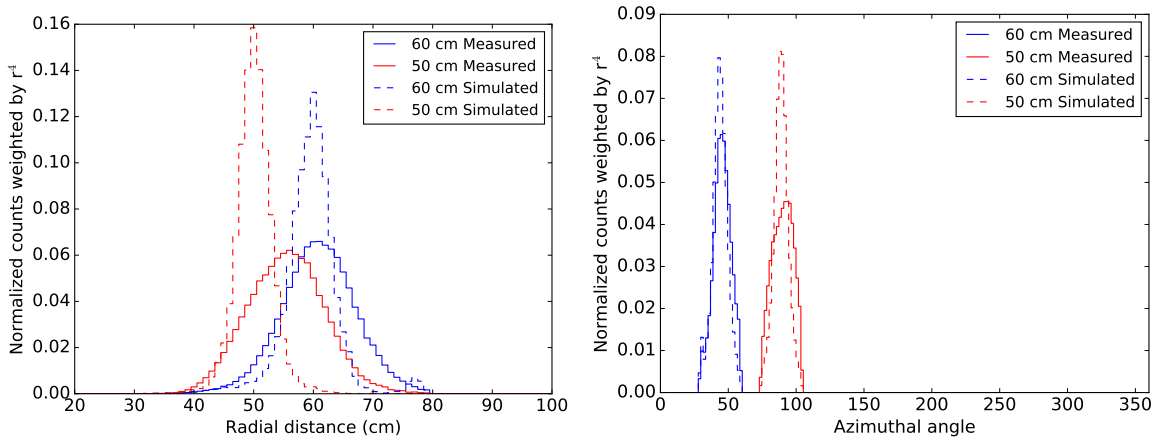

Figure 7.10: The radial distance (*left*) and azimuthal angle (*right*) distributions for both measurement (*solid*) and simulation (*dashed*). The radial distance distribution describes the distance from detector center. The source points were taken from the within the squares of the images in Figure 7.8, with matching color combinations.

lation results have an improved azimuthal FWHM of 11° for both sources. There is an apparent skewness of the radial distance distribution of the 60 cm source in the direction of the 50 cm source, which may contribute to the increase in absolute FWHM. This is due to some 50 cm source points present in the same angular region of the 60 cm source, which is due to the nearly double relative efficiency of detecting correlated signature from a source that is 20% closer.

The peak location for the measurement is off by 5.8 cm for the 50 cm source. If the source locations are not weighted by radial distance this discrepancy drops to 2.1 cm. By contrast the 60 cm source peak location is off by only 1.5 cm. This shift in peak location is not exhibited in the simulated system with better timing and interaction location resolution. This effect is caused by both the weighting of source locations and the presence of the 60 cm source. However, the weighting skewed the radial distribution of the 50 cm source toward the 60 cm source due to the significant overlap in the both radial distribution. By contrast the radial distributions of the simulated sources were well separated, as seen in Fig. 7.10, and the peak locations matched the true locations of the sources.

Table 7.1: Radial distribution (units in cm) parameters for each source in both measurement and simulation

	Source Distance	Peak Location	FWHM
Measurement	50	55.8	13.5
	60	61.5	15.1
Simulation	50	50.6	5.7
	60	60.3	6.8

Table 7.2: Azimuthal angular distribution parameters for each source in both measurement and simulation

	Angular Position	Peak Location	FWHM
Measurement	45°	47°	15°
	90°	91°	23°
Simulation	45°	45°	11°
	90°	90°	11°

7.7.4 Thunderbird Simulations

The results shown so far are of simulations and measurements of Cf-252 point sources. However, an extended source, one with actual physical dimensions, can better illustrate the utility and limitations of source reconstruction methods, such as SOE used in this work. For that purpose, I constructed a Cf-252 source in the shape of Sandia's thunderbird logo that was 27.5 cm wide, 25.5 cm long and 2 cm thick in MCNP. MINER was again used as a detection system, and with the same improved timing resolution of 200 ps and interaction location resolution of 5 mm. The MCNP model of both the source and detector system is shown in Figure 7.11.

The thunderbird source was laid flat from the point of view of the detector system. In a typical 2D image, this source would appear as essentially a line source, or a thin rectangle. But the advantage of the 3D imaging reconstruction, is that the depth of the source can be revealed. Furthermore, a top-down view of the source can be provided, just as it was with the polar projections in Figure 7.9, which would show the true nature of the source.

The image reconstruction of the thunderbird was performed in three ways: standard back-

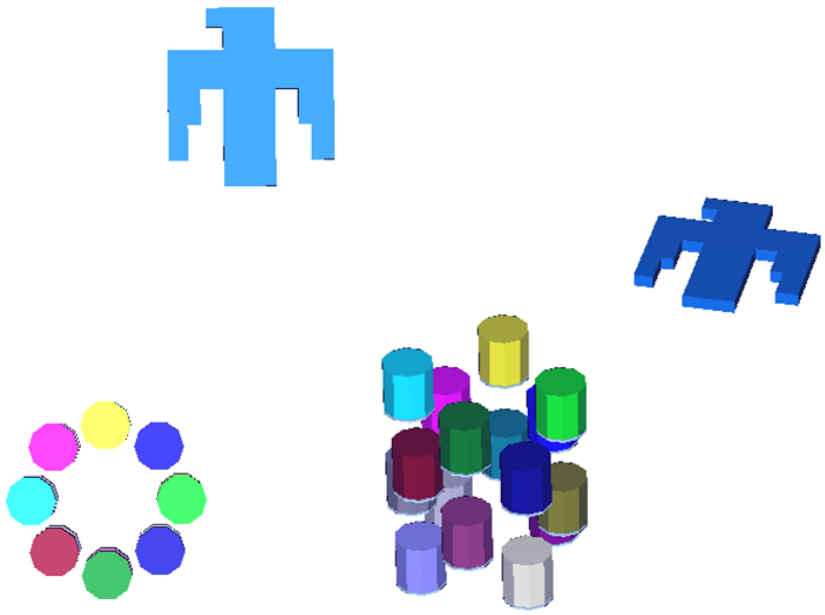

Figure 7.11: The top-view (*left*) and angled side view (*right*) of the MCNP model of MINER detector cells and thunderbird shaped Cf-252 source.

projection, SOE with 2 cm bandwidth parameter, and SOE with 4 cm bandwidth parameter. All three results are shown in Figure 7.12. In the back-projected image the thunderbird is visible, but through a cloud of non-source reconstructions. These are the result of throwing 100 source locations per correlated event, 99 of which will not correspond to the true source locations. The overlap of these points is more likely at the true source location, which is why the thunderbird shines through the image. The goal of SOE is to reduce the number of non-source reconstruction, and narrowing down on the correct ϕ for each correlated event.

However, as previously discussed in Section 7.6, SOE technique requires the choice of a bandwidth parameter, which acts as a width of the kernel used for the density calculation. This was not as consequential for point sources, but makes a noticeable difference in extended sources like the thunderbird. Thunderbird image reconstructions using both 2 cm and 4 cm bandwidth parameters are shown at the bottom of Figure 7.12. The 2 cm image is sharper, but has mis-reconstructed source points floating around it and the body of the thunderbird itself is breaking apart. These are the side effects of a bandwidth parameter that is getting to be too narrow. During the reconstruction process, source points become isolated islands, or hot-spots, which can make them

over-represented in certain areas of the image. With the wider 4 cm bandwidth parameter, these problems are largely mitigated, but at the cost of final image resolution. In fact, it would be difficult to discern that the original source was a thunderbird. Nevertheless, SOE is still a valuable tool in this case, since it increases the overall number of reconstructed source points at the true source location, and therefore improving signal-to-noise ratio.

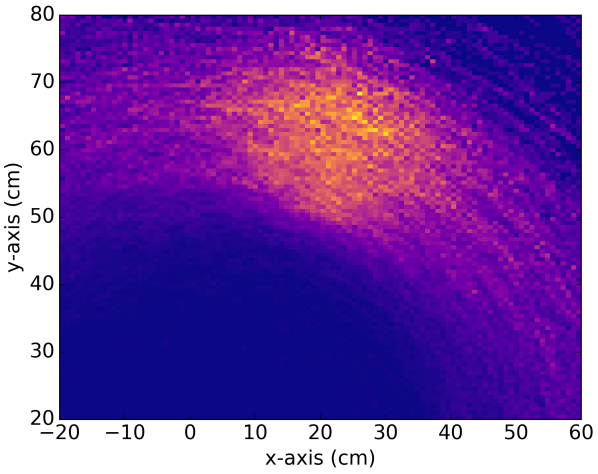

(a) back-projection

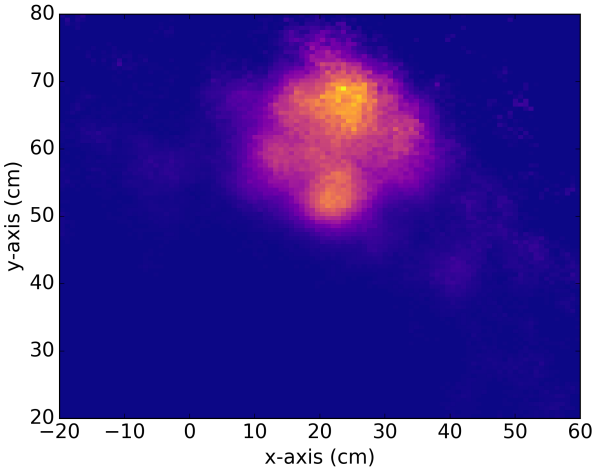

(b) SOE with 2 cm bandwidth

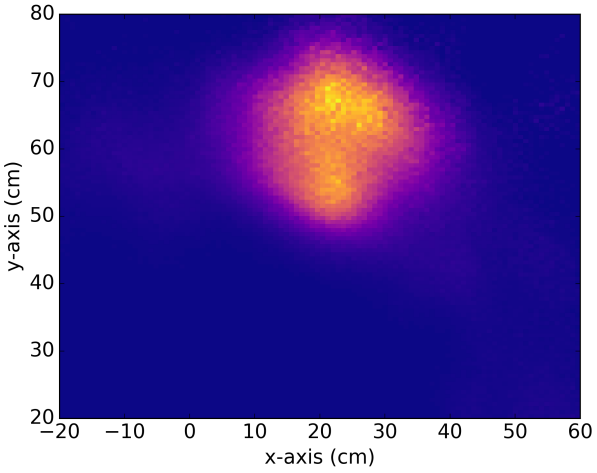

(c) SOE with 4 cm bandwidth

Figure 7.12: Image reconstructions of a thunderbird shaped Cf-252 source performed using (a) back-projection and SOE with (b) 2 cm and (c) 4 cm bandwidth parameters. The images are top-down view, with all source points between $-5 < z < 5$ projected onto an $x - y$ plane.

7.8 System Resolution and Uncertainty Analysis

System resolution is quantified here by the source-to-detector distance R and the opening angle of the projected cone θ. Apart from the interaction location, the remaining measured sources of uncertainties are $n-n$ and $\gamma-n$ timing and neutron pulse amplitude. The impact of all three can be visualized by assuming timing resolution of 2 ns and energy resolution of 10%, and then solving Eqs. 7.5 and 7.10. The result of this is shown in Figure 7.13. As expected, $\gamma-n$ timing only effects the radial distance, which makes sense because it's introduced into the equations specifically to solve for it. The remaining sources of uncertainty, neutron pulse amplitude, and $n-n$ timing, effect both quantities of interest although the sign of the correlation is different with each.

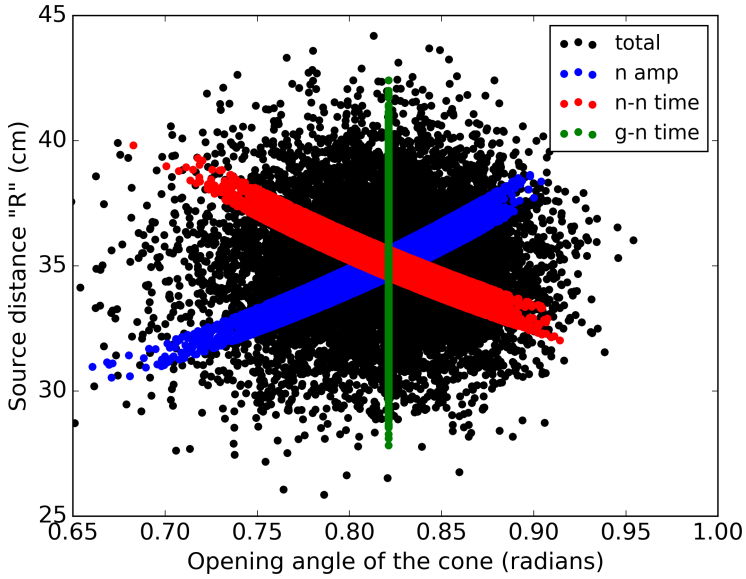

Figure 7.13: Visualization of the spread source-to-detector distance and the opening angle as a function (red) $n-n$ and (green) $\gamma-n$ timing, and (blue) neutron pulse amplitude uncertainty. Each source of uncertainty is treated separately, and the results are displayed in different colors, the combined result is shown in black. A timing resolution of 2 ns and energy resolution of 10% was assumed

Uncertainty quantification on R was performed using linear error propagation theory [113] which also included contribution from interaction location resolution. The overall timing resolution had over twice the error contribution compared with the interaction location resolution. The gamma ray timing was nearly six times more important than the neutron timing, which makes sense

given the relative speed of each particle. By contrast the neutron interaction location contributed nearly an order of magnitude more compared with the gamma ray interaction location. The first neutron interaction location had double the contribution of the second interaction.

In conclusion, the gamma ray timing resolution and neutron interaction location resolution are the primary contributors to uncertainty in radial source-to-detector distance. This was true for the measurement with timing resolution of 2 ns and interaction location resolution of 3 cm. At the simulated resolutions of 200 ps and 5 mm, the uncertainty in the proton recoil energy from the first neutron scatter (E_p) was the limiting factor. This includes the effects of energy resolution and calibration of the detector and measurement of light output response. The current practice involves fitting light output response to an empirical formula [54, 114]. Improvements could be made by better characterization of the detector response, but the estimation of the proton recoil energy would ultimately be limited by the low energy resolution of organic scintillators.

7.9 Augmented Reality

3D radiation imaging is a powerful tool, but it's difficult to display the results on a monitor display or a flat piece of paper. There are limits to what can be shown through the use of multiple projections, or views of the source, as used in Figures 7.8 and 7.9. Ideally, one would display the 3D reconstructed image of a source as a hologram, and preferably in the context of the real world surroundings of said source. Fortunately, this thesis is being written in 2017, the future is now, and the technology exists to accomplish just that.

Augmented Reality (AR) is a live display which allows a used to "augment" the real world elements through computer generated graphics, or other sensory inputs. This differs from virtual reality, where the entire sensory space is computer generated, and the user is unaware of their actual physical surroundings. Microsoft has developed AR capable headset called the HoloLens, which is pictured in Figure 7.14. The HoloLens is a head-mounted portable computer with smartglasses and variety of cameras, and other sensors. Smartglasses display either 3D holograms or 2D flat

projections that appear as part of the physical world. The cameras and sensors map out the physical surroundings and track movement of the user, which allows the visualizations to stay in place and interact with the real world. For example, a hologram of a coffee mug can be placed on top of a real table, and the mug will maintain its position as the user moves around the room.

Figure 7.14: Microsoft's HoloLens.

Fortunately for me, researchers at Sandia have already obtained a HoloLens for other unrelated work and had experience getting it to display holograms. I collaborated with them, providing them with the 3D reconstructed image data, with the goal of having the images displayed through the HoloLens. A demonstration of the technology and 3D radiation method was given during the 2016 Consortium for Verification Technology Workshop. The results of these efforts are difficult to show on paper in this dissertation, but an example of the aforementioned thunderbird source as seen through a HoloLens is shown in Figure 7.15. The thunderbird source hologram floats in space, and can be inspected from any angle that the user chooses to look at it.

The other useful feature of this technology is that it allows for display of holograms behind a physical barrier. For example, it is possible to render pipes that are installed inside a wall. This may be applicable to emergency response scenarios, where a source is hidden inside a figurative black box, and 3D imaging can provide the physical dimensions of the source without the need to open up the container. Another similar application in treaty verification may involve the imaging of pits that are stored inside drums. AR would allow an inspector to walk around the drum and visualize the object inside without the need to open anything.

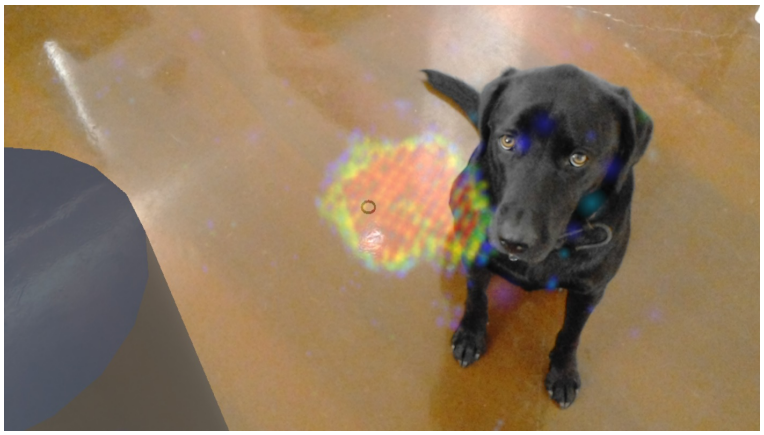

Figure 7.15: Thunderbird source displayed as a hologram as seen through a HoloLens. The corner of a virtual MINER detection system is on the left, and a bemused dog on the right.

7.10 Conclusions

A new method for 3D reconstruction of sources that emit correlated gamma rays and neutrons was demonstrated. The technique is distinguished from traditional 3D radiation imaging methods by only requiring a single-sided measurement of the source. Parallax by comparison would be restricted by system size and require close enough source-to-detector distances to function at all. This makes the $\gamma-n-n$ technique potentially valuable for nuclear inspection, emergency response and treaty verification, where multiple views of the object of interest may be restricted, even though the location of the source is known. The method proposed here is an extension of double neutron scatter imaging, combined with a correlated gamma ray to constrain the source location to the third dimension.

It is possible to resolve two sources of equal strength 10 cm apart using a portable scatter camera with sub-optimal timing and angular resolution. Simulated results with improved detector system resolution show a substantial improvement in radial resolution, and a modest improvement in angular resolution. Such improvements should be attainable with current technology, such as new photo-detectors like SiPMs. Furthermore, the detector cell geometry and size could be further optimized to improve localization resolution while maintaining adequate efficiency.

The efficiency of detecting a correlated neutron-gamma pair decreases as r^{-4}, where r is the

radial distance between source and detector system center. Therefore, it is not an ideal technique for standoff detection, although efficiency could be scaled with number and size of detector cells. However, this technique could prove valuable in application where access to the object of interest is limited. For example, this could include inspection of nuclear facilities for safeguards or treaty verification. Furthermore, neutron sources that emit correlated gamma rays (e.g. fission, (α,n)) are ubiquitous and include the vast majority of sources of concern in the aforementioned applications.

CHAPTER 8

Summary, Conclusions and Future Work

8.1 Summary and Conclusions

This thesis explored a new method for probing fission chain dynamics through correlated measurements of gamma rays and neutrons. Fission chains are a defining and unique feature of fissile material, whose detection and characterization is needed for diverse applications such as nonproliferation, safeguards, emergency response, and treaty verification. The context of those applications was given in Chapter 1. Chapter 2 explains the basic definitions and properties of fissile material, along with an overview of established measurement techniques. However, these techniques were historically developed around neutron counting with thermal capture detectors. The alternative use of organic scintillators proposed in this work provides three new capabilities:

1. Fast (sub-nanosecond) timing resolution, which allows for distinction between fission events in a chain.

2. Measurement of elastic proton recoil, which puts an upper bound estimate on the incident neutron energy.

3. Gamma ray detection, which provides a clean start time of a fission event that gave birth to the detected particle.

The best practices and methodology for extracting that relevant information from digitized pulses is laid out in Chapter 3. In prior work, these signatures were combined into TCPH distri-

butions, which were shown to be sensitive to fissile material and neutron multiplication [41, 42]. In Chapter 4 TCPH analysis was advanced by building an empirical model, and fitting it to measured distributions. The results showed that TCPH distributions were not only sensitive to the level of neutron multiplication, but also the type of reflector material. However, the methodology was somewhat convoluted, partly due to the two-dimensional aspect of TCPH.

The TOFFEE distribution was introduced in Chapter 5, which combined the same signature of TCPH, but into a one-dimensional distribution. A template-based approach was used to test TOFFEE in two treaty verification scenarios: dismantlement and item confirmation. In the former case, WGPu and HEU with and without reflector were compared, and the latter involved a test to determine the authenticity of the same fissile materials surrounded by a reflector. Under an arbitrary performance threshold of 99% True Positive (TP) and 1% False Positive (FP) the WGPu objects were verified within several seconds. By contrast, HEU confirmation required several minutes, because of the limited number of induced fissions created even under active interrogation. These tests revealed that TOFFEE was sensitive to the amount and configuration of fissile material, but did not provide a characterization of the object.

In depth characterization required a physical model, which was developed in Chapter 6 from two-region point kinetics theory. The resulting equations provided the time-dependent neutron populations in fissile material surrounded by a reflector, which were fitted to the positive side of the TOFFEE distribution. Positive linear relationships were established between the estimated and actual prompt neutron periods of the bare cases. And same trends were evident between estimated and actual neutron multiplication of the reflected cases. The estimated physical parameters also provided a way to discriminate between different reflector material types, from lightweight aluminum to heavy tungsten.

Chapter 7 introduced a new 3D technique enabled by detection of a correlated gamma ray with a double scatter neutron. Preliminary proof-of-concept measurements of Cf-252 showed that it is possible to resolve sources that are 10 cm apart, even with a neutron scatter camera with optimized for efficiency rather than resolution. Possibilities with better performing and possible

future systems was explored through simulations. Uncertainty quantification was provided as a guide for improvement of future detection systems. Finally, AR was proposed as the best way of visualizing the reconstructed 3D images.

8.2 Future Work

An alternative approach could be explored which combines the elements of analysis presented in Chapters 4 and 5. The empirical model of the TCPH distribution started with a like-fission distribution, and then smeared it to incorporate the perturbation from fission chain dynamics. TOFFEE distributions showed that the difference between non-multiplying and multiplying measurements is the addition in generation time, T_g, between detected correlated particles in the latter. Therefore, the distribution of generation time differences of fissions in a chain, convolved with the TOFFEE distribution built from only like-fission events, should produce the TOFFEE distribution expected from a multiplying fissile material. A Cf-252 measurement could be a surrogate for like-fission TOFFEE distribution. And the distribution of fission generation time differences could be built with either Monte Carlo, or a variation on the two-region point kinetics model shown in Chapter 5. Regardless of the means of creating that distribution, the underlying physical parameters would provide relevant information about measured fissile material.

The 3D imaging technique was proven to work with Cf-252, but the implicit assumption is that the detected gamma ray and neutron are born at the same space and time. This assumption does not hold in the presence of fission chains, therefore additional work is required to image fissile material. To solve this problem, it's necessary to develop a method which could determine and compensate for the time and space difference between birth of correlated particles. A solution would provide a way to simultaneously image fissile material, and measure the underlying fission chain dynamics. This is actually a difficult problem, and may require assumptions about the average distance separating fission events in a chain. But a successful effort would provide a way for a passive imaging system to reconstruct both the average fission chain length (multiplication) and

the volumetric distribution of fissile material from a single measurement.

APPENDIX A

Source Code

A.1 Pulse Parsing

```
''' Raw wavedata processing module

This module is designed to clean waveform and time tag data and also
return amplitude and PSD parameters
'''

import numpy as np
from scipy import integrate
import matplotlib.pyplot as plt
import operator

def time_order(time_stamps, freq=250, ts_bits=31):
  """ Orders time stamps sequentially

  Time stamps which oscillate due to number of bits are re-ordered
  sequentially. This function may be useful for cases where full waveforms
  are not saved but time stamps are still necessary for analysis.

  Parameters
  ----------
  time_stamps: array,  shape (N,), optional
    Timestamps of the digitizer, must be the same length as number
    of waves.
  freq: int, optional
    Frequency of the time clock in MHz
    default is 250
  ts_bits: int, optional
    Number of bits of the stored time stamp value, which determines
    the maximum timestamp value (2**ts_bits).
    default is 31

  Returns
  -------
  time_ns: array
    Event times in ns
  """
```

```
    negindx = np.flatnonzero(np.diff(time_stamps*1.)<0)
    time_ns = time_stamps*1.
    for i in negindx:
      time_ns[i+1:]+=2.**ts_bits
    time_ns = time_ns*1./(freq*1.e6)*1.e9
    if (np.diff(time_ns)<0).any():
      raise Exception("Time stamps are not sequential, check clock inputs!")
    return time_ns

  class Eventdata(object):
    '''
    Object that processes waveforms and timestamps, to produce amplitude,
    pulse shape discrimination parameters and time of events. Multiple
    methods are available for psd and time pick-off.

    Parameters
    ----------
    waves: ndarray, shape (N, wave_length):
      Raw waves from the digitizer

    Examples
    --------
    Take raw negative polarity pulses, invert, baseline subtract, apply
       threshold
    and extract amplitude, pulse shape parameters and timing.

    >>> import snappy.waveparser as wp
    >>> import numpy as np
    >>> from scipy.stats import lognorm
    >>> num_waves = 10000
    >>> x = np.arange(100)
    >>> waves = 2.**14 - 100 - np.random.normal(lognorm.pdf(np.tile(x,(num_waves
       ,1)),10,20)*1000)
    >>> ev = wp.Eventdata(waves)
    >>> ev.invert(dynamic_range=14)
    >>> ev.baseline(bline=5)
    >>> ev.threshold(threshold=200, ceiling=500, mode='sum')
    >>> amp = ev.get_amp(mode='sum')
    >>> psd = ev.psd_cdf(frac=0.2, 0.9)
    >>> time_stamps = np.floor(np.linspace(0,2**31,num_waves))
    >>> time_ns = ev.time_derivative(fraction=0.5, delay=1, time_stamps=
       time_stamps, freq=500)
    '''

    def __init__(self, waves):
      self.waves = waves

    waves = property(operator.attrgetter('_waves'))
    @waves.setter
    def waves(self, w):
      if w.ndim != 2: raise Exception("Waves must be a 2D array")
      self._waves = w
      self.reset()

    def reset(self):
      ''' Resets all attributes to initial instance creation

      Function may be useful when setting different thresholds levels form
```

```
    the command line.
    '''
    self.ind_clean = np.arange(self.waves.shape[0]) # indexes of cleaned
        arrays
    self.pulses = self.waves.copy()

  def invert(self, dynamic_range):
    ''' Inverts waveforms if they are negative polarity

    Parameters
    ----------
    dynamic_range: int
      The number of bits in the dynamic range of the digitizer, which
      determines the maximum value in waves (2**dr_bits).
    '''

    self.pulses = 2**dynamic_range - self.pulses

  def baseline(self, bline=5):
    ''' Applies baseline correction

    Parameters
    ----------
    bline: int
      Number of points used for baseline subtraction at the begining
      of the pulse train
      default is 5
    '''
    self.pulses = self.pulses-np.mean(self.pulses[:,0:bline],axis=1,keepdims=
        True,dtype='i4')

  def threshold(self, threshold, ceiling=np.inf, mode='trapz'):
    ''' Applied a threshold cutting out some pulses

    Parameters
    ----------
    threshold: float
      Threthold in digitizer units below which to cut out the pulses.
    ceiling: float
      Upper threshold above which pulses are cut, default is inf.
    '''
    amp = self.get_amp(mode)
    remove_ind = np.where(np.logical_or(amp<threshold, amp>ceiling))[0]
    self.ind_clean = np.delete(self.ind_clean, remove_ind)
    keep_ind = np.where(np.logical_and(amp>=threshold, amp<=ceiling))[0]
    self.pulses = self.pulses[keep_ind]

  def plot_pulses(self, pnum):
    ''' Plot some number of random pulses

    Parameters
    ----------
    pnum: int
      Number of waves to plot
    '''

    ind = np.random.randint(0, self.pulses.shape[0], pnum)
    plt.plot(self.pulses[ind].T)
```

```
    plt.show()

  def get_amp(self, mode='trapz'):
    """ Calculate wave amplitude of the waveform

    Parameters
    ----------
    mode: {'trapz', 'peak', 'sum'}:
      The type of camplitude calculation to perform

    Returns
    -------
    amp: array
      Estimation of the amplitude of the
    """

    if (mode=='trapz'):
      self.amp = np.trapz(self.pulses)
    elif (mode=='peak'):
      self.amp = self.pulses.max(1)
    elif (mode=='sum'):
      self.amp = self.pulses.sum(1)
    else:
      raise ValueError("Invalid input for mode")
    return self.amp

  def psd_ratio(self, sgate, lgate, prior=5):
    ''' Calculated the psd parameter using charge integration technique.

    Parameters
    ----------
    sgate: int
      Length of the short gate, in digitizer units.
    lgate: int
      Length of the long gate, in digitizer units
    prior (int): Number of points before pulse.

    Returns
    -------
    psd: ndarray, shape (N,)
      1-D array of PSD parameters corresponding to each wavelendth
    '''

    numW, lenW = self.pulses.shape
    lamp = np.zeros(numW)
    samp = np.zeros(numW)
    ind_max = self.pulses.argmax(axis=1)
    lstart = ind_max-prior
    lend = lstart+lgate
    send = lend
    sstart = send - sgate
    for i in range(numW):
      # check if the pulse is valid
      if (lstart[i]>0 or sstart[i]>0 or lend[i]<lenW or send[i]<lenW):
        lamp[i] = self.pulses[i,lstart[i]:lend[i]].sum()
        samp[i] = self.pulses[i,sstart[i]:send[i]].sum()
    psd = np.nan_to_num(samp*1./lamp)
    return  psd
```

```
def psd_cdf(self, frac1=0.1, frac2=0.9):
  ''' Calcate the time between fractional integrals of the pulse

  Uses the trapizoidal rule to calculate the time at a fraction of the
  total pulse integral, and uses the difference to calculate the PSD
  parameter.

  Parameters
  ----------
  frac1: float
    First integral fraction, the default is 0.1.
  frac2: float
    Second integral fraction.

  Returns
  -------
  psd: array, shape (N,)
    PSD parameters correspinding to each pulse in the train.
  '''

  prob = integrate.cumtrapz(self.pulses) / integrate.trapz(self.pulses)[:,
      None]
  nrow, ncol = prob.shape
  rows = np.arange(nrow)
  time = np.zeros(shape=(2,nrow))
  for i, f in enumerate([frac1, frac2]):
    y0 = np.argmax(prob>f,axis=1)-1
    x0 = prob[rows,y0]
    x1 = prob[rows,y0+1]
    time[i] = y0 + np.divide((f-x0),(x1-x0))
  time = np.nan_to_num(time)
  psd = time[1]-time[0]
  return psd

def time_cdf(self, tfrac, time_stamps, freq=250, ts_bits=31):
  ''' Returns event time using fractional integral of the pulse

  The cdf of each pulse is calculated and the time at some constant
  fraction of it is used. This method should not be used for data with
  pulses of varying shapes, as with mixed neutron and gamma data sets.

  Parameters
  ----------
  tfrac: float
    Fraction of cummulative integral for time pickoff
  time_stamps: array,  shape (N,)
    Timestamps of the digitizer, must be the same length as number
    of waves.
  freq: int, optional
    Frequency of the time clock in MHz
    default is 250
  ts_bits: int, optional
    Number of bits of the stored time stamp value, which determines
    the maximum timestamp value (2**ts_bits).
    default is 31

  Returns
```

```
    -------
    time_ns: array, shape (N,)
      Array of event times in nanoseconds associated with each pulse.

    Notes
    -----

    .. figure:: ../../../images/time_cdf.png
      :align:   center
      :width: 10cm

      A pulse and the corresponding cdf from which the time is picked
      based on some constant fraction.
    '''

    if (time_stamps.size != self.waves.shape[0]):
      raise ValueError("Number of time stamps must match number of waves!")
    time_stamp_ns = time_order(time_stamps, freq, ts_bits)
    time_stamp_ns = time_stamp_ns[self.ind_clean]
    prob = integrate.cumtrapz(self.pulses) / integrate.trapz(self.pulses)[:,
        None]
    nrow, ncol = prob.shape
    rows = np.arange(nrow)
    time = np.zeros(shape=(1,nrow))
    for i, f in enumerate([tfrac]):
      y0 = np.argmax(prob>f,axis=1)-1
      x0 = prob[rows,y0]
      x1 = prob[rows,y0+1]
      time[i] = y0 + np.divide((f-x0),(x1-x0))
    time = np.nan_to_num(time)
    time[0][time[0]<0] = 0
    time_ns = time_stamp_ns + time[0]/(freq*1.e6)*1.e9
    return time_ns

  def time_derivative(self, fraction, delay, time_stamps, freq=250, ts_bits
      =31):
    ''' Returns event time using derivative method.

    This method takes each wave and with delay subtracts some fraction
    of itself. When `fraction` and `delay` are both one this method is
        equivalent
    to taking the derivative of the pulse and looking for the zero crossing
    time.

    The optimal `fraction` will depend on pulse shape, a larger delay has
    the affect of smoothing the pulse. Typically a `delay=1` is
    sufficient.

    Parameters
    ----------
    fraction: float
      Fraction of the initial pulse to subtract
    delay: int
      The delay of the pulse that will be subtracted
    time_stamps: array,  shape (N,)
      Timestamps of the digitizer, must be the same length as number
      of waves.
    freq: int, optional
```

```
    Frequency of the time clock in MHz
    default is 250
  ts_bits: int, optional
    Number of bits of the stored time stamp value, which determines
    the maximum timestamp value (2**ts_bits).
    default is 31

  Returns
  -------
  time_ns: array, shape (N,)
    Array of event times in nanoseconds associated with each pulse.

  Notes
  -----
  This method is equivalent to the digital implementation of analog
  constant fraction disrimination, see [1]_.

  .. figure:: ../../../images/time_derivative.png
    :align:   center
    :width: 10cm

    A pulse and the corresponding derivative, the zero crossing time
    is used for time estimation.

  References
  ----------
  .. [1]      A. Fallu-Labruyere, H. Tan, W. Henning, W.K. Warburton, "Time
     resolution studies using digital constant fraction discrimination",
     Nucl. Inst. Meth. Section A, vol. 579, 1, pp. 247-251, 2007.

  '''

  if (time_stamps.size != self.waves.shape[0]):
    raise ValueError("Number of time stamps must match number of waves!")
  time_stamp_ns = time_order(time_stamps, freq, ts_bits)
  time_stamp_ns = time_stamp_ns[self.ind_clean]
  diff = self.pulses[:,1*delay:]*fraction - self.pulses[:,:-1*delay]
  x_max = diff.argmax(1)
  # shift diff by x_max, each row is independent
  rows, column_indices = np.ogrid[:diff.shape[0], :diff.shape[1]]
  roll = diff.shape[1] - x_max
  roll[roll < 0] += diff.shape[1]
  column_indices = column_indices - roll[:,np.newaxis]
  diff_shift = diff[rows, column_indices]
  # find index after zero crossing
  x2 = np.argmax(diff_shift<0,1) + x_max
  x2[x2>=diff.shape[1]] = diff.shape[1]-1
  x1 = x2-1
  y1 = diff[range(diff.shape[0]), x1]*1.
  y2 = diff[range(diff.shape[0]), x2]*1.
  time = x1*1. + y1*1./(y1-y2)
  time = np.nan_to_num(time)
  time_ns = time_stamp_ns + time/(freq*1.e6)*1.e9
  return time_ns
```

A.2 Pulse Shape Discrimination

```
''' PSD data processing module

Module for turning PSD parameters into probabities for a number of desired
classes.
'''

import numpy as np
import matplotlib.pyplot as plt
from matplotlib.colors import LogNorm
from scipy.optimize import curve_fit
from scipy.cluster.vq import kmeans2, whiten
import pickle
from scipy import interpolate

def skew2(x, E, S1, S2):
  ''' Skew normal distribution

  Args:
    x (array[T]):  An array of data points for each slice.
    E  (array[K]): Means for each class.
    S1 (array[K]): Positive standard deviation for each class.
    S2 (array[K]): Negative standard deviation for each class.
  Returns:E
    y (array[K, T]): Normalized skewed gaussian values
  '''

  # check if input it the proper format
  if not np.isscalar(E) and E.size>1: E = np.reshape(E, (-1,1))
  if not np.isscalar(S1) and S1.size>1: S1 = np.reshape(S1, (-1,1))
  if not np.isscalar(S2) and S2.size>1: S2 = np.reshape(S2, (-1,1))

  return 2./(S1+S2)* (normpdf(x,E,S1)*(x>=E) + normpdf(x,E,S2)*(x<E))

def normpdf(x, mu, sigma):
  ''' Calculate the normalized Gaussian values.

  Args:
    x (array[T]): Array of values.
    mu (array[K]): Array of means for each class.
    sigma (array[K]): Array of means for each class.
  Returns:
    y (array[K,T]): Array of gaussian values.
  '''
  mu = np.array(mu)
  sigma = np.array(sigma)
  if mu.size>1 : mu = mu.reshape((-1,1))
  if sigma.size>1 : sigma = sigma.reshape((-1,1))
  u = (x-mu)/np.abs(sigma)
  y = (1./(np.sqrt(2.*np.pi)))*np.exp(-u*u/2.)
  return y

def gauss_2(x, alpha, E_0, E_1, S1_0, S1_1):
  ''' Returns best double gaussian fit
  This is a workaround so the function can be called by curve fitting tool
  '''
```

```
  return (alpha*normpdf(x, E_0, S1_0)/S1_0 + (1.-alpha)*normpdf(x, E_1, S1_1)/
      S1_1)

def gauss_1(x, E_0, S1_0):
  ''' Returns best single gaussian fit

  This is a workaround so the function can be called by curve fitting tool
  '''
  return normpdf(x, E_0, S1_0)/S1_0

def calcProb(x, w, E, S1, S2):
  ''' Calculates the posterior-probability (P(K|x,D)) for each point x and
      class K

  Args:
    x: (array[T]): Array of PSD parameters.
    w  (array[K]): Weight for each class.
    E  (array[K]): Means for each class.
    S1 (array[K]): Positive standard deviation for each class.
    S2 (array[K]): Negative standard deviation for each class.
  Returns:
    probs (array[K,T]): Probabilities for each class for each event.
  '''

  # Check number of weights passed
  if not np.isscalar(w) and w.size>1:
    w = np.reshape(w,(len(w),1))
    # quick and dirty solution
    p_probs = w*skew2(x, E, S1, S2)
    '''
    if w.size==2:
      p_probs[0] = p_probs[0]*(x<E[1])
      p_probs[1] = p_probs[1]*(x>E[0])
    '''
    probs = np.divide(p_probs,np.sum(p_probs+1e-6,axis=0))
  else:
    probs=np.ones(len(x))
  probs[np.isnan(probs)] = 1e-16

  return probs

def calcE(x,prob,E,S1,S2):
  ''' Calculate the new epsilon (related to mean
  Args:
    x (array[T]):   Array of PSD parameters.
    prob (array[K,T]): Array of posterior probabilities for each point.
    E  (array[K]): Means for each class.
    S1 (array[K]): Positive standard deviation for each class.
    S2 (array[K]): Negative standard deviation for each class.
  Returns:
    E (array[K]): New means for each class.
  '''
  if not np.isscalar(E) and E.size>1:
    E = np.reshape(E, (len(E),1))
    ax=1
  else:
    ax=0
  return (S2**2.*np.sum(x*prob*(x>=E), axis=ax) + S1**2.*np.sum(x*prob*(x<E),
```

```
      axis=ax)) / \
          (S2**2.*np.sum(prob*(x>=E), axis=ax) + S1**2.*np.sum(prob*(x<E), axis
             =ax))

def calcS(x,E,prob):
  ''' Calculate the new standard deviations

  Args:
    x (array[T]): Array of PSD parameters.
    E (array[K]): Array of means for each class.
    prob (array[T,K]): Array of posterior probabilities for each point.
  Returns:
    S1 (array[K]): Array of posisitve standard deviations for each class.
    S2 (array[K]): Array of negative standard deviations foe each class.
  '''

  E = np.array(E)
  if E.size>1:
    E = E.reshape((-1,1))
    ax = 1
  else:
    ax = 0

  C = np.sum(prob,axis=ax)
  C1 = np.sum((x-E)**2.*prob*(x<E), axis=ax)
  C2 = np.sum((x-E)**2.*prob*(x>=E), axis=ax)
  S2 = (C1/C*(1.+(C2/C1)**(1./3)))**(1./2)
  S1 = (C2/C*(1.+(C1/C2)**(1./3)))**(1./2)
  return S1, S2

# change this to accept probabilities and then calculate skew2 by itself
def calcLogLike(x, probs, w, E, S1, S2):
  ''' Calculate the log likelehood given probability, weight and parameters.

  Args:
    x (array[T]):  An array of data points for each slice.
    probs (array[K,T]): Array of posterior probabilities for each point.
    E  (array[K]): Means for each class.
    S1 (array[K]): Positive standard deviation for each class.
    S2 (array[K]): Negative standard deviation for each class.
  Returns:
    Q (float): Log-likelihood.
  '''
  w = (np.array(w)).reshape((-1,1))
  Q = np.sum(np.log(w)*probs) +  np.sum(np.log(skew2(x,E,S1,S2)+1e-16)*probs)
  return Q

def calcskewEM(x, maxiter, eps, w, E, S1, S2, update=None):
  ''' Calculate skew parameters using Exepctation Maximization Algorithm

  Args:
    x (array[T]):  An array of data points for each slice.
    maxiter (int) :  Maximum number of iterations.
    eps (float)   :  The log-likelihood difference to terminate iteration
    w  (array[K]): Initial guess weight for each class.
    E  (array[K]): Initial guess means for each class.
    S1 (array[K]): Initial guess positive standard deviation for each class.
    S2 (array[K]): Initial guess negative standard deviation for each class.
```

```
  update (array[K]): Which classes should have variables updated.
Returns:
  probs (array[K,T]): Posterior probabilities for each class.
  w (array[K]): New weights for each class.
  E  (array[K]): New means for each class.
  S1 (array[K]): New positive standard deviation for each class.
  S2 (array[K]): New negative standard deviation for each class.
'''

# Convert imput into numy array and check for equal size.
w = np.asarray(w,dtype=float)
E = np.asarray(E,dtype=float)
S1 = np.asarray(S1,dtype=float)
S2 = np.asarray(S2,dtype=float)
if not (w.size==E.size==S1.size==S2.size):
  raise ValueError("All of the initial guesses must be equal size")
if update==None: update = np.ones(w.size, dtype=bool)
T = len(x)
iters = 0
while (maxiter>iters):
  # step 1: Calculate initial posterior probabilities
  if iters==0: probs = calcProb(x, w, E, S1, S2)
  # step 2: Calculate new weights for each class.
  w = np.asarray(np.sum(probs.T,axis=0)/T)
  # calculate the other parameters only if requested
  if (np.sum(update)>0):
    # step 3: Calculate new means given new weights.
    probs = calcProb(x, w, E, S1, S2)
    Enew = calcE(x, probs, E, S1, S2)
    # check if variables need to be updated
    if (Enew.size>1):
      for  i in range(Enew.size):
        if update[i]: E[i] = Enew[i]
    else:
      if update: E = Enew
    # step 4: Calculate new std given new means and weights
    probs = calcProb(x, w, E, S1, S2)
    S1new, S2new = calcS(x, E, probs)
    if (S1new.size>1):
      for  i in range(S1new.size):
        if update[i]:
          S1[i] = S1new[i]
          S2[i] = S2new[i]
    else:
      if update:
        S1 = S1new
        S2 = S2new
  # step 5: Calculate new probability and check log-likelihood
  probs = calcProb(x, w, E, S1, S2)
  if iters>0:
    loglike_new = calcLogLike(x, probs, w, E, S1, S2)
    if (eps>np.abs(1-loglike_old/loglike_new)):
      break
    loglike_old = loglike_new
  else:
    loglike_old = calcLogLike(x, probs, w, E, S1, S2)
  iters+=1
if maxiter==iters:
```

```
    print "Warning! Maximum number of iterations exceeded \n"
  return probs, w, E, S1, S2

def calcGaussEM(x, maxiter, eps, w, E, S1, update=None):
  ''' Calculate Gaussian parameters using Exepctation Maximization Algorithm

  Args:
    x (array[N]):   An array of data points for each slice.
    maxiter (int) :  Maximum number of iterations.
    eps (float)   :  The log-likelihood difference to terminate iteration
    w  (array[K]): Initial guess weight for each class.
    E  (array[K]): Initial guess means for each class.
    S1 (array[K]): Initial guess positive standard deviation for each class.
    update (array[K]): Which classes should have variables updated.
  Returns:
    probs (array[K,N]): Posterior probabilities for each class.
    w (array[K]): New weights for each class.
    E  (array[K]): New means for each class.
    S1 (array[K]): New positive standard deviation for each class.
  '''

  # Convert imput into numy array and check for equal size.
  w = (np.asarray(w,dtype=float))
  E = np.asarray(E,dtype=float)
  S1 = np.asarray(S1,dtype=float)
  if not (w.size==E.size==S1.size):
    raise ValueError("All of the initial guesses must be equal size")
  if update==None: update = np.ones(w.size, dtype=bool)
  N = len(x)
  iters = 0
  while (maxiter>iters):
    # step 1: Calculate initial posterior probabilities
    if iters==0:
      probs = calcProb(x, w, E, S1, S1)
    # step 2: Calculate new weights for each class.
    Nk = np.sum(probs.T, axis=0)
    w = (np.asarray(Nk/N))
    # calculate the other parameters only if requested
    if (np.sum(update)>0):
      # step 3: Calculate new means given new weights.
      probs = calcProb(x, w, E, S1, S1)
      ax=0
      if w.size>1: ax=1
      Enew =  (1./Nk)*np.sum(probs*x, axis=ax)
      # check if variables need to be updated
      if (Enew.size>1):
        for  i in range(Enew.size):
          if update[i]: E[i] = Enew[i]
      else:
        if update: E = Enew
      # step 4: Calculate new std given new means and weights
      probs = calcProb(x, w, E, S1, S1)
      if w.size>1:
        S1new = (1./Nk) * np.sum(probs*(x-E.reshape((-1,1)))**2.,axis=1)
      else:
        S1new = (1./Nk) * np.sum(probs*(x-E)**2.,axis=0)
      S1new = np.sqrt(S1new)
      if (S1new.size>1):
```

```
        for  i in range(S1new.size):
          if update[i]: S1[i] = S1new[i]
      else:
        if update: S1 = S1new
    # step 5: Calculate new probability and check log-likelihood
    probs = calcProb(x, w, E, S1, S1)
    if iters>0:
      loglike_new = calcLogLike(x, probs, w, E, S1, S1)
      if (eps>np.abs(1-loglike_old/loglike_new)):
        break
      loglike_old = loglike_new
    else:
      loglike_old = calcLogLike(x, probs, w, E, S1, S1)
    iters+=1
  if maxiter==iters:
    print "Warning! Maximum number of iterations exceeded \n"
  S2 = S1
  return probs, w, E, S1, S2

def calcCurve(x, w, E, S1, S2):
  ''' Curve fits a single skewed Gaussian or normal double Gaussian

  Instead of using EM algorithm this function performs curve fitting, this
  is ideal for distribtuions with only a singgle class (gamma measurements)
  where EM could struggle with outliers.
  '''
  if w.size>2:
    raise ValueError("Curve fitting works on maximum of 2 classes")
  ydata, xdata = np.histogram(x,bins=100,normed=True)
  xdata = xdata[:-1] + 0.5 * (xdata[1:] - xdata[:-1])
  pinit = (E,S1)
  if w.size==1:
    E, S1 = curve_fit(gauss_1, xdata, ydata, p0= pinit)[0]
    w = np.asarray(1.)
  # performs a double gaussian fit
  else:
    ret = curve_fit(gauss_2, xdata, ydata, p0= np.append(w[0],pinit))[0]
    w = np.array([ret[0],1.-ret[0]])
    E = ret[1:3]
    S1 = ret[3:5]
  S2 = S1
  probs = calcProb(x, w, E, S1, S2)
  return probs, w, E, S1, S2

def bindata(psd, amp, isa, mincounts=5000, maxbinwidth = 20000):
  """ Creates bins along amplitude with an equal number of counts in each.

  Args:
    psd (array[T]): PSD data to be divided along amplitude bins.
    amp (array[T]): Amplitude data.
    isa (array[T]): Values by which amplitude is sorted by.
    mincounts (int): Minimum number of counts in each bin.
    maxbinwidth (int): Maximum allowable bin width
  Returns:
    x_bin (array[T,K]): Matrix of psd value with each row corresponding to
       seperate bin.
    xedges (array[K+1]): Amplitude value of the edges of each bin.
    xcenters (array[K]): Amplitude value of the centers of each bin.
```

```
    """
    amp = amp[isa]
    psd = psd[isa]
    ampbins = np.floor(amp.size/mincounts)
    a_bin = np.array_split(amp, ampbins)
    i_bin = np.array_split(isa, ampbins)
    xedges = [a[0] for a in a_bin]
    xedges.append(amp.max()) # add the right most edge
    xedges = np.asarray(xedges)
    xcenters = xedges[:-1] + 0.5 * (xedges[1:] - xedges[:-1])
    x_bin = np.array_split(psd,ampbins)
    # add bins if the maximum bin is exceeded
    lastbinwidth = xedges[-1]-xedges[-2]
    if (lastbinwidth>maxbinwidth):
      amphigh = np.hstack(a_bin[-1])
      psdhigh = np.hstack(x_bin[-1])
      isahigh = np.arange(len(amphigh))
      x_bin2, xedges2, xcenters2 = bindatawidth(psdhigh, amphigh, isahigh, np.
          floor(lastbinwidth/maxbinwidth))
      # clean up old and add the new
      xedges = np.append(xedges[:-2],xedges2)
      xcenters = np.append(xcenters[:-1],xcenters2)
      x_bin.pop()
      x_bin = x_bin + x_bin2
    return x_bin, xedges, xcenters

def bindatawidth(psd, amp, isa=None, ampbins=5):
    """ Creates bins along amplitude with an equal width in each.

    Args:
      psd : array[T]
            PSD data to be divided along amplitude bins.
      amp : array[T]
            Amplitude data.
      isa : array[T])
            Values by which amplitude is sorted by.
      ampbins : int
            Number of bins in each
    Returns:
      x_bin (array[T,K]): Matrix of psd value with each row corresponding to
          seperate bin.
      xedges (array[K+1]): Amplitude value of the edges of each bin.
      xcenters (array[K]): Amplitude value of the centers of each bin.
    """
    if isa==None:
      isa = np.argsort(amp)
    amp = amp[isa]
    psd = psd[isa]
    # decrease bin width until there is counts in a bin
    while (True):
      h = np.histogram(amp, ampbins)[0]
      # decrease the number of bins if less than 100 plots remain in a bin
      if sum(h<100)>0:
        ampbins-=1
      else:
        xedges = np.histogram(amp, ampbins)[1]
        break
    xcenters = xedges[:-1] + 0.5 * (xedges[1:] - xedges[:-1])
```

```
    split = np.where(np.diff(np.digitize(amp,xedges[:-1]))>0)[0]
    x_bin = np.split(psd,split)
    return x_bin, xedges, xcenters

def reject_outliers(data, m = 2.):
    d = np.abs(data - np.median(data))
    mdev = np.median(d)
    s = d/mdev if mdev else 0.
    return data[s<m]

def calcprobs(psd, amp, showslices=1e9, mincounts=5000, maxbinwidth=20000,
                  maxiter=1000, eps=1e-6, w=[0.5,0.5], E=[17,35], S1 =[1,1],
                  S2=[.1,.1], Efit=None, S1fit=None, S2fit=None, verbose=True,
                  fittype='EMskew', curve_cut=1e9):
    ''' Finds the posterior probabilities of all the data points in the class.

    Data is divided into K classes each modeled by a skewed-Gaussian. The
    number of classes is dependent on the number of initial parameters
    provided. The algorithm fits each slice starting with the highest
    amplitude to the lowest and uses initial guesses from the previous
    result as next initial guesses.

    If the fit interpolate object for parameters is provided then those
       parameters
    for each class are not recalculated, only the weight is recalculated.
    The parameters for classes in which fit was not provided are recalculated.

    If the number of minimum counts is not met in a particulair bin then
    a k-means algorithm is used to compute the mean and standard deviation.
    A gaussian shape is assumed for the computation of both parameters.


    Args:
      psd (array[T]): PSD data points.
      amp (array[T]): Corresponding amplitude data.
      showslices: Number of slices to skip between plotting fit results.
      mincounts (int, optional): Minimum counts in each amplitude bin.
      maxiter (int, optional): Maximum number of iteration for the EM algorithm.
      eps (float, optional): Exit condition for EM algorithm.
      w (array[K], optional): Initial weights for each class.
      E (array[K], optional): Initial means for each class.
      S1 (array[K], optional): Initial positiove standard deviation.
      S2 (array[K], optional): Initial negative standard deviation.
      Efit (array[K]): Array of interpolate objects.
      S1fit (array[K]): Array of interpolate objects.
      S2fit (array[K]): Array of interpolate objects.
      verbose: Output that prints to screen size.
      fittype: 'EM' or 'curve' option for type of fitting
      curve_cut: Above this value always perform curve fitting

    Returns:
      probs (array[K,T]): Posterior probabilities for each class.
      E_arr (array[K,S]): Means for each amplitude bin.
      S1_arr (array[K,S]): Positive std for each amplitude bin.
      S2_arr (array[K,S]): Negative std for each amplitude bin.
      ampcenters (array[S]): Array of amplitude centers.
    '''
```

```
# Convert imput into numy array and check for equal size.
if np.isscalar(w): w = np.array([w])
if np.isscalar(E): E = np.array([E])
if np.isscalar(S1): S1 = np.array([S2])
if np.isscalar(S2): S2 = np.array([S2])

w = np.asarray(w)
E = np.asarray(E)
S1 = np.asarray(S1)
S2 = np.asarray(S2)
if not (w.size==E.size==S1.size==S2.size):
  raise ValueError("All of the initial guesses must be euqal size")
# check the number of fits present
if not (Efit==None and S1fit==None and S2fit==None):
  num_fits = len(Efit)
  update = np.zeros(num_fits,dtype=bool)
  # The difference will be updated
  for i in range(w.size-num_fits):
    update = np.append(update, True)
  fits_passed = True
else:
  fits_passed = False
  update = None

isa = np.argsort(amp)
psd_bin, ampedges, ampcenters = bindata(psd, amp, isa, mincounts,
    maxbinwidth)

# correct for high energies

# fit everything going backwards
prob_arr = []
E_arr = []
S1_arr = []
S2_arr = []
for i in range(len(ampcenters)-1,-1,-1):
  # if fits where passed use those to get the next value
  if fits_passed:
    amp = ampcenters[i]
    E =  np.append( np.asarray([ x(amp) for x in Efit]), E[num_fits:])
    S1 = np.append( np.asarray([ x(amp) for x in S1fit]), S1[num_fits:])
    S2 = np.append( np.asarray([ x(amp) for x in S2fit]), S2[num_fits:])

  if len(psd_bin[i])>1000 and fittype!='kmeans':
    # for fitting only one parameter, curve fitting is better
    if fittype=='curve' or ampcenters[i]>curve_cut:
      probs, w, E, S1, S2 = calcCurve(psd_bin[i], w, E, S1, S2)
    elif fittype=='EMskew':
      probs, w, E, S1, S2 = calcskewEM(psd_bin[i], maxiter, eps, w, E, S1,
          S2, update)
    elif fittype=='EMgauss':
      probs, w, E, S1, S2 = calcGaussEM(psd_bin[i], maxiter, eps, w, E, S1,
          update)
  else:
    if (verbose): print 'Using k-means'
    # convert this into its own collable function
    data = psd_bin[i]
    E, l = kmeans2(data, k=E, minit='matrix')
```

```
      # somehow this has to sort
      w = np.array([])
      S1 = np.array([])
      for k in range(len(E+1)):
        d = data[l==k]
        #d = reject_outliers(d)
        S1 = np.append(S1, d.std())
        w = np.append(w,(l==k).sum(dtype=float))
      w = w/w.sum()
      S2 = S1
      probs = calcProb(psd_bin[i], w, E, S1, S2);
    # check that the output is correct
    if (np.sum( (np.isnan(w), np.isnan(E), np.isnan(S1), np.isnan(S2))) > 0):
      raise RuntimeError("EM failed on slice " + str(i) + " with amp " + str(
          ampcenters[i]))
    prob_arr.append(probs.copy())
    E_arr.append(E.copy())
    S1_arr.append(S1.copy())
    S2_arr.append(S2.copy())
    if (verbose): print "Done with slice: " + str(i)
    # plot some results if requested
    if (np.mod(i+1,showslices)==0):
      fx = np.linspace(psd_bin[i].min(),psd_bin[i].max(),1000)
      print w, E, S1, S2
      plt.title('Slice number: ' + str(i) + " Amp: " + str(ampcenters[i]))
      plt.hist(psd_bin[i],100,normed=True,histtype='step')
      plt.plot(fx,w*skew2(fx,E,S1,S2).T)
      plt.show()
  # sort the probabilities to the input amplitude order
  probs = np.hstack(list(reversed(prob_arr)))
  E_arr = np.array(list(reversed(E_arr))).T
  S1_arr = np.array(list(reversed(S1_arr))).T
  S2_arr = np.array(list(reversed(S2_arr))).T
  if len(probs.shape)>1:
    for k in range(probs.shape[0]):
      probs[k] = probs[k][np.argsort(isa)]
  else:
    probs = np.array([probs[np.argsort(isa)]])
    E_arr = np.array([E_arr])
    S1_arr = np.array([S1_arr])
    S2_arr = np.array([S2_arr])
  return probs, E_arr, S1_arr, S2_arr, ampcenters

def plotpsd(amp, psd, probs=None, pcut=[0.9,0.9]):
  ''' Plots psd results for each class
  '''
  if probs==None: probs = np.ones(len(amp))
  if len(probs.shape)>1:
    f, (ax1, ax2) = plt.subplots(2, sharex=True, sharey=True)
    ax1.set_title('Separated photons and neutrons.')
    ax1.hist2d(amp,psd,bins=[200,100],norm=LogNorm(),weights=(probs[0]>pcut
        [0]).astype(int),cmin=1)
    ax2.hist2d(amp,psd,bins=[200,100],norm=LogNorm(),weights=(probs[1]>pcut
        [1]).astype(int),cmin=1)
    plt.show()
  else:
    plt.hist2d(amp,psd,bins=[200,100],norm=LogNorm(),weights=probs,cmin=1)
    plt.show()
```

```
def plotpsdfit(amp, psd, psdfit, E, S1, S2, ampbins):
  ''' Plots psd results for each class
  '''
  # reshape ampbins if needed
  #ampbins = np.array(ampbins).reshape((len(E),-1))
  x = np.linspace(np.min(amp),np.max(amp),1000)
  plt.hist2d(amp,psd,bins=[200,100],norm=LogNorm(),cmin=1)
  for i in range(len(psdfit['E'])):
    # plot the fits
    plt.plot(x,psdfit['E'][i](x),'g',lw=3)
    plt.plot(x,psdfit['E'][i](x)+psdfit['S1'][i](x),'k',lw=3)
    plt.plot(x,psdfit['E'][i](x)-psdfit['S2'][i](x),'k',lw=3)
    # plot the individual points
    plt.plot(ampbins, E[i],'go')
    plt.plot(ampbins, E[i]+S1[i],'ro')
    plt.plot(ampbins, E[i]-S2[i],'ro')
  plt.show()

def getRecArr(prob, psd, amp, time):
  ''' Creates a reccord array that can be saved to a root file

  This function is purpose built for photons and neutrons being present,
  but it also lives as an example for other potential programs.
  '''
  wtype = np.dtype([('probG',prob[0].dtype),('probN',prob[1].dtype),
                    ('psd',psd.dtype),('amp',amp.dtype),('time',time.dtype)])
  w = np.empty(len(prob[0]),dtype=wtype)
  w['probG'] = prob[0]
  w['probN'] = prob[1]
  w['psd'] = psd
  w['amp'] = amp
  w['time'] = time
  return w

# turn this into a class
def fitpsdparms(E, S1, S2, ampbins, smooth, knot, fitnum=1):
  ''' Fits psd paramers with splines and returns dictionary of fits

  Spline fitting is performed on PSD parameters and saved in a dictionary.
  These fits can then be used to update the probability maps for subsequent
  measurements. The fitting is performed for K number of classes that are
  placed in the dictionary as splines in the same order.

  Args:
    amp: Amplitude of pulses (for plotting)
    psd: PSD parameter of pulses (also for ploting)
    E, S1, S2 (array[n,K]): Means and standard deviations of distributions.
    ampbins array([n,K]): Amplitude centers of each slice.
    smooth (array[3,K]): Array of smoothing parameters.
    knot (array[3,K]): Array of knots for the smoothing spline
    fitnum: number of fits
  Returns:
    psdfits: Dictionary of smooth spline fits for each parameter
  '''
  # reshape ampbins if needed
  # ampbins = np.array(ampbins).reshape((fitnum,-1))
  # Add values to the dictionary to be pickled
```

```
  psdfits = {}
  psdfits['E'] = []
  psdfits['S1'] = []
  psdfits['S2'] = []

  for i in range(fitnum):
    # means
    Efit = interpolate.UnivariateSpline(ampbins, E[i],k=knot[i][0],
                                        s=smooth[i][0])
    # standard deviations
    S1fit = interpolate.UnivariateSpline(ampbins, S1[i],k=knot[i][1],
                                         s=smooth[i][1])

    S2fit = interpolate.UnivariateSpline(ampbins, S2[i],k=knot[i][2],
                                         s=smooth[i][2])
    # Append everything to the correct dictionary value
    psdfits['E'].append(Efit)
    psdfits['S1'].append(S1fit)
    psdfits['S2'].append(S2fit)
  return psdfits


def savepsdfits(psdfits, output_fitfile):
  ''' Saves the dictionary of PSD fits to an output file

  The psd fit file should be saved once the fit for every channel is
  complete.

  Args:
    psdfits: Dictionary of fit functions for parameters
    output_fitfile: The destination file for saving the fits.
  '''
  fout = open(output_fitfile, 'w')
  pickle.dump(psdfits, fout)
  fout.close()
```

A.3 3D Imaging

```
'''
Series of functions for converting correlated data points into source
   locations this one includes uncertanties
'''

import numpy as np

def scattering_energy(dist, delT):
  '''
    Calculating neuton energy after scatter from first detector
  Parameters:
    dist: Distance between interactions
    delT: Travel time between interactions (ns)

  Return:
    Energy between two scatters
  '''
```

```
    m_n = 1.6749e-27
    delT = delT/1.e9
    erg1 = (m_n/2.) * ((dist/100)**2 / delT**2) * 6.242e12
    return erg1

def calc_incident(dist, delT, erg_dep):
    '''
      Calculate incident energy and opening angle of the cone
    Args:
      dist: Distance between interactions
      delT: The difference in time between two interactions
      erg_dep: energy deposited in first detector (MeV)
    '''
    # define constants append numbers to record array
    erg1 = scattering_energy(dist, delT)
    erg0 = erg_dep + erg1
    angle = np.arccos(np.sqrt(erg1/erg0))
    return angle, erg0

def rodrigues(k, v, theta, mode='uniform'):
    ''' Rotate vector v about axis of vector k by angle theta using the
    right hand rule

    Parameters:
      k: unit vector to turn on .
      v: unit vector being turned:
      theta: angle of rotation
      mode: Default = 'uniform', rotates all the vectors, 'specific', each
            vector is rotates according to corresponding angle
    Return:
      vn (data_points, cordinates, theta): Rotated vector n
    '''
    if mode=='uniform':
      vn = v[:,:,None]*np.cos(theta) + np.cross(k,v)[:,:,None]*np.sin(theta)+(k
          *(k*v).sum(1)[:,None])[:,:,None]*(1-np.cos(theta))
    elif mode=='specific':
      vn = v*np.cos(theta)[:,None] + np.cross(k,v)*np.sin(theta)[:,None]+(k*(k*v
          ).sum(1)[:,None])*(1-np.cos(theta))[:,None]
      vn = vn[:,:,None]
    return vn

def get_vector(p0, p1):
    '''
    Gets the vector and its magniture from two points
    p0 -------> p1
    Parameters:
      p0: First point
      p1: Secont point
    Returns:
      vec: Vector defined by two points
      dist: distance between two points (or magnitude of the vector)
    '''

    vec = p0-p1
    dist = np.sqrt(np.sum(vec**2,1))
    return vec, dist

def solve_R(f, d, v, t):
```

```
    '''
    Solves for the two possible solutions of R
    Args:
        d: distance between neutron and gamma (cm)
        v: speed of incident neutron (m/s)
        f: dot product of R unit vector and g-n unit vector
        t: time between gamma-neutron events (ns)
    Returns:
        R1, R2: The two solutions for R
    '''
    c = 3.e8
    d = d/100.
    t = t/1.e9
    f = f.T
    R = ( np.sqrt(v**2*(c**2*d**2 - 2*c**2*d*f*t*v + c**2*t**2*v**2 + d**2*f**2*
        v**2 - d**2*v**2 ))
          + c**2*t*v - d*f*v**2)/(c**2 - v**2)
    R = R.T
    return R*100.

def im3_type():
    '''
    Returns the 3d imaging data type which includes:
    n0loc (3,): Location (cm) of first neutron scatter
    n1loc (3,): Location (cm) of second neutron scatter
    gloc (3,): Location (cm) of the gamma interaction
    nnt : Time (ns) between first and second scatter
    gnt : Time (ns) between gamma and neutrons catter
    n0erg: Deposited energy in first neutron interaction
    '''
    im_type = np.dtype([('n0loc','float',3),('n1loc','float',3),('gloc','float'
        ,3),
                        ('nnt','float'),('gnt','float'),('n0erg','float')])
    return im_type

def im2_type():
    '''
    Returns the 2d imaging data type which includes:
    n0loc (3,): Location (cm) of first neutron scatter
    n1loc (3,): Location (cm) of second neutron scatter
    nnt : Time (ns) between first and second scatter
    n0erg: Deposited energy in first neutron interaction
    '''

    im_type = np.dtype([('n0loc','float',3),('n1loc','float',3),
                        ('nnt','float'),('n0erg','float')])
    return im_type

def cart2sphere(xyz):
    ''' Converts cartesian to spherical coordinates
    '''
    r = np.sqrt(np.sum(xyz**2,1))
    theta = np.arctan2(xyz[:,1],xyz[:,0])
    phi = np.arccos(xyz[:,2]/r)
    rtp = np.array([r,theta,phi]).T
    return rtp

def sphere2cart(rtp):
```

```
    ''' Converts spherical to cartisian coordinates
    '''
    x = rtp[:,0]*np.cos(rtp[:,1])*np.sin(rtp[:,2])
    y = rtp[:,0]*np.sin(rtp[:,1])*np.sin(rtp[:,2])
    z = rtp[:,0]*np.cos(rtp[:,2])
    xyz = np.array([x,y,z]).T
    return xyz

def get_source(data, n_thetas = 100):
    '''
    Returns source points in cartesian coordinates based on the input data

    Parameters:
      data: Record array of locations, times and energy in first neutron scatter
      n_thetas: Number of source locations to throw per cone, if 1 then uses
          random
                otherwise its a uniform distribution
    Return:
      source (n_evnets, 3 coordinates, n_thetas): Array of the possible source
          points based on the input.
        T
    '''

    # get the unit vector that defines the n-n scatter axis
    nn_vec, nn_d = get_vector(data['n0loc'], data['n1loc'])
    nn_hat = nn_vec/nn_d[:,None]
    # get vector and magnitude that definds the n-g axis
    ng_vec, ng_d = get_vector(data['gloc'], data['n0loc'])
    ng_hat = ng_vec/ng_d[:,None]
    # get energy and opening angle of the cone
    theta1, erg0 = calc_incident(nn_d, data['nnt'], data['n0erg'])
    v_n = np.sqrt(2.*erg0/(939.5/3.e8**2))
    # decline nn_hat by the opening angle of the cone
    norm_nn = np.cross([1,1,1],nn_hat)
    norm_nn = norm_nn/np.sqrt(np.sum(norm_nn**2.,1))[:,None]
    ns_hat = nn_hat*np.cos(theta1)[:,None]+np.sin(theta1)[:,None]*np.cross(
        norm_nn,nn_hat)
    # rotate ns_hat around given azimuthal angle around the cone
    if n_thetas>1:
      cone_thetas = np.linspace(0,np.pi*2,n_thetas)
      cone_hat = rodrigues(nn_hat, ns_hat, cone_thetas, mode='uniform')
    else:
      cone_thetas = np.random.rand(ns_hat[:,0].size)*2*np.pi
      cone_hat = rodrigues(nn_hat, ns_hat, cone_thetas, mode='specific')
    # calculate distance r for each point and get the final source point
    f = (cone_hat*ng_hat[:,:,None]).sum(1) # cosine of angles between cone
        surface and n-g vector
    Rn = solve_R(f, ng_d, v_n, data['gnt'])
    source = cone_hat*Rn[:,None] + data['n0loc'][:,:,None]

    return source
```

APPENDIX B

Math

B.1 3D Imaging

The solution to the quadratic equation, shown Section 7.4, that yields the distance from the fist neutron interaction to the source along the length of the projected cone is

$$R_n = \frac{c^2 t_{\gamma,n} v_n - d v_n^2 \mu \pm \sqrt{v_n^2 \left(c^2 (t_{\gamma,n}^2 v_n^2 - 2 d v_n \mu t_{\gamma,n} + d^2) + v_n^2 d^2 (\mu^2 - 1) \right)}}{c^2 - v_n^2} \tag{B.1}$$

The proof will demonstrate that only one of those roots is a valid solution, because the speed of the neutron has to be less than the speed of light $v_n < c$. First, Eq. 7.8 can be rearranged to solve for source-gamma distance:

$$R_\gamma = c \left(\frac{R_n}{v_n} - t_{\gamma,n} \right) \tag{B.2}$$

R_γ has to be positive, therefore:

$$t_{\gamma,n} < \frac{R_n}{v_n} \tag{B.3}$$

This inequality can be substituted back into Eq. B.1:

$$
\begin{aligned}
t_{\gamma,n} &< \frac{c^2 t_{\gamma,n} v_n - d v_n^2 \mu \pm \sqrt{v_n^2 \left(c^2(t_{\gamma,n}^2 v_n^2 - 2dv\mu t_{\gamma,n} + d^2) + v^2 d^2(\mu^2 - 1)\right)}}{v_n(c^2 - v_n^2)} \\
c^2 t_{\gamma,n} - t_{\gamma,n} v_n^2 &< c^2 t_{\gamma,n} - d v_n \mu \pm \sqrt{c^2(t_{\gamma,n}^2 v_n^2 - 2dv\mu t_{\gamma,n} + d^2) + v_n^2 d^2(\mu^2 - 1)} \\
d v_n \mu - t_{\gamma,n} v_n^2 &< \pm\sqrt{c^2(t_{\gamma,n}^2 v_n^2 - 2d v_n \mu t_{\gamma,n} + d^2) + v_n^2 d^2(\mu^2 - 1)} \qquad \text{(B.4)}
\end{aligned}
$$

This is a key part in the proof, because at this point one has to decide which sign, positive or negative, to choose for the term on the right-hand-side. The proof is in showing which sign satisfies the inequality. Assuming the sign has to be *negative*, then by definition both sides of Eq. B.4 have to be less than zero. Therefore, if both sides are squared then the inequality sign has to flip:

$$
\begin{aligned}
(d v_n \mu)^2 - 2d v_n^3 \mu t_{\gamma,n} + t_{\gamma,n}^2 v_n^4 &> c^2(t_{\gamma,n}^2 v_n^2 - 2dv\mu t_{\gamma,n} + d^2) + v_n^2 d^2(\mu^2 - 1) \\
v_n^2(t_{\gamma,n}^2 v_n^2 - 2d v_n \mu t + d^2) &> c^2(t_{\gamma,n}^2 v_n^2 - 2d v_n \mu t_{\gamma,n} + d^2)
\end{aligned}
$$

The validity of this expression hinges on whether the term in the parenthesis is positive or negative. It is indeed always positive because

$$
\begin{aligned}
t_{\gamma,n}^2 v_n^2 - 2d v_n \mu t_{\gamma,n} + d^2 \geq &(d - t_{\gamma,n} v_n)^2 > 0 \\
-1 \leq \mu \leq &1.
\end{aligned}
$$

and therefore the *negative* solution is invalid. Assume the positive sign right-hand-side of Eq. B.4, and the left-hand-side has to be positive because that is only valid result from taking a square root:

$$
\begin{aligned}
|d v_n \mu - t_{\gamma,n} v_n^2| &< \sqrt{c^2(t_{\gamma,n}^2 v_n^2 - 2dv\mu t_{\gamma,n} + d^2) + v_n^2 d^2(\mu^2 - 1)} \\
\sqrt{v_n^2(t^2 v_n^2 - 2d v_n \mu t_{\gamma,n} + d^2 \mu^2)} &< \sqrt{c^2(t_{\gamma,n}^2 v_n^2 - 2dv\mu t_{\gamma,n} + d^2) + v_n^2 d^2(\mu^2 - 1)}
\end{aligned}
$$

Since both sides have to be positive, squaring them maintains the inequality. The terms can be re-arranged as before and result in

$$v_n^2(t_{\gamma,n}^2 v_n^2 - 2dv_n\mu t + d^2) < c^2(t_{\gamma,n}^2 v_n^2 - 2dv_n\mu t_{\gamma,n} + d^2)$$

$$v_n < c.$$

which is demonstrably true. Therefore, the solution for the distance from the first neutron scatter and possible source location along the surface of a cone is:

$$\boxed{R_n = \frac{c^2 t_{\gamma,n} v_n - dv_n^2\mu + \sqrt{v_n^2\left(c^2(t_{\gamma,n}^2 v_n^2 - 2dv_n\mu t_{\gamma,n} + d^2) + v_n^2 d^2(\mu^2 - 1)\right)}}{c^2 - v_n^2}} \tag{B.5}$$

BIBLIOGRAPHY

[1] R. Rhodes, *Making of the Atomic Bomb*. New York: Simon and Schuster, 1986.

[2] M. Bunn, Y. Morozov, R. Mowatt-Larssen, S. Saradzhyan, W. Tobey, V. I. Yesin, and P. S. Zolotarev, "The u.s.-russia join threat assessment of nuclear terrorism," 2011.

[3] D. Reilly, N. Ensslin, H. J. Smith, and S. Kreiner, "The origin of neutron radiation," in *Passive nondestructive assay of nuclear materials*, pp. 337–356, Los Aalamos National Laboratory, 1991.

[4] J. M. Verbeke, C. Hagmann, and D. Wright, "Simulation of neutron and gamma ray emission from fission and photofission," Tech. Rep. UCRL-AR-228518, Lawrence Livermore National Laboratory, 2014.

[5] T. E. Valentine, "Evaluation of prompt fission gamma rays for use in simulating nuclear safeguard measuements," Tech. Rep. ORNL/TM-1999/300, Oak Ridge National Laboratory, 1999.

[6] V. V. Verbinski, H. Weber, and R. E. Sund, "Prompt gamma rays from $^{235}\mathrm{U}(n,f)$, $^{239}\mathrm{Pu}(n,f)$, and spontaneous fission of $^{252}\mathrm{Cf}$," *Phys. Rev. C*, vol. 7, pp. 1173–1185, Mar 1973.

[7] X-5 Monte Carlo Team, *MCNP - A General Monte Carlo N-Particle Transport Code, Version 5, Volume I: Overview and Theory*. Los Alamos National Laboratory, April 2003. Appendix H - Fission Spectra Constants and Flux-To-Dose Factors Constant for Fission Spectra.

[8] N. Ensslin, "Principle of neutron coincident counting," in *Passive nondestructive assay of nuclear materials*, pp. 457–492, Los Alamos National Laboratory, 1991.

[9] "Nuclear regulatory legislation," Tech. Rep. NUREG-0980, U. S. Nuclear Regulatory Comission, September 2013.

[10] B. C. Reed, "An examination of potential fission-bomb weaponizability of nuclides other than U-235 and Pu-239," *American Journal of Physics*, vol. 85, pp. 38–44, 2017.

[11] "Iaea safeguards glossary," Tech. Rep. IAEA/NVS/3, International Atomic Energy Agency, Vienna, 2002.

[12] J. J. Duderstadt and L. J. Hamilton, *Nuclear Reactor Analysis*, ch. 1 Introductory Concepts of Nuclear Power Reactor Analysis, p. 84. John Wiley and Sons, 1976.

[13] J. J. Duderstadt and L. J. Hamilton, *Nuclear Reactor Analysis*, ch. 5 The One-Speed Diffusion Theory Model, pp. 150–225. John Wiley and Sons, 1976.

[14] J. D. Lewins, "Neutron lifetime, generation time and reproduction time," *Nucl. Sci. Eng.*, vol. 78, p. 105, 1981.

[15] K. O. Ott and R. J. Neuhold, *Nuclear Reactor Dynamics*, ch. 2 Delayed Neutrons, pp. 5–19. Illinois, USA: American Nuclear Society, 1985.

[16] R. Serber, "The definitions of neutron multiplication," Tech. Rep. LA-335, Los Alamos National Laboratory, 1945.

[17] I. Pazsit and L. Pal, *Neutron Fluctiations*, ch. 11 Theory of Multiplicity in Nuclear Safeguards, pp. 294 – 311. Amsterdam: Elsevier, 2008.

[18] F. de Hoffmann, "Intensity fluctuations of a neutron chain reactor," Tech. Rep. LA-DC-256, Los Alamos National Laboratory, 1944.

[19] M. M. Pickerell, K. Veal, and N. Ensslin, "Fast and epithermal neutron multiplicity counting," in *Passive nondestructive assay of nuclear materials*, no. LA-UR-07-1602, pp. 1–19, Los Alamos National Laboratory, 2007.

[20] D. Chernikova, K. Axell, S. Avdic, I. Pázsit, A. Nordlund, and S. Allard, "The neutron-gamma feynman variance to mean approach: Gamma detection and total neutron-gamma detection (theory and practice)," *Nuclear Instruments and Methods in Physics Research Section A: Accelerators, Spectrometers, Detectors and Associated Equipment*, vol. 782, pp. 47 – 55, 2015.

[21] C. P. Baker, "Time scale measurement by the rossi method," Tech. Rep. LA-617, Los Alamos National Laboratory, 1947.

[22] R. E. Malenfant, "Controlled production of an explosive nuclear chain reaction," Tech. Rep. LA-397, Los Alamos Nationa Laboraory, 1945.

[23] J. D. Orndoff and C. W. Johnstone, "Time scale measurement by the rossi method," Tech. Rep. LA-744, Los Alamos National Laboratory, 1949.

[24] G. E. Mckenzie, "Modern rossi alpha measurements," 2014.

[25] R. Feynman, "Statistical behavior of neutron chains," Tech. Rep. LA-591, Los Alamos National Laboratory, 1946.

[26] J. D. Orndoff, "Prompt neutron periods of metal critical assemblies," *Nuclear Science and Engineering*, vol. 2, pp. 450 – 460, 1957.

[27] F. de Hoffman, "Statistical fluctuations in the water boiler and the dispersion of neutrons exitted per fission," Tech. Rep. LA-101, Los Alamos National Laboratory, 1944.

[28] R. P. Feynman, F. de Hoffmann, and R. Serber, "Dispersion of the neutron emission in u-235 fission," *J. Nuclear Energy*, vol. 3, pp. 64– 69, February 1956.

[29] E. J. Dowdy, G. E. Hansen, A. A. Robba, and J. C. Pratt, "Effects of (α, n) contaminants and sample multiplication on statistical neutron correlation measurements," Tech. Rep. LA-UR-80-743, Los Alamos National Laboratory, 1980.

[30] N. Ensslin, W. H. Geist, M. S. Krick, and M. M. Pickrell, "Active neutron multiplicity counting," in *Passive nondestructive assay of nuclear materials*, no. LA-UR-07-1403, pp. 1–23, Los Alamos National Laboratory, 2007.

[31] G. Birkhoff, L. Bondar, J. Ley, R. Berg, R. Swennen, and G. Busca, "On the determination of pu-240 in solid waster containers by spontaneous fission neutron measurements, application to reprocessing plant waste," Tech. Rep. EUR-5158e, Commission of the European Communities, Joint Research Centre, Ispra, 1974.

[32] K. Böhnel, "Die plutoniumbestimmung in kernbrennstoffen mit der neutronen — koinzidensmethode," Tech. Rep. KFK-2203, Kernforschungszentrum, Karlsruhe, 1975.

[33] N. Envsslin, M. S. Krick, D. G. Langner, M. M. Pickrell, T. D. Reilly, and J. E. Stewart, "Passive neutron multiplicity counting," in *Passive Nondestructive Assay of Nuclear Materials*, pp. 1–32, Los Alamos National Laboratory, 2007.

[34] D. M. Cifarelli and W. Hage, "Models for a three-parameter analysis of neutron signal correlation measurement for fissile material assay," *Nuclear Instruments and Methods in Physics Research Section A*, vol. 251, pp. 550 – 563, 1986.

[35] L. Bondar and B. G. R. Smith, "Interpretation of pu waste measurements by the euroatom time correlation analyser," in *Proc. Int. Symp. Managment α-Contaminated Waste*, (Vienna), June 2-6 1980.

[36] R. Dierckx and W. Hage, "Neutron signal multiplet analysis for the mass determination of spontaneous fission isotopes," *Nuclear Science and Engineering*, vol. 85, no. 4, pp. 325–338, 1983.

[37] W. Hage and D. M. Cifarelli, "On the factorial moments of the neutron multiplicity distribution of fission cascades," *Nuclear Instruments and Methods in Physics Research Section A*, vol. 236, pp. 165 – 177, 1985.

[38] K. Böhnel, "The effect of multiplication on the quantitative determination of spontaneously fissioning isotopes by neutron correlation analysis," *Nuclear Science and Engineering*, vol. 90, pp. 75 – 82, 1985.

[39] W. Hage and D. M. Cifarelli, "Correlation analysis with neutron count distributions in randomly or signal triggered time intervals for assay of special fissile material," *Nuclear Science and Engineering*, vol. 89, pp. 159 – 176, 1985.

[40] S. Croft, A. Favalli, D. Hauck, D. Henzlova, and P. Santi, "Feynman variance-to-mean in the context of passive neutron coincidence counting," *Nuclear Instruments and Methods in Physics Research Section A: Accelerators, Spectrometers, Detectors and Associated Equipment*, vol. 686, pp. 136 – 144, 2012.

[41] E. Miller, S. Clarke, A. Enqvist, S. A. Pozzi, P. Marleau, and J. K. Mattingly, "Characterization of special nuclear material using a time-correlated pulse-height analysis," *Journal of Nuclear Materials Managment*, vol. XLI, no. 1, pp. 32–37, 2012.

[42] E. Miller, J. Dolan, S. Clarke, S. Pozzi, A. Tomanin, P. Peerani, P. Marleau, and J. Mattingly, "Time-correlated pulse-height measurements of low-multiplying nuclear materials," *Nuclear Instruments and Methods in Physics Research Section A: Accelerators, Spectrometers, Detectors and Associated Equipment*, vol. 729, pp. 108 – 116, 2013.

[43] M. G. Paff, M. Monterial, P. Marleau, S. Kiff, A. Nowack, S. D. Clarke, and S. A. Pozzi, "Gamma/neutron time-correlation for special nuclear material detection âĂŞ active stimulation of highly enriched uranium," *Annals of Nuclear Energy*, vol. 72, pp. 358 – 366, 2014.

[44] E. Miller, *Characterization of Fissionable Material using Time-Correlated Pule-Height Technique for Liquid Scintillators*. PhD thesis, University of Michigan, 2012.

[45] P. Marleau, A. Nowack, M. Paff, M. Monterial, S. Clarke, and S. Pozzi, "Gamma/neutron time-correlation for special nuclear material detection âĂŞ active stimulation of highly enriched uranium," Tech. Rep. SAND2013-7442, Sandia National Laboratories, 2013.

[46] M. Monterial, M. Paff, S. Clarke, E. Miller, S. A. Pozzi, P. Marleau, A. N. S. Kiff, and J. K. Mattingly, "Time-correlated-pulse-height technique measurements of fissile samples at the device assembly facility.," in *Proceesdings of the Institute of Nuclear Materials Management 54th Annual Meeting*, (Palm Desert, California), July 17-22 2013.

[47] N. Kornilov, V. Khriatchkov, M. Dunaev, A. Kagalenko, N. Semenova, V. Demenkov, and A. Plompen, "Neutron spectroscopy with fast waveform digitizer," *Nuclear Instruments and Methods in Physics Research Section A*, vol. 497, no. 23, pp. 467 – 478, 2003.

[48] mesytech GmbH, *4 channel particle discriminator module for liquid scintillators*, 2017. "V 2.12_01".

[49] A. Fallu-Labruyere, H. Tan, W. Hennig, and W. Warburton, "Time resolution studies using digital constant fraction discrimination," *Nuclear Instruments and Methods in Physics Research Section A: Accelerators, Spectrometers, Detectors and Associated Equipment*, vol. 579, no. 1, pp. 247 – 251, 2007. Proceedings of the 11th Symposium on Radiation Measurements and Applications.

[50] B. von Krosigk, L. Neumann, R. Nolte, S. Röttger, and K. Zuber, "Measurement of the proton light response of various lab based scintillators and its implication for supernova neutrino detection via neutrino–proton scattering," *The European Physical Journal C*, vol. 73, no. 4, p. 2390, 2013.

[51] H. Schölermann and H. Klein, "Optimizing the energy resolution of scintillation counters at high energies," *Nuclear Instruments and Methods*, vol. 169, no. 1, pp. 25 – 31, 1980.

[52] L. Swiderski, M. Moszyński, W. Czarnacki, J. Iwanowska, A. Syntfeld-Każuch, T. Szczęśniak, G. Pausch, C. Plettner, and K. Roemer, "Measurement of compton edge position in low-z scintillators," *Radiation Measurements*, vol. 45, no. 3, pp. 605 – 607, 2010. Proceedings of the 7th European Conference on Luminescent Detectors and Transformers of Ionizing Radiation (LUMDETR 2009).

[53] G. F. Knoll, *Radiation Detection and Measurement*, ch. 10 Radiation Spectroscopy with Scintillators, p. 229. John Wiley and Sons, fourth ed., 2010.

[54] A. Enqvist, C. C. Lawrence, B. M. Wieger, S. A. Pozzi, and T. N. Massey, "Neutron light output response and resolution functions in EJ-309 liquid scintillation detectors," *Nuclear Instruments and Methods in Physics Research Section A: Accelerators, Spectrometers, Detectors and Associated Equipment*, vol. 715, pp. 79 – 86, 2013.

[55] C. C. Lawrence, M. Febbraro, T. N. Massey, M. Flaska, F. Becchetti, and S. A. Pozzi, "Neutron response characterization for an ej299-33 plastic scintillation detector," *Nuclear Instruments and Methods in Physics Research Section A: Accelerators, Spectrometers, Detectors and Associated Equipment*, vol. 759, no. 0, pp. 16 – 22, 2014.

[56] J. Iwanowska, L. Swiderski, T. Krakowski, M. Moszynski, T. Szczesniak, and G. Pausch, "The time-of-flight method for characterizing the neutron response of liquid organic scintillators," *Nuclear Instruments and Methods in Physics Research Section A: Accelerators, Spectrometers, Detectors and Associated Equipment*, vol. 781, pp. 44 – 49, 2015.

[57] R. Katz, S. Sharma, and M. Homayoonfar, "Detection of energetic heavy ions," *Nuclear Instruments and Methods*, vol. 100, no. 1, pp. 13 – 32, 1972.

[58] L. Stevanato, D. Fabris, X. Hao, M. Lunardon, S. Moretto, G. Nebbia, S. Pesente, L. Sajo-Bohus, and G. Viesti, "Light output of {EJ228} scintillation neutron detectors," *Applied Radiation and Isotopes*, vol. 69, no. 2, pp. 369 – 372, 2011.

[59] H. Wang, D. Carter, T. N. Massey, and A. Enqvist, "Neutron light output function and resolution investigation of the deuterated organic liquid scintillator ej-315," *Radiation Measurements*, vol. 89, pp. 99 – 106, 2016.

[60] J. Birks, *The Theory and Practice of Scintillation Counting*. New York, USA: Perrgamon, 1964.

[61] J. F. Ziegler, "SRIM-2013," 2013.

[62] J. F. Ziegler, J. P. Biersack, and M. D. Ziegler, *SRIM: The Stopping and Range of Ions in Matter*. 15th ed. ed., 2015.

[63] M. A. Norsworthy, A. Poitrasson-Riviére, M. L. Ruch, S. D. Clarke, and S. A. Pozzi, "Evaluation of neutron light output response functions in ej-309 organic scintillators," *Nuclear Instruments and Methods in Physics Research Section A: Accelerators, Spectrometers, Detectors and Associated Equipment*, vol. 842, pp. 20 – 27, 2017.

[64] N. Kornilov, I. Fabry, S. Oberstedt, and F.-J. Hambsch, "Total characterization of neutron detectors with a 252cf source and a new light output determination," *Nuclear Instruments and Methods in Physics Research Section A: Accelerators, Spectrometers, Detectors and Associated Equipment*, vol. 599, no. 2 -3, pp. 226 – 233, 2009.

[65] M. Bourne, S. Clarke, M. Paff, A. DiFulvio, M. Norsworthy, and S. Pozzi, "Digital pile-up rejection for plutonium experiments with solution-grown stilbene," *Nuclear Instruments and Methods in Physics Research Section A: Accelerators, Spectrometers, Detectors and Associated Equipment*, vol. 842, pp. 1 – 6, 2017.

[66] M. Monterial, P. Marleau, S. Clarke, and S. Pozzi, "Application of bayes' theorem for pulse shape discrimination," *Nuclear Instruments and Methods in Physics Research Section A: Accelerators, Spectrometers, Detectors and Associated Equipment*, vol. 795, pp. 318 – 324, 2015.

[67] J. Adams and G. White, "A versatile pulse shape discriminator for charged particle separation and its application to fast neutron time-of-flight spectroscopy," *Nuclear Instruments and Methods*, vol. 156, no. 3, pp. 459 – 476, 1978.

[68] I. A. Pawełczak, S. A. Ouedraogo, A. M. Glenn, R. E. Wurtz, and L. F. Nakae, "Studies of neutronγ pulse shape discrimination in ej-309 liquid scintillator using charge integration method," *Nuclear Instruments and Methods in Physics Research Section A*, vol. 711, pp. 21 – 26, 2013.

[69] C. Liao and H. Yang, "n/γ pulse shape discrimination comparison of ej301 and ej339a liquid scintillation detectors," *Annals of Nuclear Energy*, vol. 69, pp. 57 – 61, 2014.

[70] S. A. Pozzi, M. M. Bourne, and S. D. Clarke, "Pulse shape discrimination in the plastic scintillator ej-299-33," *Nuclear Instruments and Methods in Physics Research Section A*, vol. 723, pp. 19 – 23, 2013.

[71] K. A. A. Gamage, M. J. Joyce, and N. P. Hawkes, "A comparison of four different digital algorithms for pulse-shape discrimination in fast scintillators," *Nuclear Instruments and Methods in Physics Research Section A*, vol. 642, no. 1, pp. 78 – 83, 2011.

[72] Y. Uchida, E. Takada, A. Fujisaki, M. Isobe, K. Ogawa, K. Shinohara, H. Tomita, J. Kawarabayashi, and T. Iguchi, "A study on fast digital discrimination of neutron and gamma-ray for improvement neutron emission profile measurement," *The Review of Scientific Instruments*, vol. 85, no. 11, p. 11E118, 2014.

[73] M. Monterial, P. Marleau, M. Paff, S. Clarke, and S. Pozzi, "Multiplication and presence of shielding material from time-correlated pulse-height measurements of subcritical plutonium assemblies," *Nuclear Instruments and Methods in Physics Research Section A: Accelerators, Spectrometers, Detectors and Associated Equipment*, vol. 851, pp. 50 – 56, 2017.

[74] S. A. Pozzi, E. Padovani, and M. Marseguerra, "MCNP-PoliMi: a Monte-Carlo code for correlation measurements," *Nuclear Instruments and Methods in Physics Research Section A: Accelerators, Spectrometers, Detectors and Associated Equipment*, vol. 513, no. 3, pp. 550 – 558, 2003.

[75] J. A. Nelder and R. Mead, "A simplex method for function minimization," *The Computer Journal*, vol. 7, pp. 308–313, jan 1965.

[76] J. C. Lagarias, J. A. Reeds, M. H. Wright, and P. E. Wright, "Convergence properties of the Nelder-Mead simplex method in low dimensions," *SIAM Journal of Optimization*, vol. 9, pp. 112–147, 1998.

[77] J. Mattingly, "Polyethylene-reflected plutonium metal sphere: Subcritical neutron and gamma measurements," Tech. Rep. SAND2009-5804, Sandia National Laboratories, 2009.

[78] M. Monterial, P. Marleau, and S. A. Pozzi, "Demonstration of time-correlated pulse heigh template-base confirmation measurements," in *Proceesdings of the Institute of Nuclear Materials Management 57th*.

[79] D. W. MacArthur, D. K. Hauck, and M. K. Smith, "Confirmation of nuclear treaty limited items: Pre-dismantlement vs. post-dismantlement," in *Proceedings of the 35th Annual ESARDA Symposium*, (Bruges, Belgium), May 28-30 2013.

[80] A. G. Jie Yan, "Nuclear warhead verification: A review of attribute and template systems," *Science & Global Security*, vol. 23, no. 3, pp. 157–170, 2015.

[81] J. M. Benz. and J. E. Tanner, "Tempting as a chain of custody tool for arms control," in *Proceedings of the 35th Annual ESARDA Symposium*, (Bruges, Belgium), May 28-30 2013.

[82] A. Glaser, B. Barak, and R. Goldston, "A new approach to nuclear warhead verification using a zero-knowledge protocol.," in *Proceesdings of the Institute of Nuclear Materials Management 53rd Annual Meeting*, (Orlando, Florida), July 15-19 2012.

[83] S. Philippe, R. J. Goldston, A. Glaser, and F. d'Errico, "A simplex method for function minimization," *Nature Communications*, vol. 7, Sep 2016.

[84] C. J. MacGahan, M. A. Kupinski, E. M. Brubaker, N. R. Hilton, and P. A. Marleau, "Development of nonsensitive template for arms-control-treaty-verification tasks.," in *IEEE Symposium on Radiation Measurements and Applications*, (Berkeley, California), May 22-26 2016.

[85] C. M. Percher and D. P. Heinrichs, "Criticality safety evaluation for tacs at daf," Tech. Rep. LLNL-TR-489234, Lawrence Livermore National Laboratory, June 21 2011.

[86] C. E. Cohn, "Reflected-reactor kinetics," *Nuclear Science and Engineering*, vol. 13, no. 1, pp. 12 – 17, 1962.

[87] G. D. Spriggs, R. D. Busch, and J. G. Williams, "Two-region kinetic model for reflected reactors," *Annals of Nuclear Energy*, vol. 24, no. 3, pp. 205 – 250, 1997.

[88] J. J. Duderstadt and L. J. Hamilton, *Nuclear Reactor Analysis*, ch. 1 Introductory Concepts of Nuclear Power Reactor Analysis, pp. 62–63. John Wiley and Sons, 1976.

[89] A. Poitrasson-Riviére, M. C. Hamel, J. K. Polack, M. Flaska, S. D. Clarke, and S. A. Pozzi, "Dual-particle imaging system based on simultaneous detection of photon and neutron collision events," *Nuclear Instruments and Methods in Physics Research Section A: Accelerators, Spectrometers, Detectors and Associated Equipment*, vol. 760, pp. 40 – 45, 2014.

[90] J. E. M. Goldsmith, M. D. Gerling, and J. S. Brennan, "MINER - a mobile imager of neutrons for emergency responders," in *Symposium on Radiation Measurements and Applications*, (Ann Arbor, MI), June 9-12 2014.

[91] M. Monterial, P. Marleau, and S. A. Pozzi, "Single-view 3-d reconstruction of correlated gamma-neutron sources," *IEEE Transactions on Nuclear Science*, vol. 64, pp. 1840–1845, July 2017.

[92] T. Gozani, "Fission signatures for nuclear material detection," *IEEE Transactions on Nuclear Science*, vol. 56, pp. 736–741, June 2009.

[93] K. Geiger and L. V. D. Zwan, "Radioactive neutron source spectra from ^{9}Be(α, n) cross section data," *Nuclear Instruments and Methods*, vol. 131, no. 2, pp. 315 – 321, 1975.

[94] M. Wernick and J. Aarsvold, *Emission Tomography: The Fundamentals of PET and SPECT*. Elsevier Science, 2004.

[95] R. W. Todd, J. M. Nightingale, and D. B. Everett, "A proposed [gamma] camera," *Nature*, vol. 251, pp. 132–134, Sep 1974.

[96] V. Schönfelder, "Imaging principles and techniques in space-borne gamma-ray astronomy," *Nuclear Instruments and Methods in Physics Research Section A: Accelerators, Spectrometers, Detectors and Associated Equipment*, vol. 525, no. 1-2, pp. 98 – 106, 2004. Proceedings of the International Conference on Imaging Techniques in Subatomic Physics, Astrophysics, Medicine, Biology and Industry.

[97] D. Herzo, R. Koga, W. Millard, S. Moon, J. Ryan, R. Wilson, A. Zych, and R. White, "A large double scatter telescope for gamma rays and neutrons," *Nuclear Instruments and Methods*, vol. 123, no. 3, pp. 583 – 597, 1975.

[98] G. W. Phillips, "Gamma-ray imaging with compton cameras," *Nuclear Instruments and Methods in Physics Research Section B: Beam Interactions with Materials and Atoms*, vol. 99, no. 1, pp. 674 – 677, 1995.

[99] G. W. Phillips, "Applications of compton imaging in nuclear waste characterization and treaty verification," in *Nuclear Science Symposium, IEEE*, (Albuquerque, NM), Nov 9-15 1997.

[100] H. O. Anger, "Scintillation camera with multichannel collimators," *J Nucl Med.*, vol. 5, pp. 583 – 531, July 1964.

[101] P. Vanier, "Improvements in coded aperture thermal neutron imaging," in *SPIE Conference Proceedings*, vol. 5199, p. 124, 2004.

[102] P. Marleau, J. Brennan, E. Brubaker, and J. Steele, "Results from the coded aperture neutron imaging system," in *IEEE Nuclear Science Symposuim Medical Imaging Conference*, pp. 1640–1646, Oct 2010.

[103] C. G. Wahl, W. R. Kaye, W. Wang, F. Zhang, J. M. Jaworski, A. King, Y. A. Boucher, and Z. He, "The polaris-h imaging spectrometer," *Nuclear Instruments and Methods in Physics Research Section A: Accelerators, Spectrometers, Detectors and Associated Equipment*, vol. 784, pp. 377 – 381, 2015. Symposium on Radiation Measurements and Applications 2014 (SORMA XV).

[104] G. Legge and P. V. der Merwe, "A double scatter neutron spectrometer," *Nuclear Instruments and Methods*, vol. 63, no. 2, pp. 157 – 165, 1968.

[105] R. Barnowski, A. Haefner, L. Mihailescu, and K. Vetter, "Scene data fusion: Real-time standoff volumetric gamma-ray imaging," *Nuclear Instruments and Methods in Physics Research Section A: Accelerators, Spectrometers, Detectors and Associated Equipment*, vol. 800, pp. 65 – 69, 2015.

[106] J. E. McKisson, P. S. Haskins, G. W. Phillips, S. E. King, R. A. August, R. B. Piercey, and R. C. Mania, "Demonstration of three-dimensional imaging with a germanium compton camera," *IEEE Transactions on Nuclear Science*, vol. 41, pp. 1221–1224, Aug 1994.

[107] M. Hamel, J. Polack, A. Poitrasson-Riviére, S. Clarke, and S. Pozzi, "Localization and spectral isolation of special nuclear material using stochastic image reconstruction," *Nuclear Instruments and Methods in Physics Research Section A: Accelerators, Spectrometers, Detectors and Associated Equipment*, vol. 841, pp. 24 – 33, 2017.

[108] M. Hamel, J. Polack, A. Poitrasson-Riviére, M. Flaska, S. Clarke, S. Pozzi, A. Tomanin, and P. Peerani, "Stochastic image reconstruction for a dual-particle imaging system," *Nuclear Instruments and Methods in Physics Research Section A: Accelerators, Spectrometers, Detectors and Associated Equipment*, vol. 810, pp. 120 – 131, 2016.

[109] A. Andreyev, A. Sitek, and A. Celler, "Fast image reconstruction for compton camera using stochastic origin ensemble approach," *Medical Physics*, vol. 38, no. 1, 2011.

[110] F. Pedregosa, G. Varoquaux, A. Gramfort, V. Michel, B. Thirion, O. Grisel, M. Blondel, P. Prettenhofer, R. Weiss, V. Dubourg, J. Vanderplas, A. Passos, D. Cournapeau, M. Brucher, M. Perrot, and E. Duchesnay, "Scikit-learn: Machine learning in Python," *Journal of Machine Learning Research*, vol. 12, pp. 2825–2830, 2011.

[111] P. Cattaneo, M. D. Gerone, F. Gatti, M. Nishimura, W. Ootani, M. Rossella, S. Shirabe, and Y. Uchiyama, "Time resolution of time-of-flight detector based on multiple scintillation counters readout by sipms," *Nuclear Instruments and Methods in Physics Research Section A: Accelerators, Spectrometers, Detectors and Associated Equipment*, vol. 828, pp. 191 – 200, 2016.

[112] S. Pozzi, S. Clarke, W. Walsh, E. Miller, J. Dolan, M. Flaska, B. Wieger, A. Enqvist, E. Padovani, J. Mattingly, D. Chichester, and P. Peerani, "Mcnpx-polimi for nuclear nonproliferation applications," *Nuclear Instruments and Methods in Physics Research Section A: Accelerators, Spectrometers, Detectors and Associated Equipment*, vol. 694, pp. 119 – 125, 2012.

[113] E. O. Lebigot, "Uncertainties: a Python package for calculations with uncertainties." Version 2.4.8.1.

[114] F. Pino, L. Stevanato, D. Cester, G. Nebbia, L. Sajo-Bohus, and G. Viesti, "The light output and the detection efficiency of the liquid scintillator ej-309," *Applied Radiation and Isotopes*, vol. 89, pp. 79 – 84, 2014.